Perforated Panel Absorbers with Viscous Energy Dissipation Enhanced by Orifice Design

Rolf Tore Randeberg

DOCTORAL THESIS

submitted to the Department of Telecommunications,
Norwegian University of Science and Technology,
in partial fulfillment of the requirements for the degree of *doktor ingeniør*

Trondheim, June 2000

Abstract

Currently, there is a great interest in panel absorber design where porous components are excluded due to environmental and cleaning considerations. For such absorbers, the challenge is to increase the natural, viscous losses to attain an acceptable absorption bandwidth. This dissertation presents two new perforated panel absorber concepts, where the viscous energy dissipation has been enhanced by the use of non-traditional design of the perforations.

The first concept is a perforated panel where the perforations has been shaped as small horns. The inner part of the horns have dimensions comparable to microperforated panels. The purpose of the design is to increase the surface area of the opening, increase the flow velocity in the inner part of the horn, and offer a better impedance match to the incoming wave. The concept has been investigated primarily by calculations using the Finite Difference Method. The results indicate that a relatively large absorption bandwidth can be obtained for a horn with wide outer radius and small inner radius.

The second concept is a double perforated panel, consisting of two parallel, perforated plates separated by a small distance, typically $0.1 - 0.3\,\mathrm{mm}$. The main part of the energy dissipation takes place in the small gap between the plates. Both perforated and slitted variants have been investigated by simulations and experiments. For the slitted panel case, absorption bandwidths equivalent to microperforated panels has been observed. The slitted variant can also be designed to be adjustable, allowing the lateral distance between the slits in the two plates to be varied. This offers two special features: The maximum absorption coefficient can be adjusted from unity to almost zero, and the resonance frequency can be shifted. A frequency shift of one octave at normal sound incidence has been obtained.

Preface

This thesis summarizes my work for the degree of *doktor ingeniør* at the Norwegian University of Science and Technology. The work has been conducted at the Acoustics group, Department of Telecommunications, NTNU, and was financed by Hydro Aluminium AS as part of their strategic doctorate program "Aluminium in Buildings" at NTNU. The work described in this thesis was performed in the period February 1997 to June 2000.

Acknowledgements

First, I want to thank my supervisors, Professor Tor Erik Vigran and Professor Ulf Kristiansen, for their excellent support to this thesis. I also want to thank them for their invaluable support and inspiration to my experimental and theoretical work during the project. A special thank goes to Tor Erik Vigran for continuing his support also after his retirement.

I want to thank my colleagues at the Acoustics group for sharing thoughts and common frustrations. In particular I am thankful to Asbjørn Sæbø, with whom I shared office. He has always been helpful when I have had questions about Emacs, Linux, LaTeX, Perl, MATLAB or anything else. I also want to thank the secretary at the Acoustics group, Åse Vikdal, for her helpfulness on all occasions.

Leif O. Malvik and the technicians at the Department workshop deserves a special thank. They have provided extensive help with the design and implementation of equipment and samples used during the experimental work. I special thank also goes to the GNU Project, the Linux Community, Donald E. Knuth, Leslie Lamport, Larry Wall and MathWorks Inc. for providing excellent software for my computational work.

I am very grateful to my wife Lise and my daughters, Ragna Kristine and Inga Amalie, for their endurance during the frustrating periods of my work.

Finally, I want to thank Hydro Aluminium, and vice president Einar Wathne in particular, for giving me the opportunity to take part in this project. Hydro Aluminium has also generously supported guided tours to some of their production sites home and abroad. These tours have given the possibility of sharing technical thoughts, as well as socializing, across the disciplines.

Contents

List of Figures

List of Tables

Nomenclature

Symbols

A	Cross-section area of resonator cavity volume
a	Width of resonator cavity volume
B	Length of resonator cavity volume
b	Center-center distance between resonator openings
C	Acoustic reactance
C_P	Heat capacity of air at constant pressure, $C_\mathrm{P} = 1.01\,\mathrm{J/Kkg}$ * †
c_0	Velocity of sound in air, $c_0 = 340\,\mathrm{m/s}$ ** †
D	Perimeter of resonator opening
d	Thickness of air layer behind panel absorber
d_h, d_v	Thickness of thermal and viscous boundary layers
f, f_0	Frequency, and frequency at resonance
f_1, f_2	Lower and upper half-absorption frequencies, $\alpha = \alpha_0/2$ for $f = f_1, f_2$
g	Gap width between plates of double panel absorber
h	Length of outer part of microhorn
i	An integer denoting plate number
J_m	Bessel's function of first kind and mth order
k	Wave number, $k = 2\pi/\lambda$
k_s	Structure factor of porous material
L	Acoustic inductance
	Number of x- or r-steps in Finite Difference simulations
L_1, L_2	Minimum number of x-steps in narrowest slit, and minimum total steps
l	Length of resonator neck
	Length of inner part of microhorn
	An integer
l_i, l_i'	Length and reduced length of perforations in plate i, $l_i' = l_i - \Delta z S_i$
M	Number of shells in microhorn Integration Method simulation
	Number of z-steps in microhorn Finite Difference simulation
	Number of z-steps in gap in double panel Finite Difference simulation
	Number of discrete angles in approximation of α_st

m	An integer
N	Number of elements facing incoming wave in Finite Element simulation
$\mathbf{n}$	A vector normal to a surface
P, P_0	Pressure, and ambient air pressure
P_h, P_v	Thermal and viscous energy dissipation at a surface
p, Δp	Sound pressure, and sound pressure drop across tube or perforation
p^0	Assumed input sound pressure in Finite Difference models, $p^0 = 1\,\mathrm{Pa}$
$p_{l,m}$	Sound pressure at grid point (l,m)
Q	Q-value of resonance, $Q = f_0/\left(f_2 - f_1\right)$
q	Lateral distance between centers of front and rear slit
R	Acoustic resistance
r, $\bar{r}$	Radius of orifice, and hydraulic radius of orifice, $\bar{r} = 2S/D$
Δr	Radial grid length in Finite Difference simulations
r_0, r_h	Radius of outer and inner parts of microhorn
r_i	Radius of perforations in plate i
r_lin, r_log	Linear and semi-empiric radius function for microhorn, Eqs. (3.26) and (3.25)
r_m	Radius of shell m in microhorn impedance calculation
S	Cross-section area of resonator opening
ΔS	Small area associated with grid point
S_i	Number of z-steps into slit i in Finite Difference simulation
s	Distance between microphones in Kundt's tube
T	Total number of z-steps in Finite Difference simulation, $T = S_1 + M + S_2$
t	Distance between first microphone and sample in Kundt's tube
t_i	Thickness of plate i
U	Volume flow rate
u	Horizontal, lateral or tangential particle velocity
$\mathbf{u}$, $\mathbf{u}_{l,m}$	Particle velocity, $\mathbf{u} = u\hat{\mathbf{x}} + v\hat{\mathbf{z}}$, and particle velocity at grid point (l,m)
V	Volume of resonator cavity
v, $\bar{v}$	Vertical, axial or normal particle velocity, and average axial velocity
W_i	Number of x-steps in slit i in Finite Difference simulation
w, w_i	Width of slits in panel absorber, and width of slits in plate i
X	Position of left edge of rear slit (see Fig. 4.11)
x	Perforate constant (acoustic Reynold's number),[§] $x = r\sqrt{\omega\rho_0/\mu}$
Δx	Horizontal, lateral or tangential grid length in Finite Difference simulations
x_i	Perforate constant of perforations in plate i, with radius $r = r_i$
x_m	Value of x for shell m in microhorn impedance calculation
x_s	Perforate constant for slits, $x = \frac{w}{2}\sqrt{\omega\rho_0/\mu}$
y	Ratio of resonator opening and cavity dimensions
Z	Acoustic impedance, $Z = z/S = p/vS$
z	Specific impedance, $z = p/v$

Δz	Length of shell in microhorn integration model
	Vertical, axial or normal grid length in Finite Difference simulations
z_a	Characteristic impedance of air, $z_a = \rho_0 c_0$

α, α_0	Absorption coefficient, and absorption coefficient at resonance
α_{st}	Absorption coefficient in a diffuse sound field
β, β'	Angles
γ	Ratio of specific heats of air, $\gamma = 1.4$
δ	Mass end correction of resonator neck length, corrected
δ_0, δ_i	Mass end correction of resonator neck length, outer and inner apertures
δ_{tot}	Mass end correction of resonator neck length, both apertures
$\delta_{s,tot}$	Mass end correction of resonator neck length, both apertures (slitted panel)
ε	Argument to Fok's function ψ_{Fok}, $\varepsilon = \sqrt{S/A}$
ζ	Relative, specific impedance, $\zeta = z/\Phi z_a = \theta + j\omega\chi$
η_m	Distance to surface to the right of grid point $(L(m), m)$, in units of Δr
θ	Relative, specific resistance
θ_i, θ_r	Relative, specific system resistance and radiation resistance
κ	Thermal conductivity of air, $\kappa = 23.1\,\mathrm{mW/Km}$ [*] [†]
λ, λ_0	Wavelength, $\lambda = c/f$, and wavelength at resonance
$\lambda_{l,m}$	Distance to surface below Finite Difference grid point (l, m), in units of Δz
μ	Coefficient of viscosity of air, $\mu = 17.9\,\mu\mathrm{Ns/m^2}$ [**] [††]
ρ_0	Density of air, $\rho_0 = 1.23\,\mathrm{kg/m^3}$ [**] [††]
ρ_e	Effective density of air in tube
ρ_{eff}	Effective density of air in cylindrical opening, includes viscous losses
$\rho_{s,eff}$	Effective density of air in slit-shaped opening, includes viscous losses
σ	Flow resistivity of a porous material
σ_e	Effective resistivity of tube
Φ	Perforation of distributed resonator (perforated panel), $\Phi = S/A$
Φ_s	Perforation of distributed resonator (slitted panel), $\Phi_s = w/b$
ϕ	Porosity of a porous material
χ	Relative, specific inductance of perforated panel
ψ_{Fok}	A polynomial function for interaction end corrections, used in Eq. (2.46)
ω, ω_0	Angular frequency, $\omega = 2\pi f$, and angular frequency at resonance

[*] at 0 °C and atmospheric pressure
[**] at 15 °C and atmospheric pressure
[†] *Morse and Ingard* [1968]
[††] *Gerhart et al.* [1993]
[§] *Craggs and Hildebrandt* [1984]; *Maa* [1998]

Abbreviations

FFT	Fast Fourier Transform
FDM	Finite Difference Method
FEM	Finite Element Method
IM	Integration Method
KE	Kinetic energy
MLS	Maximum Length Sequence
MPP	Microperforated panel
PE	Potential energy

Chapter 1

Introduction

The Helmholtz resonator principle is an old and very simple concept. Basically, it consists of an air-filled cavity with a relatively small opening. It has been investigated for over 100 years, most notably by von Helmholtz, Lord Rayleigh and *Ingard* [1953]. Helmholtz resonators are in common use in sound absorbers where absorption at low frequencies is required [See *e. g. Lee and Swenson*, 1992]. The most common implementations are as perforated panel absorbers placed a distance from a back wall, and as silencers in ducts. The required volume of such distributed Helmholtz resonators is significantly smaller than for absorbers of porous materials. Such a construction can have a large sound absorption coefficient at the resonance frequency. However, the absorption bandwidth as usually very limited, due to the small inherent energy dissipation. To compensate for this, the cavity behind the panel has traditionally been partly or completely filled with porous material, or a resistive layer has been put near the resonator openings [*Ingard and Lyon*, 1953; *Ingard*, 1954; *Kristiansen and Vigran*, 1994; *Mechel*, 1994b]. For such configurations, the main functions of the perforated panel are to add a mass reactance to the impedance and to protect the porous material.

Today, there is a trend toward a panel absorber and silencer design where porous materials are excluded. This is primarily due to the environmental disadvantages of porous materials. Porous materials of the fibrous type may release fibers into the air, and are not easily cleaned. Additionally, porous materials may not be robust enough in physically or chemically rough environments [*Ackermann et al.*, 1988]. Consequently, several authors have investigated new panel absorbers concepts. By clever design of the panels, the inherent viscous energy dissipation at the surfaces may be increased compared to the traditional perforated panels.

The simplest of these designs are microperforated panels (MPP), which are perforated panel with sub-millimeter perforations. The small perforations increases the viscous energy dissipation, and hence the absorption bandwidth, significantly compared to traditional perforated panels [*Maa*, 1987, 1998; *Fuchs et al.*, 1999]. The absorption bandwidth may be further extended by combining several MPPs separated by a distance, as described by *Zhang and Gu* [1998]; *Kang et al.* [1998]. The MPP concept is also the basis for commercial products like MICROSORBER®, where the "panels" are thin, perforated foils [*Fuchs et al.*, 1999]. Another panel absorber concept without added porous materials is discussed by *Frommhold et al.* [1994] and by *Mechel* [1994a]. It is a grid of Helmholtz resonators covered by a thin

plate or a foil. The foil is separated from the resonators by a small air gap. The purpose of these kind of absorbers is to increase the number of possible resonances, in addition to the Helmholtz resonance. By optimal design, the flow in the thin gap may cause significant energy dissipation. Mechel has also presented another concept, where the panel is laterally divided in two. The small separation between the two parts introduces additional possible resonances. A foil may also be put between the two parts of the panel to increase the flow in the small gap between the two parts, and hence increase the energy dissipation.

As a continuation of the trend described above, this thesis presents my work on two different perforated panel absorbers where the viscous energy dissipation has been enhanced by the use of non-traditional designs of the panel openings.

Chapter 2 contains an introductory overview of the theory of Helmholtz resonators. This includes theory for the calculation of resonance frequency and energy dissipation of resonators, as well as the impedance of resonator openings. The chapter also includes a short review of relevant prior work on non-fibrous absorbers.

Chapter 3 presents the work with the *microhorn* concept. This is a microperforated panel where the orifices are horn-shaped. The chapter presents three different models. One of these, the Finite Difference Method, has been used to simulate several microhorns geometries where the horn width, length and shape has been varied. The results of these simulations, and one experiment on a microhorn panel sample, are presented.

Chapter 4 presents the work on the double panel concept. The chapter has four sections, corresponding to the four different double panel concepts that has been tested experimentally. Two different models are presented, one for double panels with circular perforations and the other for double panels with slit-shaped openings.

Chapter 2

Helmholtz resonators

The Helmholtz resonator is an ancient and very simple concept. Yet, it has been the subject of investigations for over 100 years, perhaps most notably by von Helmholtz, Lord Rayleigh and *Ingard* [1953]. Those investigators contributed fundamental knowledge about the Helmholtz resonator principle, some of which is recapitulated in what follows.

Helmholtz resonators are in common use in applications such as acoustic elements in rooms and in duct silencers. They can take two principal forms: single resonators or distributed resonators. The perforated panels often used in rooms is an example of distributed Helmholtz resonators. The geometries of Helmholtz resonators are very diverse, but they all have two characteristic features in common: A *cavity* and a relatively small *opening* through which the sound energy enters the cavity. In the case of the distributed Helmholtz resonator, the cavity is shared by the resonator openings. For sufficiently large panels, each opening can be associated with a cavity volume determined by the separation between the perforations. In its various forms, the Helmholtz resonator has both advantages and disadvantages compared to the commonly used porous or fibrous absorbers. By varying the volume of the cavity or the size of the opening, the resonator can be tuned to absorb sound at a given frequency. Thus, absorption in the low frequency range can be achieved without increasing the depth of the absorber construction, as would be required for any porous absorbent. One obvious disadvantage of the Helmholtz resonator, compared to porous absorbers, is that the absorption bandwidth is usually relatively small. This is because the resonator system in itself has low energy dissipation. The low bandwidth has traditionally been compensated for by partly or completely filling the cavity with porous material, or by covering the inner apertures by a thin, resistive layer. The effect of this has been discussed to some extent in the literature [see *e. g. Ingard and Lyon*, 1953; *Ingard*, 1954; *Brouard et al.*, 1993; *Mechel*, 1994b; *Kristiansen and Vigran*, 1994]. This will not be discussed further here.

For a limited frequency range, a Helmholtz resonator is analogous to a simple mechanical damped resonator system. The resilience of the air in the cavity makes it similar to a spring. The mass of the air in and around the orifice is equivalent to a mechanical mass. The value of the "spring constant" and the mass is what mainly determines the resonance frequency, as shown in the next section. The analogous mechanical resistance of the system is mainly determined by viscous energy dissipation at the surfaces of the resonator (see Sec. 2.2).

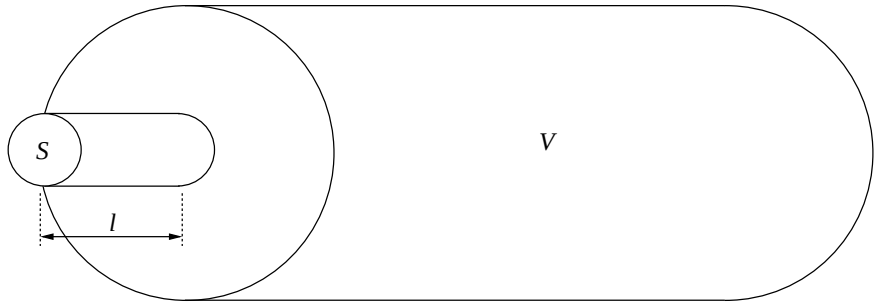

Figure 2.1: *A Helmholtz resonator. The opening of the resonator is often referred to as the* neck. *The cavity volume V, the neck length l and the cross-section area S of the neck determine the resonance frequency of the resonator, by Eq. (2.11).*

2.1 Resonance frequency

Due to the inherent small bandwidth of Helmholtz resonators, a small shift in resonance frequency can result in a significant decrease in absorption coefficient at the target frequency. The calculation of absorption frequency should therefore be as accurate as possible. Several authors have investigated the frequency dependency of the geometry of Helmholtz resonators, and have found that the geometry has a significant influence. For low values of the system resistance, its effect on the resonance frequency can be ignored, as is done below.

2.1.1 Single Helmholtz resonator

The original resonator studied by von Helmholtz was a very simple one; A rigid cavity of volume V, with small dimensions compared to the wavelength of the incident sound. The cavity had a small circular orifice of radius r. When small dimensions are assumed, the complex problem of how waves propagate in the cavity can be ignored. The resonator can then be modeled as a mass-spring-resistance problem as described above. An alternative is to model the resonator by a "lumped-circuit" electrical model, where sound pressure is analogous to voltage and volume flow rate is analogous to current. Either way the resonance frequency of von Helmholtz' resonator is found to be [*Morse and Ingard*, 1968, Eq. 9.1.30]

$$f_0 = \frac{c_0}{2\pi}\sqrt{\frac{2r}{V}} = \frac{c_0}{2\pi}\sqrt{\frac{4S}{VD}}, \tag{2.1}$$

where c_0 is the velocity of sound in air, S is the cross-section area of the orifice and D is the orifice perimeter. This equation can also be used for non-circular orifices of regular shape, *i. e.* not very wide or long.

Equation (2.1) does not contain any reference to the *length* of the cavity opening. The resonance frequency of a cavity with an opening of length l, as shown in Fig. 2.1, can be developed using the mechanical mass-spring analogy mentioned above. The mechanical stiffness of the air in the cavity, k_m, can be derived from the adiabatic, perfect gas equation applied

on a cylindrical volume V, which is compressed an amount $\Delta V = S\Delta x$ by sound pressure ΔP applied to the resonator opening. It is assumed that the cavity walls are rigid.

$$PV^{\gamma} = \text{constant} \tag{2.2}$$

gives, by derivation,

$$\Delta P V^{\gamma} = -\gamma P V^{\gamma-1}\Delta V, \tag{2.3}$$

where $P = P_0$ is the ambient pressure and $\gamma = 1.4$ is the ratio of specific heats of air. Since $\Delta P = \Delta F/S$, we have

$$\frac{\Delta F}{S} = -\gamma P_0 \frac{S\Delta x}{V} \tag{2.4}$$

Therefore,

$$k_{\mathrm{m}} = -\frac{\Delta F}{\Delta x} = \frac{\gamma P_0 S^2}{V} = \frac{\rho_0 c_0^2 S^2}{V}, \tag{2.5}$$

where $\gamma P_0 = \rho_0 c_0^2$, and ρ_0 is the density of air. This derivation assumes sound pressures small compared to the ambient pressure, $\Delta P \ll P_0$, and adiabatic compression of the air [*Morse and Ingard*, 1968, Ch. 6.1]. The mechanical mass of the air in the opening is equivalent to that of a tube of cross-section area S and length l, and is given by

$$m_{\mathrm{m}} = \rho_0 S l \tag{2.6}$$

The mechanical stiffness and mass of the resonator is related to acoustic capacitance and inductance, respectively, by a factor S^2. Thus, the capacitance

$$C = \frac{V}{\rho_0 c_0^2}, \tag{2.7}$$

and the inductance

$$L = \frac{\rho_0 l}{S} \tag{2.8}$$

The resonator system is therefore equivalently described by a mechanical impedance

$$Z_{\mathrm{m}} = \mathrm{j}\omega m_{\mathrm{m}} + \frac{k_{\mathrm{m}}}{\mathrm{j}\omega} + R_{\mathrm{m}}, \tag{2.9}$$

or by an acoustic impedance,

$$Z = \mathrm{j}\omega L + \frac{1}{\mathrm{j}\omega C} + R, \tag{2.10}$$

where $\omega = 2\pi f$. The calculation of the system resistance $R = R_{\mathrm{m}}/S^2$ may involve several energy dissipation mechanisms, and is described further in Sec. 2.2. The resonance frequency of the system is given by

$$f_0 = \frac{\omega_0}{2\pi} = \frac{1}{2\pi}\sqrt{\frac{k_{\mathrm{m}}}{m_{\mathrm{m}}}} = \frac{1}{2\pi}\frac{1}{\sqrt{LC}} = \frac{c_0}{2\pi}\sqrt{\frac{S}{Vl}} \tag{2.11}$$

This equation is a coarse approximation, but can be used with reasonable accuracy on various geometries as long as the dimensions are small compared to the wavelength.

The neck length l in Eq. (2.11) must in most cases be corrected with an added length. This is because the flow of air through the neck affects the air close to the inner and outer apertures. This nearby air will take part in the flow and thus contribute to the total resonator mass. For holes with circular cross-section, Rayleigh proposed an end correction δ_0 that should be added to l in Eq. (2.11) [*Ingard*, 1953; *Chanaud*, 1994]. The proposed end correction,

$$\delta_0 = \frac{8r}{3\pi} = \frac{8}{3\pi}\sqrt{\frac{S}{\pi}}, \tag{2.12}$$

corresponds to the inductive part of the radiation impedance of a circular, plane piston of radius r in an infinite wall. The latter expression for δ_0 can be used as an approximation for other shapes of the resonator opening. Since this end correction corresponds to a single piston flanged in an infinite wall, care must be taken if it is used for the *inner* aperture. For the same reason, Eq. (2.12) may also be invalid for the outer aperture if there are other openings nearby. In lack of a better alternative, Rayleigh used Eq. (2.12) for the inner and outer apertures. The total end correction,

$$\delta_{\text{tot}} = 2\delta_0 = \frac{16r}{3\pi}, \tag{2.13}$$

is then added to l in Eq. (2.11). Thus

$$f_0 = \frac{c_0}{2\pi}\sqrt{\frac{S}{V\left(l+\delta_{\text{tot}}\right)}} = \frac{c_0}{2\pi}\sqrt{\frac{S}{V\left(l+2\delta_0\right)}} \tag{2.14}$$

Ingard [1953] did an extensive survey on the topic of resonators, and presented expressions for the inner end correction for some simple circular and rectangular geometries. Assuming flat velocity profile in the resonator neck, he found expressions for the inner end correction, shown in Fig. 2.2. For openings relative small compared to the resonator cavity cross-section, the inner end correction can be approximated by

$$\delta_{\text{i}} = \delta_0\left(1 - 1.25y\right), \tag{2.15}$$

where y is the ratio of the dimensions of the opening and the cavity, and must be less than 0.4 for the approximation to be valid. According to Ingard, Eq. (2.15) is valid for three different geometries: circular opening/cavity, square opening/cavity, and circular opening/square cavity. *Allard* [1993, Eq. 10.18] gave another approximation for the latter geometry:

$$\delta_{\text{i}} = \delta_0\left(1 - 1.14y\right), \tag{2.16}$$

Note that in his book, Allard gave the correction as function of $\varepsilon = \sqrt{S/A}$, where A is the cavity cross-section area. This is probably an error, neglecting the factor $\sqrt{\pi}/2$ relating ε to y for this geometry. The agreement with curve 2 in Fig. 2.2 is very good for Eq. (2.16) as it is written here. The difference between Eqs. (2.15) and (2.16) is probably negligible in most cases. For small openings, δ_{i} approaches δ_0, and in this case the latter can be used for the inner aperture end correction for all the geometries.

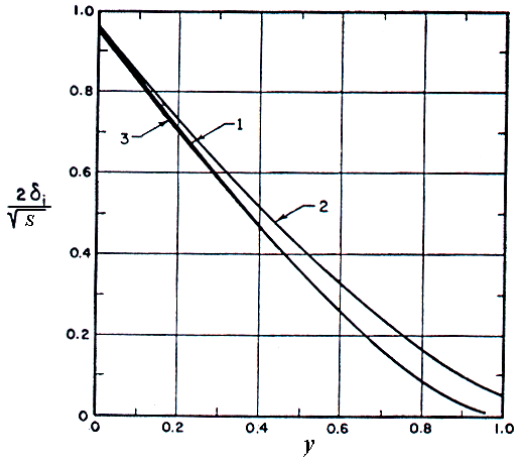

Figure 2.2: *Ingard's calculated inner mass end correction δ_i of various geometries as function of opening to cavity dimension ratio y. 1, Circular opening and cavity; 2, circular opening and square cavity; 3, square opening and cavity. Figure adapted from [*Ingard, *1953, Fig. 3].*

Panton and Miller [1975] showed that when the assumption of long wavelengths compared to the resonator length was dismissed, the resonance frequency for a cylindrical Helmholtz resonator could be found by solving the transcendental equation

$$\frac{lA}{BS}kB = \cot(kB)\,, \tag{2.17}$$

where B is the length of the cavity, and $k = 2\pi/\lambda$ is the wavenumber. A is assumed constant through the cavity length. They showed that by using the two first terms in the series expansion of $\cot(kB)$, the resonance frequency was approximately given by

$$f_0 = \frac{c_0}{2\pi}\sqrt{\frac{S}{V\,(l+\delta_{\text{tot}}) + \frac{B^2 S}{3}}}, \tag{2.18}$$

where $V = AB$, and δ_{tot} has been added to the neck length. The classic expression for the resonance frequency, Eq. (2.14), is similarly found by using only the first term in the series expansion of the cotangent. The classic expression was shown to be accurate only for cavity lengths $B < \pi\lambda/16$. Panton and Miller also noted that Eq. (2.14) conforms *less* with experimental data when Ingard's end correction for the inner aperture is used, *i. e.* $\delta_{\text{tot}} = \delta_0 + \delta_i$, than if the classical end correction is used, $\delta_{\text{tot}} = 2\delta_0$. On the other hand, Ingard's end correction gives the *best* correspondence with measurements when used with Eq. (2.18). They explained this by the fact that the correction terms in Eqs. (2.15) and (2.18) are in opposite directions.

Chanaud [1994, 1997] investigated the effect of extremes in cavity geometry (*deep* or *shallow*), and of the shape, dimension and placement of the opening. A transcendental equation for the resonance frequency, and expressions for the inner end corrections, were also

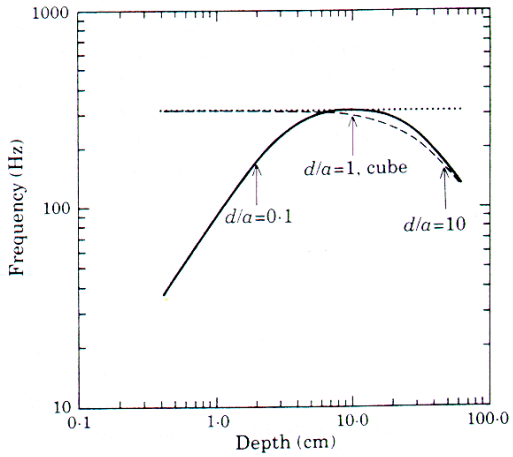

Figure 2.3: *Calculated resonance frequency as a function of cavity depth, for a Helmholtz resonator with a square-faced cavity of constant volume* $1000\,\mathrm{cm}^3$ *and a circular opening of radius* 2 cm *and length* 0.5 cm. $\cdots$*, Rayleigh equation Eq. (2.14);* - - -*, transcendental equation Eq. (2.17) with* $l \to l + 2\delta_0$*; —, Chanaud's analysis. Note that in the figure, d is the cavity length B, and a is the cavity width. Figure from [*Chanaud*, 1994, Fig. 5].*

presented for parallelepipedic and cylindrical cavities. Chanaud assumed no internal resistance in the cavity, a flat velocity profile in the resonator opening, and long wavelengths relative to the dimensions of the *opening*. The main results were:

- The resonance frequency calculated from the Rayleigh equation, Eq. (2.14), deviates significantly from the one predicted by Chanaud except for cubic cavities, as illustrated in Fig. 2.3.
- Panton and Miller's transcendental Eq. (2.17), with l substituted by $l + 2\delta_0$, corresponds with Chanaud's equations for deep cavities, but not for wide cavities. This is also shown in Fig. 2.3.
- Variation in the opening *position* gives the greatest deviation of the Rayleigh equation relative to Chanaud's equations.
- Variation of the opening *shape* gives no significant deviation between the equations.

Chanaud [1997] also noted that Ingard's inner end correction, Eq. (2.15), deviated from the end correction found by Chanaud for y outside the interval $0.22 - 0.52$. It is not stated, but seems clear that *constant* cavity volume has been assumed for this comparison. For wide openings, Ingard let $y = 0.4$ be the upper limit of validity, but indicated no lower limit on y for wide and shallow cavities. Other studies have analytically and numerically confirmed the significance of the shape (*i. e.* length to width ratio) of the resonator volume in determining the resonator frequency [see *e. g. Selamet et al.*, 1995, 1997; *Dickey and Selamet*, 1996].

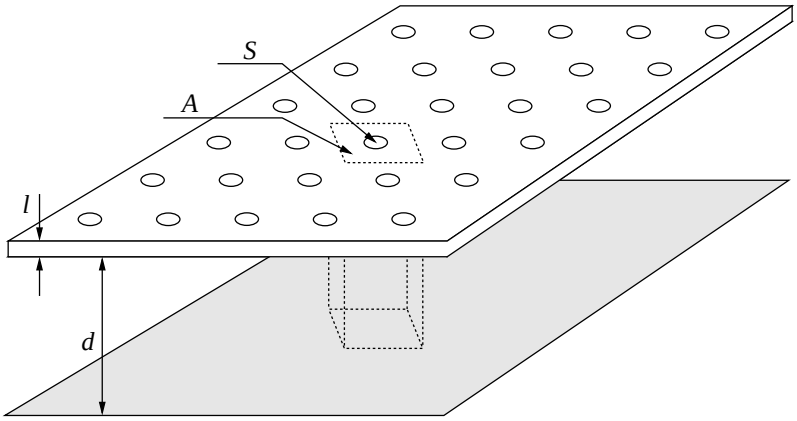

Figure 2.4: *A perforated panel. This is an example of distributed Helmholtz resonators. Each panel opening with cross-section area S has an associated cavity volume Ad. The resonator neck length l equals the thickness of the panel.*

2.1.2 Distributed Helmholtz resonators

The resonance frequency of distributed resonators, as shown in Fig. 2.4, can be calculated by Eq. (2.14) if the panel openings can be considered independent. This is the case when the opening cross-section area S is considerably smaller than the cavity cross-section area A associated with each opening [*Morse and Ingard*, 1968, Ch. 9.1]. When this is the case, Eq. (2.14) can be rewritten as

$$f_0 = \frac{c_0}{2\pi}\sqrt{\frac{\Phi}{d\,(l+\delta_{\text{tot}})}}, \tag{2.19}$$

where $\Phi = S/A$ is the panel perforation. The panel is assumed to be placed a distance d in front of a rigid wall.

Equation (2.19) can also be used for slitted panels. Assuming unit length slits, Eqs. (2.7) and (2.8) are written as

$$C_{\text{s}} = \frac{bd}{\rho_0 c_0^2} \tag{2.20}$$

and

$$L_{\text{s}} = \frac{\rho_0 l}{w}, \tag{2.21}$$

where w is the width of the slits and b is the center-center distance between the slits. The perforation in Eq. (2.19) is then $\Phi_{\text{s}} = w/b$. Of course, the end correction in Eq. (2.13) cannot be used in this case. *Smiths and Kosten* [1951] have studied panel absorbers with infinitely

long slits. Based on two different velocity profiles (*constant velocity* and *constant pressure*) which represents the upper and lower limits on the end correction, they have developed the formula

$$\delta_{\mathrm{s,tot}} = -\frac{2w}{\pi} \ln\left[\sin\left(\frac{\pi w}{2b}\right)\right] \tag{2.22}$$

for the total inductive end correction in the constant pressure case. For small values of b/d, the end correction in the constant velocity case differs insignificantly from the value of $\delta_{\mathrm{s,tot}}$ above. Equation (2.22) was developed assuming $b < \lambda/2$ and $2\pi d/b > 2$. For $f = 500\,\mathrm{Hz}$, these requirements equals $b < 34\,\mathrm{cm}$ and $d > 10\,\mathrm{cm}$, which are usually not hard to satisfy.

2.2 Energy dissipation

The Helmholtz resonator is both an absorber and a scatterer. For distributed Helmholtz resonators, the absorption cross-section at resonance is determined by the ratio of the system resistance θ_{i} to the outer aperture radiation resistance θ_{r}, and is given by [*Ingard*, 1953]

$$\tau = \frac{\lambda_0^2}{2\pi} \frac{4\theta_{\mathrm{i}}/\theta_{\mathrm{r}}}{\left(1+\theta_{\mathrm{i}}/\theta_{\mathrm{r}}\right)^2}, \tag{2.23}$$

where λ_0 is the resonance wavelength. The absorption cross-section has a maximum $\frac{1}{2\pi}\lambda_0^2$ when $\theta_{\mathrm{i}} = \theta_{\mathrm{r}}$. The corresponding absorption bandwidth is usually very small. If θ_{i} is increased by the addition of some porous material or by special design of the opening, then the absorption bandwidth increases at the cost of a decrease in the absorption cross-section area [see *e. g. Cremer and Müller*, 1978a, pp. 195-197]. For most geometries, θ_{r} is usually negligible compared to the θ_{i} [*Ingard and Ising*, 1967; *Melling*, 1973].

Thus, for cases of practical interest, the bandwidth is determined by the system resistance, and it is therefore important to predict this with reasonable accuracy. The system resistance is determined by considering the energy dissipation in the resonator system. The exact mechanisms involved in the energy dissipation in fluids are quite complex [*Morse and Ingard*, 1968, Ch. 6.4], and include:

- Fluid internal energy dissipation by
  - thermal conductivity
  - fluid viscosity
  - molecular energy equipartition
- Surface energy dissipation by
  - thermal conductivity
  - viscosity

For the cases discussed in this work, energy dissipation in relatively small enclosures, the fluid internal energy loss is negligible compared to energy loss at surfaces.

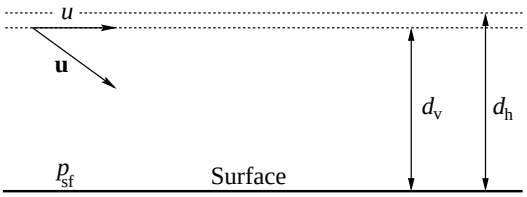

Figure 2.5: *Thermal and viscous boundary layer thicknesses d_h and d_v at a surface. Thermal and viscous energy dissipation at a surface occur mainly inside these layers. The thermal energy loss, Eq. (2.26), depends on the pressure p_{sf} at the surface. The viscous energy loss, Eq. (2.27), is dependent on the tangential particle velocity u at the outside of the viscous boundary layer. The particle velocity* **u** *is zero at the surface.*

2.2.1 Thermal and viscous resistance at a surface

The surface energy dissipations take place in (usually thin) layers close to the surfaces. The widths of these layers, as given by *Morse and Ingard* [1968, Ch. 6.4] are

$$d_h = \sqrt{\frac{2\kappa}{\rho_0 \omega C_P}} \approx \frac{2.4\,\text{mm}}{\sqrt{f\ [\text{Hz}]}}, \tag{2.24}$$

for thermal losses, and

$$d_v = \sqrt{\frac{2\mu}{\rho_0 \omega}} \approx \frac{2.2\,\text{mm}}{\sqrt{f\ [\text{Hz}]}}, \tag{2.25}$$

for viscous losses. Here μ is the coefficient of viscosity of air, κ is the thermal conductivity of air, and C_P is the heat capacity of air at constant pressure. At 100 Hz, d_h and d_v are approximately 0.24 and 0.22 mm, respectively. The values of d_h and d_v represent the minimum distance from a surface where thermal and viscous modes can be considered negligible compared to the propagational mode.

The thermal energy dissipation per unit surface area is proportional to the squared pressure at the surface:

$$P_h \approx \frac{\gamma - 1}{2\rho_0 c_0^2} \omega d_h \left| p_{sf} \right|^2, \tag{2.26}$$

where p_{sf} is the sound pressure at the surface. See Fig. 2.5. The surface is assumed to have high thermal conductivity compared to that of air, so the compressibility is isothermal at the surface. The viscous energy dissipation per unit surface area is proportional to the square of u, the velocity component tangential to the surface *just outside the viscous boundary layer*:

$$P_v \approx \frac{1}{2} \rho_0 \omega d_v \left| u \right|^2 \tag{2.27}$$

It is assumed that the wavelength λ is much greater than d_h and d_v, and that the surface is infinite and plane. The energy loss at a surface can also be expressed as acoustic resistances.

By the electrical analogy, the thermal resistance of a surface ΔS, over which the pressure p is assumed constant, is

$$R_{\mathrm{h}} = \left(\frac{\gamma - 1}{\rho_0 c_0^2} \omega d_{\mathrm{h}} \Delta S \right)^{-1}, \tag{2.28}$$

and the viscous resistance of a surface ΔS is

$$R_{\mathrm{v}} = \frac{1}{U^2} \rho_0 \omega d_{\mathrm{v}} |u|^2 \Delta S = \frac{1}{U^2} \sqrt{2\mu\rho_0\omega}\, |u|^2 \Delta S, \tag{2.29}$$

where U is the volume flow rate by the surface. For most applications, thermal energy loss is negligible compared to viscous loss [*Ingard*, 1953; *Stinson and Shaw*, 1985]. The equivalent electrical circuit has a *large* thermal resistance in parallel with a smaller viscous resistance. The total resistance is mainly determined by the latter.

2.2.2 Viscous resistance in resonator neck

In Helmholtz resonators, the main part of the energy dissipation takes place near and inside the necks, where the velocity is highest. The amount of energy dissipation depends on the velocity profile in and around the resonator neck. Because this velocity profile can be difficult or impossible to calculate analytically even for quite "normal" geometries, the prediction of dissipation is not trivial. Under the assumption of large radius of curvature compared to the viscous boundary layer thickness (*i. e.* no sharp edges) and uniform flow in the neck, *Ingard* [1953] found analytically that the combined acoustic resistance of a circular hole of radius r and the panel surfaces was given by

$$R = \frac{1}{\pi r^2} \sqrt{2\mu\rho_0\omega}\, \frac{1}{r} (l + r) \tag{2.30}$$

The latter r in the parentheses represents the energy dissipation at the panel surfaces, and can be considered to be the total resistive end correction to the neck length l. Ingard's experimental results indicated that the end correction should rather be $2r$ instead of r, thus

$$R = \frac{1}{\pi r^2} \sqrt{2\mu\rho_0\omega}\, \frac{1}{r} (l + 2r) \tag{2.31}$$

This was of course due to the fact that the velocity flow is *not* uniform, and sharp edges exist. Therefore high viscous energy dissipation takes place near the sharp edges. Ingard confirmed the validity of Eq. (2.31) for a number of samples with openings large compared to the boundary layer. From the above equation, the resistive end correction is

$$R_{\mathrm{end}} = \frac{2}{\pi r^2} \sqrt{2\mu\rho_0\omega} = \frac{2}{\pi r^2} \rho_0 \omega d_{\mathrm{v}} \tag{2.32}$$

An expression for the slitted panel case may also be obtained [*Kristiansen and Vigran*, 1994]. Written as acoustic resistance, and assuming unit length slits of width w, it is completely analogous to Eq. (2.31):

$$R_{\mathrm{s}} = \frac{1}{w} \sqrt{2\mu\rho_0\omega}\, \frac{1}{w} (l + 2w) \tag{2.33}$$

2.3 Impedance of cylindrical and slit-shaped openings

2.3.1 Linear domain, independent perforations

Ingard's expressions for R are based on the resistance of flow over an infinite, plane surface, Eq. (2.29). It assumes that the tangential velocity u is calculated from the wave equation, neglecting the effect of viscosity. When the dimension of the opening is comparable to the thickness of the boundary layers, the preceding equations are no longer valid. Viscous (and sometimes thermal) effects must then be incorporated into the equation of motion.

Assuming that the gas is incompressible ($\nabla \cdot \mathbf{u} = 0$), the linearized Navier-Stokes can be written as

$$-\nabla p = \mathrm{j}\omega\rho_0\mathbf{u} - \mu\nabla^2\mathbf{u} \tag{2.34}$$

For simple geometries this equation can be used to find an effective, complex density, ρ_{eff}. The imaginary part of this density is related to the viscous energy loss. A summary of the derivation, for the two geometries circular-cylindrical tube and infinite slit, is presented by *Allard* [1993, Ch. 4]. The procedure is based on original work by Kirchoff and later simplifications by *Zwikker and Kosten* [1949, Ch. 2]. *Stinson* [1991] validated the simplifications for opening radii r in the very wide range $10^{-5}\,\mathrm{m} < r < f^{-3/2}\cdot 10^{4}\,\mathrm{ms}^{-3/2}$. For axial flow in z-direction in a circular, cylindrical tube, Newton's equation can be written as

$$-\frac{\partial p}{\partial z} = \mathrm{j}\omega\rho_{\mathrm{eff}}\bar{v}, \tag{2.35}$$

where $\bar{v}$ is the average velocity over the tube cross-section. Then the specific impedance of a circular tube can be approximated by [see *e. g. Maa*, 1987; *Allard*, 1993]

$$z \approx \frac{\Delta p}{\bar{v}} = \mathrm{j}\omega\rho_{\mathrm{eff}} l = \mathrm{j}\omega\rho_0 l\left[1 - \frac{2}{x\sqrt{-\mathrm{j}}}\frac{J_1\left(x\sqrt{-\mathrm{j}}\right)}{J_0\left(x\sqrt{-\mathrm{j}}\right)}\right]^{-1} \tag{2.36}$$

Here Δp is the pressure drop across the tube of length l, J_i is Bessel's function of first kind and ith order, and

$$x = r\sqrt{\frac{\omega\rho_0}{\mu}} = \sqrt{2}\frac{r}{d_{\mathrm{v}}} \tag{2.37}$$

The parameter x is proportional to the ratio of tube radius and viscous boundary layer thickness. This very important parameter has in the literature been termed *shear wave number*, *acoustic Reynolds' number* and *perforate constant* [*Zwikker and Kosten*, 1949; *Maa*, 1998]. Just like the Reynolds' number, x indicates the importance of inertia forces compared to viscous forces. With the effective density of a slit-shaped opening [*Allard*, 1993, Eq. 4.23], the equivalent of Eq. (2.36) for slits is

$$z_{\mathrm{s}} \approx \mathrm{j}\omega\rho_{\mathrm{s,eff}} l = \mathrm{j}\omega\rho_0 l\left[1 - \frac{\tanh\left(x_{\mathrm{s}}\sqrt{\mathrm{j}}\right)}{x_{\mathrm{s}}\sqrt{\mathrm{j}}}\right]^{-1} \tag{2.38}$$

Here the parameter x_s is given by

$$x_s = \frac{w}{2}\sqrt{\frac{\omega\rho_0}{\mu}} \tag{2.39}$$

It should be noted that Eqs. (2.36) and (2.38) are the impedance of the tube or slit only, and does not include inductive or resistive end corrections.

Craggs and Hildebrandt [1984] used the Finite Element Method (FEM) to solve Navier-Stokes equation, Eq. (2.34) for one-directional sound propagation in tubes of various shapes. In this case only the axial velocity component needs to be considered:

$$-\frac{\partial p}{\partial z} = \mathrm{j}\omega\rho_0 v - \mu\left(\frac{\partial^2 v}{\partial x^2} + \frac{\partial^2 v}{\partial y^2}\right) \tag{2.40}$$

The pressure was assumed to be a function of z only, while the velocity v was assumed to be independent of z. Equation (2.40) was solved for some simple cross-section shapes, *e. g.* slit, rectangle, circle and triangle. The authors stated that the value of the perforation constant x, Eq. (2.37), determine how waves propagate in the tube. For low values of x, *i. e.* $x < 2$, the flow is dominated by viscous effects, this is termed *Poiseuille flow*. For high $x \approx 10$ and above, inertia forces dominate. This is termed *Helmholtz conditions*. The numerical results confirms this separation into different flow regimes. Poiseuille flow has a parabolic velocity profile. For high x, the velocity profile has a low, flat part at the center of the tube, and high peaks near the edge. This applies to circular as well as rectangular and triangular cross-section shapes. With the velocity $\bar{v}$ averaged over the tube cross-section, Craggs and Hildebrandt wrote Newton's equation in the form

$$-\frac{\partial p}{\partial z} = \mathrm{j}\omega\rho_e\bar{v} + \sigma_e\bar{v} \tag{2.41}$$

Note that the effective density ρ_e and the effective flow resistivity σ_e are *real* quantities, as opposed to the complex ρ_{eff} in Eq. (2.35) above. Craggs and Hildebrandt presented calculations of the dimensionless variables ρ_e/ρ_0 and $\sigma_e\bar{r}^2/\mu$ as functions of x. The *hydraulic radius* $\bar{r}$, defined as twice the cross-section area divided by the perimeter, is used in the definition of x. The density ratio was shown to decrease with increasing x, from values 1.2 (slit), 1.33 (circle) and 1.44 (triangle) at $x = 0$, to a *common* value 1.15 for all cross-section shapes when $x > 10$. The resistivity ratio was found to be constant for small x, with extreme values 6.5 (triangle) and 12 (slit). For large x, the resistivity ratio is proportional to x [*Craggs and Hildebrandt*, 1986].

2.3.2 Effect of nonlinearity at high sound pressure levels

The geometries to be presented in Chs. 3 and 4 are relatively complex, and nonlinear effects have not been included in the models described in these chapters. However, it should be noted how nonlinearity affects the impedance of a perforated panel absorber. The nonlinear terms, which have been discarded in the basic equations above, become significant when the driving sound pressure reaches a certain value. The exact value is dependent on the geometry. For a typical microperforated panels, nonlinearity becomes significant for sound pressure levels

above 120 dB, corresponding to a particle velocity 2.5 m/s in the perforations [*Maa*, 1987]. *Ingard* [1953] and *Ingard and Ising* [1967] reported measurements on nonlinear resistance and reactance of circular openings. The results of the latter authors indicate that the nonlinear effects becomes significant for particle velocities around 5 m/s. These, and many other results and theories were reviewed by *Melling* [1973]. Some of the results are presented here.

The most important observation is that, for particle velocity v above some threshold level, the sound pressure in the opening is proportional to the squared velocity, $p \propto \rho_0 v^2$ (Bernoulli's equation). The opening resistance at high sound pressure level is then, according to *Ingard and Ising* [1967],

$$R_{\mathrm{nl}} \approx \rho_0 v, \tag{2.42}$$

and is independent of frequency for frequencies where the absolute value of the reactance is less than R_{nl}. For high sound pressure levels, the nonlinear resistance given above is the dominating part of the system resistance, and the viscous losses in and near the opening can be neglected. The experiments of *Ingard* [1953] indicated a dependency of $v^{1.7}$ instead of v, while *Melling* [1973] from an analytical approach derived the nonlinear resistance

$$R_{\mathrm{nl}} \approx \frac{4\rho_0}{3\pi} v, \tag{2.43}$$

i. e. with a coefficient roughly half of the one used in Eq. (2.42).

The nonlinear reactance of the opening seems to be difficult to determine. It has been found to decrease when the sound pressure level increases. *Ingard* [1953] and *Ingard and Ising* [1967] reported the decrease to be $5/8$ and $1/2$ of the linear value, $\rho_0 \omega (l + \delta_{\mathrm{tot}})$, with δ_{tot} given by Eq. (2.13). The decrease is caused by the formation of turbulence at the "outflow" aperture of the opening. The kinetic energy in the turbulent flow does not contribute to the reactance, and is dissipated. According to *Ingard* [1953], the decrease in reactance is related to the increase in resistance as described above.

2.3.3 Effect of interaction between perforations

The models presented in the preceding sections, with two exceptions (the end corrections in Eq. (2.15) and Eq. (2.22)), assumes that there is only one Helmholtz resonator opening, or, equivalently, that the area S of the openings of a perforated panel is very much larger than cavity cross-section area A associated with each opening. For some geometries, this assumption may not be valid. In these cases, the airflow through the openings are perturbated by the airflow of the neighboring openings. *Melling* [1973] summarized the effects as follows.

The reactive end correction is larger, by a factor of $\sqrt{2}$, for two separate holes than for one hole with area equal to the sum of the two separate holes. The reactive and resistive end corrections decrease when perforations are placed closer to each other. Fig. 2.6 shows a physical picture of the situation. With reference to calculations by V. A. Fok [see *e. g. Rschevkin*, 1963, Ch. VII] for a circular opening in a circular tube, Melling presented a function

$$\psi_{\mathrm{Fok}}(\varepsilon) = \left(1 + a_1 \varepsilon + a_2 \varepsilon^2 + \cdots\right)^{-1} \tag{2.44}$$

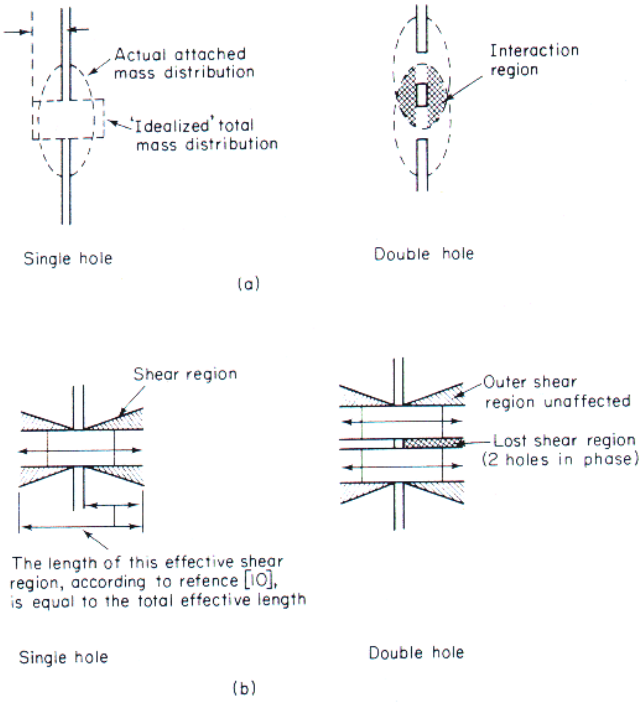

Figure 2.6: *The effect of interaction on the resistive and reactive end corrections. a) Two holes placed close to each other have a common attached mass. The attached mass per hole is less than for a single hole. b) Two holes placed close to each other have airflow in phase. The shear region is reduced or lost. Figure from [*Melling*, 1973, Fig. 5].*

The first polynomial coefficients are:

$$\begin{aligned} a_1 &= -1.4092, & a_2 &= 0, \\ a_3 &= 0.33818, & a_4 &= 0, \\ a_5 &= 0.06793, & a_6 &= -0.02287, \\ a_7 &= 0.03015, & a_8 &= -0.01641 \end{aligned} \tag{2.45}$$

According to Rschevkin, ψ_{Fok} can be used to correct the (reactive) end corrections of an opening in a partition in a tube when the opening area S is not very small compared to the cavity cross-section area A. Fok's function is unity for $\varepsilon = \sqrt{S/A} = 0$, *i. e.* for a small hole or an infinite partition. The function increases sharply when ε increases. The function ψ_{Fok} is used by Melling to correct the total end correction for the case of several interacting holes

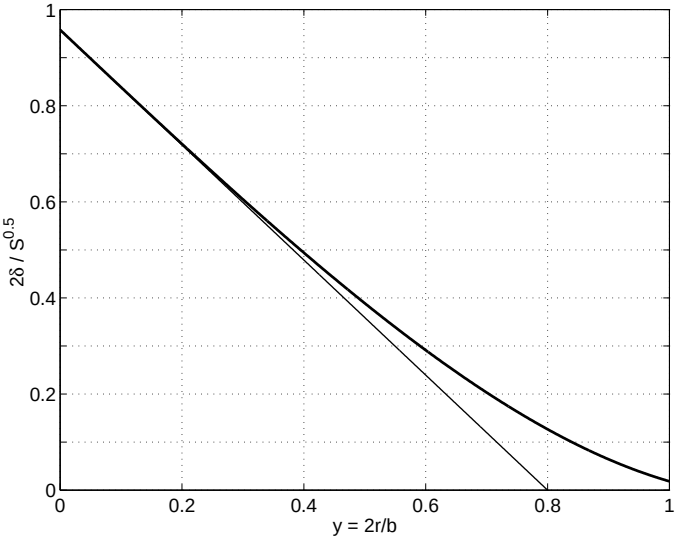

Figure 2.7: *Comparison of two correction factors for the classic end correction δ_0. Total corrected end correction as function of $y = 2r/b$, where r is the perforation radius and b is the distance between perforations.* ——, *Correction by Ingard, $\delta = \delta_0\,(1 - 1.25y)$;* ▬, *Correction by Melling, $\delta = \delta_0/\psi_{\mathrm{Fok}}\left(y\sqrt{\pi}/2\right)$. Compare Melling's curve with Fig. 2.2.*

in a panel with perforation Φ (compare with Eq. (2.36)):

$$Z = \frac{\mathrm{j}\omega\rho_0}{\pi r^2\Phi}\left[l + \frac{2\delta_0}{\psi_{\mathrm{Fok}}\left(\varepsilon\right)}\right]\left[1 - \frac{2}{x\sqrt{-\mathrm{j}}}\frac{J_1\left(x\sqrt{-\mathrm{j}}\right)}{J_0\left(x\sqrt{-\mathrm{j}}\right)}\right]^{-1} \tag{2.46}$$

Note that Melling used two different values for the viscosity; one for air near a thermally conducting surface (used inside the opening), and one for a non-thermally conducting medium (used for the end correction). For simplicity, the latter viscosity is used in Eq. (2.46) for both cases. Also note that the total (reactive) end correction length from Eq. (2.13), $2\delta_0 \approx 1.7r$, is here used as a correction for both the reactive and the resistive part of the impedance. The difference between this and Ingard's value $2r$ in Eq. (2.31) seems to be insignificant.

It is quite interesting to note that, although not stated by Melling, the result of applying $\psi_{\mathrm{Fok}}\left(\varepsilon\right)$ as a correction due to hole interaction, as done above, is practically *equivalent* to using Ingard's inner end correction, Eq. (2.15) for both apertures of the holes in a perforated panel. With ε written as a function of $y = 2r/b$, where b is the perforation distance,

$$\varepsilon = y\frac{\sqrt{\pi}}{2}, \tag{2.47}$$

the two corrections can be compared, as is done is Fig. 2.7. The similarity of Fok's function and Ingard's calculations of δ_{i} is also evident in the book by *Rschevkin* [1963].

The above summary is valid for circular openings. The total reactive end correction for slits, $\delta_{s,tot}$ in Eq. (2.22), explicitly includes the slit distance b, and accounts for the interaction between the slits. As noted by *Smiths and Kosten* [1951]: "...the domain of appreciable kinetic energy is certainly not negligible in comparison with the wavelength". The end correction $\delta_{s,tot}$ decreases when b decreases, as it should according to the discussion above.

2.4 Developments in panel absorber geometries

It was mentioned earlier that porous materials or resistive layers have traditionally been added to Helmholtz resonators to increase the absorption bandwidth. Another approach is to couple more resonators in series, so that the outer neck aperture of the second resonator is in the back wall of the first resonator cavity, and so on. The "cost" of this solution is an increased total depth. In an effort to reduce the volume and the need for extra materials, various alternative geometries have been proposed, all of which try to exploit the inherent viscous losses optimally. Two categories are presented in this section. The first is the use of non-traditional shape and size of the opening and cavity of the resonator. The second is the combination (and interaction) of Helmholtz resonance with the resonances of plates or foils. The first category includes the concepts to be discussed in Chs. 3 and 4.

2.4.1 Non-traditional aperture geometries

Many authors have investigated the effect of alternative shapes and sizes of the resonator neck and cavities. Variations in cavity shape may have significant influence on the resonance frequency, as discussed in Sec. 2.1, but may also give high energy losses in some special cases. An example of the latter is the "prefractal" cavities discussed in an article by *Sapoval et al.* [1997]. On the other hand, variations in neck shape and size may have a significant effect on both resonance frequency and absorption bandwidth.

Helmholtz resonators with slotted neck plates

In light of the work to be presented in Ch. 4, the most interesting non-traditional geometry is the one presented by *Mechel* [1994c]. It is a *laterally* slotted, distributed Helmholtz resonator, which consists of two plates with slit-shaped perforations, placed in front of a hard wall. See Fig. 2.8. The plates are separated by a small distance, a *slot*. In contrast to the concepts discussed in detail in Ch. 4, the perforations in the front plate are placed directly in front of the rear plate perforations. The lateral "side branches" of the neck add an additional impedance to the system. Because the slot is usually thin, the added impedance is mainly capacitive in the frequency range of interest. Mechel observed that this added capacitance shifted the Helmholtz resonance to higher frequency relative to an ordinary Helmholtz resonator without the slot. He also identified two extra resonances, in addition to this shifted Helmholtz resonance, and the $\lambda/4$-resonance of the back cavity:

- The mass-spring-mass resonance of the masses in the necks and the spring of the slot
- The spring-mass-spring resonance of the springs in the slot and back cavity and the mass of the inner neck.

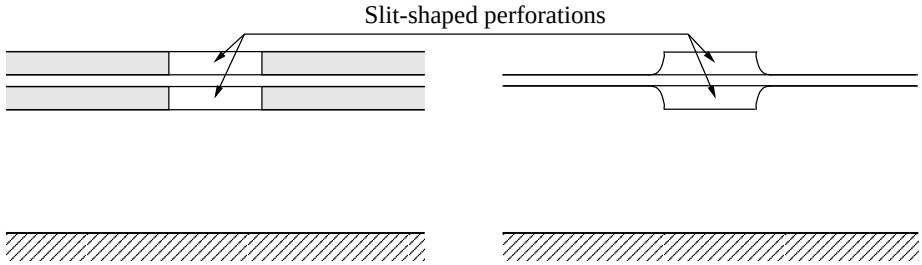

Figure 2.8: *Helmholtz resonators with slotted neck plates. The two variants are approximately equivalent versions. Figure adapted from [*Mechel, *1994c, Fig. 1].*

Because the slot has a high impedance compared to the neck, it is only weakly excited. To increase the driving-field impedance, Mechel suggested that a freely floating, limp, resistive foil could be put into the slot. This will have two effects: *Firstly*, it will increase the overall system resistance. *Secondly*, it will increase the impedance in the neck to a level comparable to the slot impedance, so that the flow in the slot increases. Both effects will increase the energy dissipation, and therefore the absorption bandwidth. The added mass reduces the resonance frequency. Mechel also noted that oblique sound incidence, or an asymmetric partitioning of the slot, result in a splitting of the first of the extra resonances listed above. The split resonances are close to each other, so the effect is a broadening of the resonance.

Microperforated panels

Microperforated panels (MPPs) are increasingly used for reverberation control. It is also the basis for the concept discussed in Ch. 3. As the name implies, MPPs are panels of arbitrary material with perforations of very small dimensions. The perforation diameter is typically less than a millimeter, except for very low frequency absorbers (*Lee and Swenson* [1992] used 20 mm thick panels with perforations of diameter 2 mm for absorption around 50 – 60 Hz). Perforations of small radius, approaching the viscous boundary layer thickness, have velocity profiles quite different from those of "normal" perforations, as described by *Craggs and Hildebrandt* [1984] (see page 14). This reduced radius significantly increases the viscous energy losses in the perforations [*Morse and Ingard*, 1968, Ch. 6.4].

Based on Crandall's simplifications of Eq. (2.36) for high and low values of x,

$$z = \begin{cases} \frac{8\mu l}{r^2} + \mathrm{j}\frac{4}{3}\omega\rho_0 l & \text{if} \quad x < 1 \\ \sqrt{2\rho_0\mu\omega}\,\frac{l}{r} + \mathrm{j}\omega\rho_0 l\left(1 + \frac{1}{r}\sqrt{\frac{2\mu}{\rho_0\omega}}\right) & \text{if} \quad x > 10, \end{cases} \tag{2.48}$$

Maa [1987] has developed an expression for the impedance of the openings for intermediate values of x (The value of x is 2.3 for $f = 200$ Hz and perforation diameter $2r = 0.5$ mm). By adding the classic inductive end correction, Eq. (2.13) and Ingard's resistive end correction, Eq. (2.32), Maa obtained an expression for the specific, relative resistance and inductance of

the panel:

$$\zeta = \frac{z}{z_a \Phi} = \theta + j\omega\chi, \tag{2.49}$$

where $z_a = \rho_0 c_0$ is the characteristic impedance of air, Φ is the panel perforation percentage, and the relative resistance θ and inductance χ is given by

$$\theta = \left(\frac{8\mu l}{\Phi \rho_0 c_0 r^2}\right)\left(\sqrt{1+\frac{x^2}{32}} + \sqrt{2}\frac{xr}{4l}\right) \tag{2.50}$$

and

$$\omega\chi = \left(\frac{\omega l}{\Phi c}\right)\left(1 + \frac{1}{\sqrt{9+\frac{1}{2}x^2}} + \frac{16r}{3\pi}\right) \tag{2.51}$$

Note that Maa's equation for θ had an error. Equation (2.50) is equivalent to an expression given in a later paper by *Fuchs and Zha* [1995]. Also note that Ingard's resistive end correction is used in Eq. (2.50), despite the fact that it was only experimentally validated for relatively large openings [*Ingard*, 1953], *i. e.* for *Helmholtz conditions*, $x > 10$. *Melling* [1973] argued that Ingard's end correction should generally be valid, also for $x < 1$. This is because the opening length l is an independent variable both in the general expression for the impedance, Eq. (2.36), and in the Crandall's approximate expressions, Eq. (2.48). Maa did not include any correction of the end corrections due to hole interaction. For typical dimensions of MPPs, *e. g.* $2r = 0.5\,\text{mm}$ and $b = 5\,\text{mm}$, the value of ψ_{Fok} is 1.14, thus the effect of hole interaction need not be included.

The ideal absorber has $\theta = 1$ (specific resistance of opening equals characteristic resistance of air) and $\theta/\omega\chi \gg 1$ (small inductance of opening) [*Maa*, 1987]. The resistance to reactance ratio increases for smaller r and f. Although there is a lower practical limit on r, restricting the size of this ratio, microperforated panels can achieve a relatively high absorption bandwidth, typically two octaves. In a later paper, *Maa* [1998] showed that for x less than about 1, the bandwidth is mainly determined by θ, and is practically independent of x. See Fig. 2.9. Larger values of θ gives high bandwidth. For large x, the opposite is true; the bandwidth *decreases* when θ increases. The maximum absorption coefficient, α_0, is given by the relative resistance as

$$\alpha_0 = \frac{4\theta}{(1+\theta)^2} \tag{2.52}$$

The MPPs have also been combined in multiple layer configurations. Each segment, consisting of one MPP and an air layer, is equivalent to an electrical circuit segment consisting of a resistance, an inductance, and a parallel capacitance [*Kang et al.*, 1998]. Although an increase in the total depth of the panel absorber is inevitable, optimal configurations will broaden the absorption bandwidth significantly compared to a single layer. *Zhang and Gu* [1998] showed that the resonance and anti-resonance frequencies of a two-layer MPP did

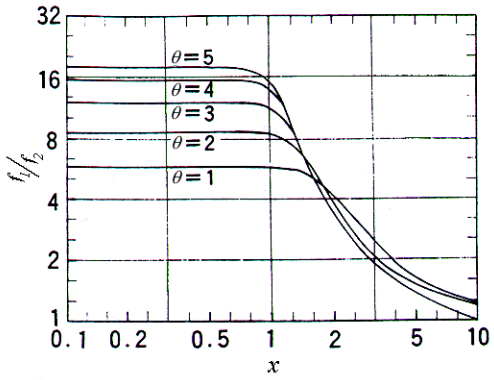

Figure 2.9: *Half-absorption bandwidth of MPP as a function of perforate constant x for several values of the relative, specific resistance θ, as calculated by Maa. Figure adapted from [*Maa*, 1998, Fig. 4].*

not change significantly when the resistance of rear layer was assumed zero. Based on this assumption, an analytical expression for the resonance frequencies was developed, and was shown to agree with experimental results.

If the MPPs are thin, plate vibration may influence the absorption characteristics [see *e. g. Ke et al.*, 1998; *Zhou et al.*, 1998]. The effect of the plate vibration is equivalent to adding an impedance in parallel to the resistance and inductance of the perforation [*Kang et al.*, 1998]. This impedance consists of an inductance, given by the surface density of the plate, and a resistance, given by the energy losses caused by the vibration. The vibration of MPPs is driven by the pressure difference over the plate. *Tanaka and Takahashi* [1999] showed that for large perforations, the vibrations have little influence. On the other hand, small perforations gives high flow resistivity in the holes and large pressure difference across the plate. This significantly influences the MPP absorption. The absorption peak is shifted to lower frequency for increased mass density of the plate. *Zhou et al.* [1998] noted that vibration modes with frequencies below the Helmholtz resonance of the absorber have little influence on the absorption characteristics. On the other hand, higher vibration modes may or may not have their frequencies shifted to higher frequencies, depending on whether the impedance of the plate is comparable to the impedance of the perforations or if it is much smaller than the perforation impedance.

In addition to metal, the microperforated panels may also be made of other materials. A recent development is the MICROSORBER® concept, which is a transparent, thin (approx. 0.1 mm), microperforated foil made of plastics like polyethylene or polyester. The perforation radii can be as small as 0.2 mm. Multiple foils can be combined to increase the absorption bandwidth. Figures 2.10 and 2.11 shows measurement and simulations of absorber consisting of one and two layers of such thin foils, respectively.

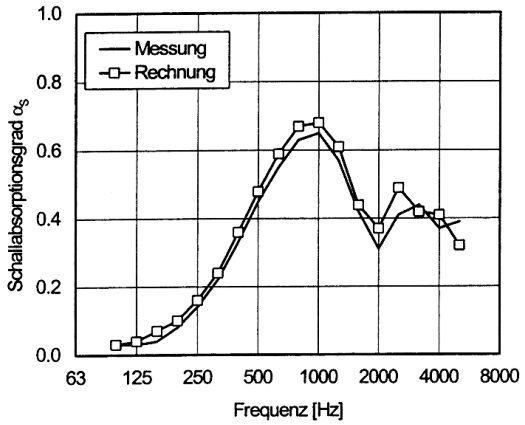

Figure 2.10: *Calculated and measured (in reverberation chamber) absorption coefficient of microperforated foil,* 0.1 mm *thick, and with perforations of diameter* 0.2 mm *and with* 2 mm *separation. The distance to the back wall is* 100 mm*. Figure from [*Fuchs et al.*, 1999, Bild 4]*.

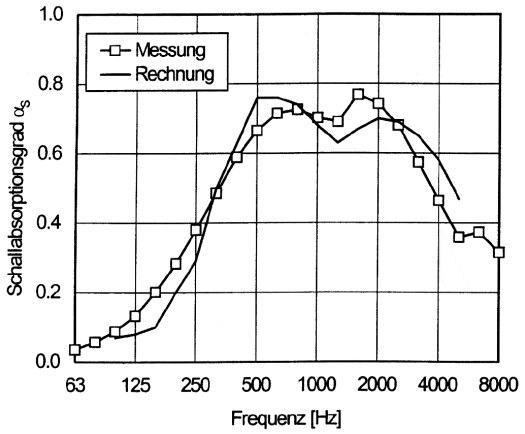

Figure 2.11: *Calculated and measured (in reverberation chamber) absorption coefficient of a two-layer microperforated foil. All foil parameters are as in Fig. 2.10. Front foil placed* 30 mm *in front of rear foil. Figure adapted from [*Fuchs et al.*, 1999, Bild 5]*.

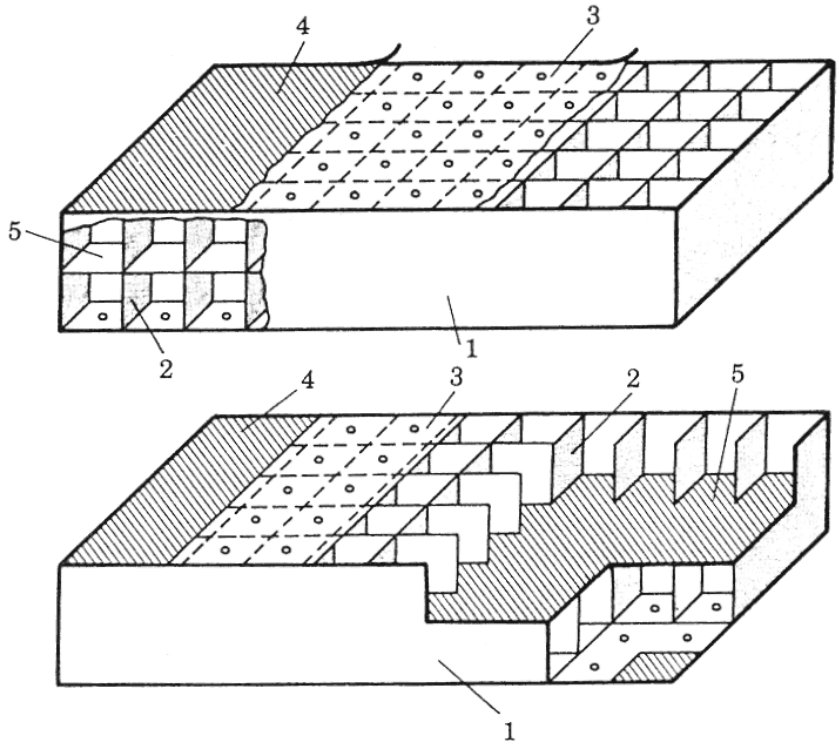

Figure 2.12: *Geometry of absorber concept described by* Frommhold et al. *[1994] and* Ackermann et al. *[1988]. Helmholtz resonators covered by protecting plate. 1, Frame; 2, cavity walls; 3, flexible, perforated plate; 4, cover plate; 5, support plate. Figure from [*Frommhold et al.*, 1994, Fig. 1].*

2.4.2 Helmholtz resonators covered by plates or foils

Several authors have investigated the characteristics of traditional Helmholtz resonators covered by foils or plates. This has two implications: *Firstly*, additional resonances are added to the system, and may interact with the Helmholtz resonance. *Secondly*, the smooth front surface may function as a protection in harsh environments, which is often desirable.

Ackermann et al. [1988] presented an absorber suited for rough environments, *e. g.* as a silencer. The absorber consists of several Helmholtz resonators with a flexible, perforated plate as top cover, which in turn is covered and sealed by a smooth, protecting “membrane”. Mechel pointed out later that the correct term should be *foil*, because there is no tensile stresses involved [*Mechel*, 1994a]. The cover plates are also so thin that bending stiffness can be included in an effective mass density of a limp foil, for frequencies below the critical frequency of the plates. Figure 2.12 shows the absorber concept. The outer cover plate may be separated from the perforated plate with a thin foam ring. The inner and outer cover plates

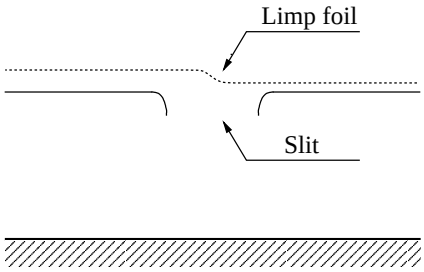

Figure 2.13: *Helmholtz resonator covered by a limp foil (the foil is shown dotted). Mechel's article discusses asymmetrical air gaps between the foil and the slitted resonator neck plate, therefore the widths of the gaps need not be equal. Figure adapted from [*Mechel*, 1994a, Fig. 1].*

are typically a few tenths of a millimeter thick, while the openings of the Helmholtz resonator are in the order of one or two centimeters. The number of different dimensions and material parameters, results in a relatively complicated absorber.

A detailed examination of the absorber was presented later by *Frommhold et al.* [1994]. The absorber concept cannot be described by simple lumped elements because of the interaction between the involved mechanisms. Frommhold *et al.* identified two main absorption peaks. The first is due to the ordinary Helmholtz resonance of the cavities covered with the perforated plate. This resonance frequency is shifted to lower frequencies when the mass of the outer cover plate is added. The second peak is related to the main resonance of the perforated plate. The cover plate is shown to be essential for the quality of the absorber. The cover rises the maximum absorption of the plate resonance from 0.5 to about 0.8. Frommhold *et al.* proposed several explanations for the effect of the cover plate: *Firstly*, viscous losses in the thin air layer between the cover plate and the perforated plate are introduced. *Secondly*, energy may dissipate in the foam support. *Thirdly*, viscous losses at the edge of the perforations increase because the perforations cannot radiate into open half-space; the vibrating air has to enter the small gap between the plates. The latter effect is frequency dependent, because the relative velocity of the air and the plate has a maximum at resonance frequencies.

Mechel [1994a] investigated a comparable concept by a thorough analysis; a slitted panel absorber covered by a limp foil, as shown in Fig. 2.13. His conclusion is that the foil covered resonators are inferior to the slotted neck plates discussed in Sec. 2.4.1, despite the advantage of a smooth outer surface. Among the disadvantages listed are:

- Fewer excitable resonances
- Outer cover vulnerable to mechanical attacks
- Gap width difficult to control

Chapter 3

Microperforated panels with horn-shaped orifices

This chapter describes the investigation of a special concept for panel absorbers; Panels with horn-shaped openings, as shown in Fig. 3.1. The inner part of each horn has dimensions approximately equivalent to traditional microperforated panels (MPPs), as described in Sec. 2.4.1. The concept, called *microhorn*, was thought to have the following virtues:

- The incoming wave is offered a better impedance match than with normal MPPs
- The larger surface area of the opening increases the system resistance
- The increased particle velocity in the inner part of the horn also increases the resistance

The microhorn concept has been modelled by three different methods, none of which were completely satisfactory. Because of this, no reliable estimate of an optimal geometry could be made. Only one geometry was experimentally tested.

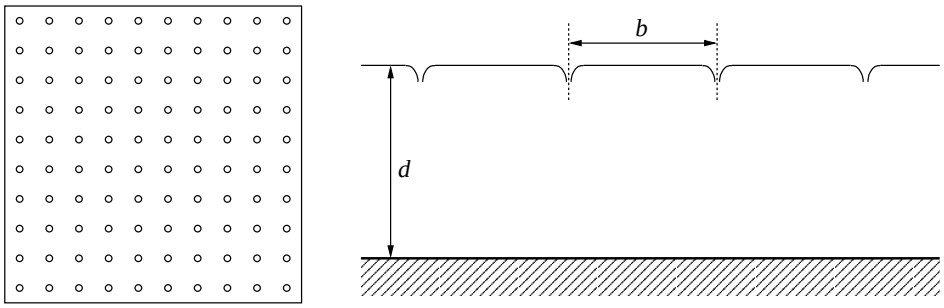

Figure 3.1: *Front view and cross-section of microhorn panel absorber.*

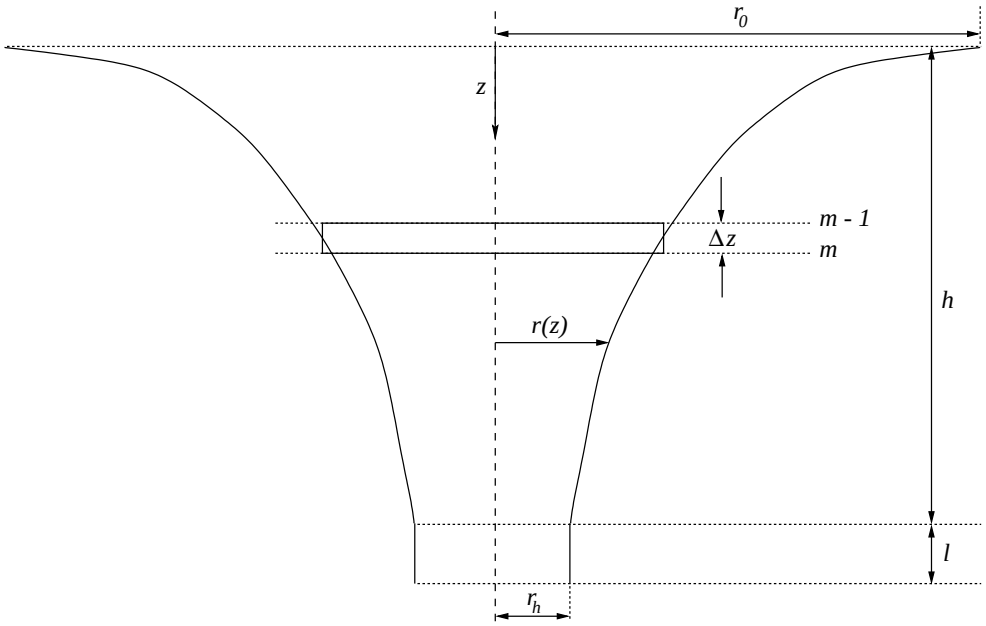

Figure 3.2: *The geometry of a typical microhorn. For the outer part of the horn,* i. e. *z in the range* $0-h$*, the shape is given by the function* $r(z)$*. The inner part of the horn is an ordinary cylindrical tube of length* l*. For the Integration Method, Sec. 3.1.1, the outer part is divided into cylindrical shells of length* Δz*. The shells are very short tubes, and the impedance of each tube is calculated by Eq. (2.36). The impedances of the tubes are added to give the total impedance of the outer part of the horn.*

3.1 Models

The impedance of a cylindrical, circular opening or tube may be calculated by the theory presented in Sec. 2.3. However, the addition of the horn complicates the calculation. The following sections present three different approaches to the calculation of the impedance of the horn-shaped panel openings. The first method is a semi-analytic model, called the Integration Method (IM), whereas the other two are the numeric Finite Element Method (FEM) and Finite Difference Method (FDM), respectively.

Figure 3.2 shows the cross-section of a single microhorn. To make the modelling flexible with regard to variations in dimensions, the horn is divided into two parts. The inner (rear) part is an ordinary, cylindrical tube of length l and radius r_h. The outer (front) part has a shape described by the function $r(z)$, where z is the distance from the front opening. The front opening has radius r_0. The length of the outer part is h. The arbitrary function $r(z)$ is only subject to the constraints $r(0) = r_0$ and $r(h) = r_h$. The microhorn panel absorber consists of a rectangular grid of microhorns, where the center to center distance between the horns is b, as illustrated in Fig. 3.1. The panel is placed a distance d in front of a hard wall.

3.1.1 Integration Method

A simple model of the microhorn absorber uses the simplified Kirchoff model for cylindrical perforations, Eq. (2.36). For the calculation of the acoustic impedance of the outer part of the horn ($z < h$ in Fig. 3.2), this part of the horn is divided into M short cylindrical shells, analogous to a method used by *Pfretzschner et al.* [1999]. Thus, each shell is a circular cylindrical tube of length $\Delta z = h/M$. The acoustic impedance of each of these short tubes is then added, and the result is the total acoustic impedance of the outer horn:

$$Z_{\text{outer}} = \sum_{m=1}^{M} \frac{\mathrm{j}\omega\rho_0 \Delta z}{\pi \bar{r}_m^2} \left[1 - \frac{2}{x_m\sqrt{-\mathrm{j}}} \frac{J_1\left(x_m\sqrt{-\mathrm{j}}\right)}{J_0\left(x_m\sqrt{-\mathrm{j}}\right)} \right]^{-1} \tag{3.1}$$

Here the radius of shell m is $\bar{r}_m = \frac{1}{2}\left(r_{m-1} + r_m\right)$, where $r_m = r\left(m\Delta z\right)$. The perforate constant x_m is given by Eq. (2.37) with $r = \bar{r}_m$. The acoustic impedance of the inner part of the horn is

$$Z_{\text{inner}} = \frac{\mathrm{j}\omega\rho_0 l}{\pi r_h^2} \left[1 - \frac{2}{x\sqrt{-\mathrm{j}}} \frac{J_1\left(x\sqrt{-\mathrm{j}}\right)}{J_0\left(x\sqrt{-\mathrm{j}}\right)} \right]^{-1} \tag{3.2}$$

Here $r = r_h$ is used in the expression for x. At both ends of the microhorn, inductive and resistive end corrections are included. Equations (2.12) and (2.32) give

$$Z_{\text{end,outer}} = \frac{1}{\pi r_0^2} \left(\mathrm{j}\omega\rho_0 \frac{8r_0}{3\pi} + \sqrt{2\mu\rho_0\omega} \right) \tag{3.3}$$

and

$$Z_{\text{end,inner}} = \frac{1}{\pi r_h^2} \left(\mathrm{j}\omega\rho_0 \frac{8r_h}{3\pi} + \sqrt{2\mu\rho_0\omega} \right) \tag{3.4}$$

Note that the end correction of Eq. (2.32) is the *total* resistive end correction (both apertures). This has been split in two parts here. The acoustic impedance of the air layer between the panel and the wall is [*Allard*, 1993, Eq. 2.21]

$$Z_{\text{air}} = -\mathrm{j}\frac{z_{\text{a}}}{b^2}\cot kd, \tag{3.5}$$

where $z_{\text{a}} = \rho_0 c_0$ is the characteristic impedance of air. For small cavity depths, $kd \ll 1$, the impedance Z_{air} equals the capacitive part of Eq. (2.10), and is inversely proportional to the cavity volume $V = b^2 d$. This is the reason that d in Fig. 3.1 is measured from the back of the plate, and not from the rear aperture of the microhorns. The total acoustic impedance of the microhorn absorber is the sum of the above impedances,

$$Z_{\text{mh}} = Z_{\text{air}} + Z_{\text{end,inner}} + Z_{\text{inner}} + Z_{\text{outer}} + Z_{\text{end,outer}}, \tag{3.6}$$

and the absorption coefficient of the panel is [*Morse and Ingard*, 1968, Ch. 6.3]

$$\alpha = 1 - \left| \frac{Z_{\text{mh}} b^2 - z_{\text{a}}}{Z_{\text{mh}} b^2 + z_{\text{a}}} \right|^2 \tag{3.7}$$

The model described above introduces two sources of error. *Firstly*, the discretization of the curved surface into a series of short, cylindrical tubes introduces an error. This error can be reduced by increasing M. The model requires little computing power compared to a numerical method (*e. g.* FDM), thus M can be made very large. The *second* error is related to the velocity field in the microhorn. For large M, the velocity field in each short tube m in the range $2 \ldots M-1$ is approximately equivalent to the velocity field in the neighboring tubes, so there is no significant error caused by the discontinuities of the horn cross-section. Also, Eq. (2.36) seems valid for infinitesimal short tubes. However, the velocity field in the horn is not axial, as assumed in the development of Eq. (2.36), but has a significant radial component. The error caused by this cannot be eliminated by increasing M, and can only be ignored for long, narrow horns. Consequently, the Integration Method can only be considered as a first approximation.

3.1.2 Finite Element Method

The Finite Element Method is here applied to the entire length of the microhorn. The computer program that is used, *FEMAK*, does not have a special element type for viscous sound propagation in air [*Johansen et al.*, 1996]. Instead, an equivalent fluid type element, designed for sound propagation in porous materials with rigid frame, is used. Two versions of this element exist; one which uses a slightly corrected version of a model by *Craggs* [1978, 1986], and another which uses the Johnson-Allard model [*Allard*, 1993, Ch. 5]. The former, simpler version, which is used here, is based on theory by *Zwikker and Kosten* [1949]. Adiabatic compression is assumed, so thermal losses are excluded. The corrections to Craggs' model concern the effective density and the continuity of the volume velocity. The viscous losses in the porous material are included in the complex density of the equivalent fluid.

Using the equivalent fluid model to describe flow through a porous material, Newton's equation and the mass conservation equation can be written [*Johansen et al.*, 1996]

$$-\nabla p = \left(\frac{\mathrm{j}\omega\rho_0 k_\mathrm{s}}{\phi} + \sigma \right) \mathbf{u} \tag{3.8}$$

$$\nabla \cdot \mathbf{u} = -\frac{\mathrm{j}\omega\phi}{\rho_0 c_0^2} p, \tag{3.9}$$

where ϕ is porosity, σ is flow resistivity, and k_s is the structure factor. These are characteristic parameters of the porous material. The velocity $\mathbf{u}$ can be eliminated by the combination of the equations. With the obvious assumption of $\phi = 1$ and $k_\mathrm{s} = 1$ for the air in the microhorn, the result is the Helmholtz equation,

$$\nabla^2 p + k_1^2 p = 0, \tag{3.10}$$

where the complex, squared wave number is

$$k_1^2 = \frac{\omega^2}{c_0^2} - \frac{\mathrm{j}\omega\sigma}{\rho_0 c_0^2} = \frac{\omega^2}{c_0^2} \left(1 - \frac{\mathrm{j}\sigma}{\rho_0 \omega} \right) \tag{3.11}$$

Eliminating velocity from the linearized Navier-Stokes equation (Eq. (2.34)) and the mass conservation equation (Eq. (3.9) with $\phi = 1$) also results in the Helmholtz equation. The

squared wave number for sound propagation in viscous fluid is then written as

$$k_2^2 = \frac{\omega^2}{c_0^2}\left(1 + \frac{\mathrm{j}\omega\mu}{\rho_0 c_0^2}\right)^{-1} \tag{3.12}$$

Because k_1 and k_2 are characteristic parameters for the same viscous flow, described by the Helmholtz equation, they can be equated. Thus, the flow resistivity can be related to the viscosity by

$$\sigma = \mu\frac{\omega^2}{c_0^2}\cdot\frac{1}{1+\frac{\mathrm{j}\omega\mu}{\rho_0 c_0^2}} \approx \mu\frac{\omega^2}{c_0^2} \tag{3.13}$$

For audible frequencies, the absolute value of the ratio in the denominator is equal to or less than $1.5\cdot10^{-5}$. Hence the approximation introduces no significant errors. For $f = 200\,\mathrm{Hz}$, the equivalent flow resistivity $\sigma \approx 2.44\cdot10^{-4}\,\mathrm{Pas/m^2}$. Compared with the flow resistivity of typical porous materials like rock wool, which is in the order of $10\,\mathrm{kPas/m^2}$, the flow resistivity by Eq. (3.13) is very small.

The implementation of the equivalent fluid element in *FEMAK* does not handle impedances or sources at the edge of the element. Therefore, it is required to add a layer of ordinary fluid elements at the inner and outer end of the microhorn. The elements at the outer opening are defined to see an incoming plane wave with amplitude 1 Pa parallel to the horn axis. These elements also face a specific impedance equal to z_a. The elements at the inner opening face the specific impedance of the air layer between the panel and the wall, with the addition of the inner end correction $\pi r_h^2 \cdot Z_{\mathrm{end,inner}}$. The thickness of the air layer is adjusted to compensate for the thickness of the extra layer of elements. *FEMAK* supports axial symmetry, so only half of the cross-section in Fig. 3.2 is included in the model.

The output of the *FEMAK* simulations is the complex pressure at each node. To calculate the specific impedance at a node facing the incoming wave, the axial velocity across the corresponding element m is needed. By Eq. (3.8), with $\phi = 0 = k_\mathrm{s}$ and $\sigma \approx 0$, the velocity is

$$u_m = -\frac{1}{\mathrm{j}\omega\rho_0}\cdot\frac{\partial p}{\partial z} \approx -\frac{1}{\mathrm{j}\omega\rho_0}\cdot\frac{p_{m,2}-p_{m,1}}{\Delta z_m}, \tag{3.14}$$

if the microhorn axis is in the z direction. Here, Δz_m is the axial length of element m, and $p_{m,1}$ and $p_{m,2}$ are the pressures at the front and rear side of the element. The average specific impedance z_mh at the front microhorn opening is then calculated as the average of the specific impedance at the front node of each element,

$$z_\mathrm{mh} = \frac{1}{N}\sum_{m=1}^{N}\frac{p_{m,1}}{u_m} = -\mathrm{j}\omega\rho_0\frac{1}{N}\sum_{m=1}^{N}\frac{p_{m,1}}{p_{m,2}-p_{m,1}}\Delta z_m, \tag{3.15}$$

where N is the number of elements that sees the incoming wave. The acoustic impedance of the microhorn panel absorber is then, with the addition of the outer end correction,

$$Z_\mathrm{mh} = \frac{z_\mathrm{mh}}{\pi r_0^2} + Z_{\mathrm{end,outer}}, \tag{3.16}$$

and the absorption coefficient for the panel is calculated by Eq. (3.7) as before.

Unfortunately, the results in Sec. 3.3.1 indicate that *FEMAK* cannot handle the porous material element type when used like this. The predicted absorption coefficient of the resonator system is predicted to be approximately zero. It seems that the equivalent fluid model implemented in *FEMAK* is not suited for "porous materials" with such low flow resistivities as used here.

3.1.3 Finite Difference Method

Here, the Finite Difference Method [see *e. g. Zienkiewicz and Morgan*, 1983, Ch. 1] is applied to the linear Navier-Stokes equation, Eq. (2.34), and the mass conservation equation, Eq. (3.9) (with $\phi = 1$). With cylindrical coordinates, and assuming rotational symmetry of the horn, the velocity vector can be written as $\mathbf{u}(r,z) = u(r,z)\,\hat{\mathbf{r}} + v(r,z)\,\hat{\mathbf{z}}$, and the pressure as $p(r,z)$. The equations to be solved for p, u and v, are then [*Landau and Lifshitz*, 1959, § 15]

$$\begin{aligned} \mathrm{j}\omega\rho_0 u + \frac{\partial p}{\partial r} - \mu\left(\frac{\partial^2 u}{\partial r^2} + \frac{\partial^2 u}{\partial z^2} + \frac{1}{r}\frac{\partial u}{\partial r} + \frac{u}{r^2}\right) &= 0 \\ \mathrm{j}\omega\rho_0 v + \frac{\partial p}{\partial z} - \mu\left(\frac{\partial^2 v}{\partial r^2} + \frac{\partial^2 v}{\partial z^2} + \frac{1}{r}\frac{\partial v}{\partial r}\right) &= 0 \\ \mathrm{j}\omega p + \rho_0 c_0^2\left(\frac{\partial u}{\partial r} + \frac{\partial v}{\partial z} + \frac{u}{r}\right) &= 0 \end{aligned} \tag{3.17}$$

The equations are solved in the outer part of the horn, $0 < z < h$, as shown in Fig. 3.3. The specific impedance at $z = h$ is an input parameter to the FDM model. The outer part of the horn is divided into M axial steps of length $\Delta z = h/M$. Thus, there are $M+1$ rows of grid points, in the range $m = 0 \ldots M$. The shape of the horn is given by the arbitrary function $r(z)$, as before. Due to the shape of the horn, the total number of grid points increases sharply as the number of radial steps at the inner end of the tube increases. The number of radial steps at $m = M$, denoted $L(M)$, is therefore limited by the available computing resources. To ensure that no grid point is "wasted" at the surface of the horn, where the particle velocity is known to be exactly zero, the radial step length Δr is set equal to $r_h/\left[L(M) + 0.05\right]$, so that the grid point $(M, L(M))$ is close to, but not exactly *at*, the surface. The number of radial grid points for row m, that is $L(m)+1$, is the nearest higher integer to $r(m\Delta z)/\Delta r$.

With the velocity at the grid point (l,m) written as $\mathbf{u}_{l,m} = u_{l,m}\hat{\mathbf{r}} + v_{l,m}\hat{\mathbf{z}}$ and the pressure as $p_{l,m}$, the boundary conditions of the FDM model can be expressed as follows:

– Symmetry at the central axis ($l = 0$):

$$\begin{aligned} u_{0,m} &= 0 & v_{-1,m} &= v_{1,m} \\ u_{-1,m} &= -u_{1,m} & p_{-1,m} &= p_{1,m} \end{aligned} \tag{3.18}$$

Note the sign change of the radial velocity component u.

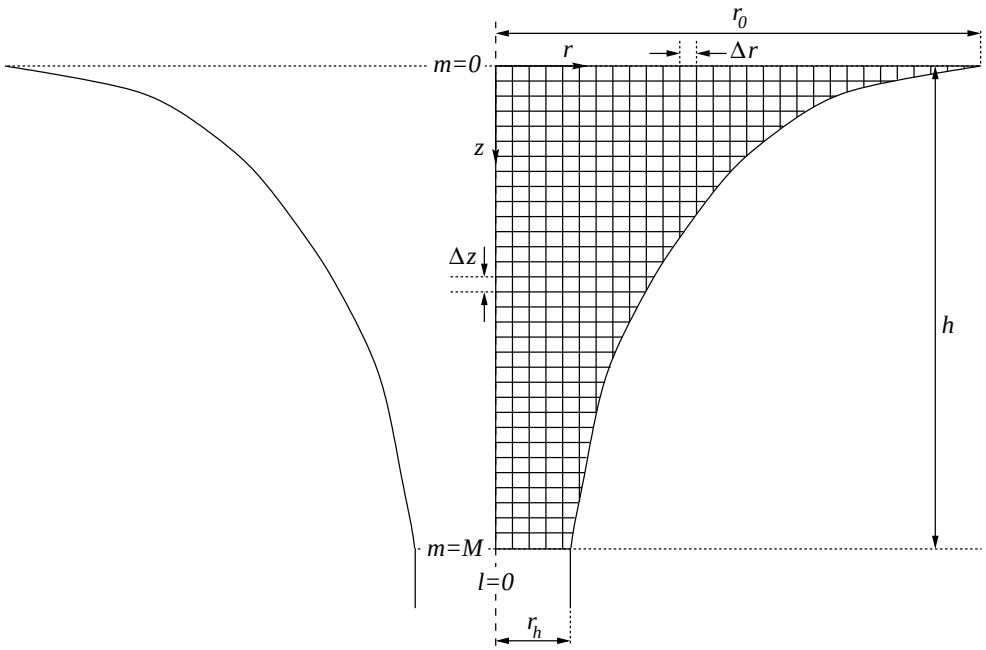

Figure 3.3: *The Finite Difference Method was used to solve Eqs. (3.17) for pressure p and particle velocity* **u** *in the hatched region. The grid shown is not the actual grid used. The specific impedance at $m = M$ is an input parameter to the model.*

– Constant sound pressure p^0 and axial flow in front of outer opening ($m < 0$):

$$\begin{aligned} p_{l,-1} &= p^0 & v_{l,-1} &= v_{l,0} \\ u_{l,-1} &= 0 \end{aligned} \tag{3.19}$$

Equations (3.17) are linear, thus the impedance at any point is independent of p^0. The value of p^0 is therefore arbitrary, and is set to $p^0 = 1$.

– Constant specific impedance z_M at the boundary of the inner part of the horn ($m = M$), and axial flow in the inner part ($m > M$):

$$\begin{aligned} p_{l,M} &= z_M v_{l,M} & v_{l,M+1} &= v_{l,M} \\ u_{l,M+1} &= 0 & p_{l,M+1} &= p_{l,M} \end{aligned} \tag{3.20}$$

Here $z_M = \pi r_h^2 \left(Z_{\text{air}} + Z_{\text{end,inner}} + Z_{\text{inner}} \right)$, by Eqs. (3.5), (3.4) and (3.2).

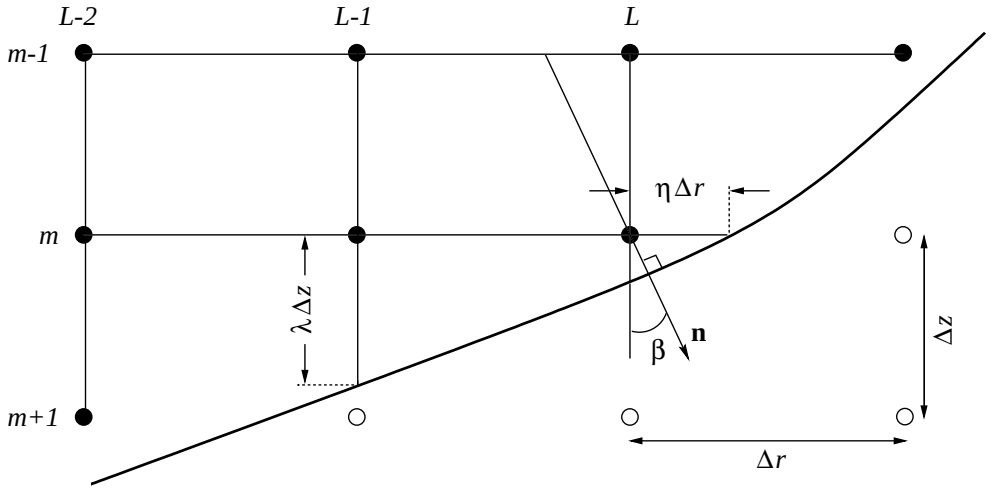

Figure 3.4: *Grid points close to the curved surface of the microhorn, that is points where* $\eta < 1$ *or* $\lambda < 1$*, are excluded from normal treatment by the Finite Difference Method. The pressure and velocity at these special points are determined by boundary conditions and neighboring points, as described by Eqs. (3.22) and (3.23).*

– The horn surface is hard, and there is no slip of the viscous flow:

$$\left.\frac{\partial p}{\partial n}\right|_{\text{surface}} = 0 \qquad \mathbf{u}|_{\text{surface}} = 0, \tag{3.21}$$

where $\partial p/\partial n$ is the derivative of the pressure in the direction of a vector **n** normal to the surface.

Because of the curved surface, points close to the surface have to be treated specially, with a procedure summarized by *Crandall* [1956]. Figure 3.4 shows the geometry. Points "close to the surface" are defined as points (l,m) where $l > L\,(m+1)$ or $l = L\,(m)$, *i. e.* grid points which lacks neighboring grid points either below or to the right. The velocity and pressure at such points are determined by the boundary conditions and the values of the neighboring points. The pressure at (l,m) is given by

$$p_{l,m} = \begin{cases} p_{l,m-1}\left(1-\tan\beta_{l,m}\right) + p_{l-1,m-1}\tan\beta_{l,m} & \text{if} \quad \beta_{l,m} \le \arctan\frac{\Delta r}{\Delta z} \\ p_{l-1,m}\left(1-\cot\beta_{l,m}\right) + p_{l-1,m-1}\cot\beta_{l,m} & \text{if} \quad \beta_{l,m} > \arctan\frac{\Delta r}{\Delta z}, \end{cases} \tag{3.22}$$

where $\beta_{l,m}$ is the angle between the z-axis and the normal vector **n** from the point (l,m) to the surface. The velocity at (l,m) is

$$\mathbf{u}_{l,m} = \begin{cases} \frac{\lambda_{l,m}}{1+\lambda_{l,m}}\mathbf{u}_{l,m-1} & \text{if} \quad L\,(m+1) < l < L \\ \frac{\eta_m}{1+\eta_m}\mathbf{u}_{l-1,m} & \text{if} \quad l = L \end{cases} \tag{3.23}$$

For $m = M$, the value of $\lambda_{l,M}$ is undefined, so only the latter expression is used.

When the pressure and velocity at all grid points have been determined, the impedance at the front opening of the microhorn is given by the average of the specific impedance at grid points at $z = 0$, with the addition of the outer end corrections (see Eq. (3.3)):

$$Z_{\mathrm{mh}} = \frac{1}{\pi r_0^2 [L(0)+1]} \sum_{l=0}^{L(0)} \frac{p_{l,0}}{v_{l,0}} + Z_{\mathrm{end,outer}} \tag{3.24}$$

The absorption coefficient of the microhorn panel absorber is given by Eq. (3.7).

The FDM model is probably the most reliable of the three presented models, but the usefulness and accuracy is limited for the typical microhorn geometries in question. To model the viscous flow in the inner part of the horn correctly, the grid size has to be quite small. Due to the shape of the horns, the computation time and memory requirements makes it inconvenient to investigate a wide range of geometries, and practically impossible to increase the number of grid points to an optimal level.

The three models presented above were primarily meant to give a *qualitative* description of different microhorn geometries, and were not expected to be quantitatively correct. Therefore, the end corrections Z_{inner} and Z_{outer} were not corrected by Eq. (2.15) or Eq. (2.44).

3.2 Measurements and simulations

3.2.1 Measured dimensions of samples

Microhorn panel dimensions

Due to the limitations of the models presented above, only one microhorn panel was produced for impedance measurements. The panel, sized 200×200 mm, and 1 mm thick, were made of aluminium. Horns were punched $b = 15$ mm apart in a rectangular grid. At the bottom of each horn, a hole with diameter approximately 0.5 mm was drilled.

The models require accurate values of the dimensions of the perforations in the panel, including the radius vs. depth function $r(z)$. To determine this function for the perforations in the sample panel, glue was used to make molds from three of the perforations. The glue used was *Super Epoxy 120*. The molds were then measured on a *Hilger & Watts* projector screen, type 601.301, with $50\times$ magnification. The measured dimensions of the three perforations were quite similar, therefore the average of the dimensions was used. The inner perforation diameter was found to be $2r_h \approx 0.55$ mm wide. The outer diameter was measured to $2r_0 \approx 3.9$ mm. The depth of the horn was approximately $h \approx 2.3$ mm. The value of inner perforation length l would seem to be zero, but the exact value could not be determined from the molds. Figure 3.5 shows the average of the measured radius of the horn as function of depth. Given the constraints $r(0) = r_0$ and $r(h) = r_h$ for the given h, a curve fitting to the measured $r(z)$ was attempted. Several functions were tried, *e. g.* a quadratic dependency and a polynomial fit. The closest fit to the measured shape of the horn was the logarithmic function

$$r_{\log}(z) = r_h - \frac{1}{K} \ln\left[\frac{z}{h} + \left(1 - \frac{z}{h}\right) \mathrm{e}^{-K(r_0 - r_h)}\right], \tag{3.25}$$

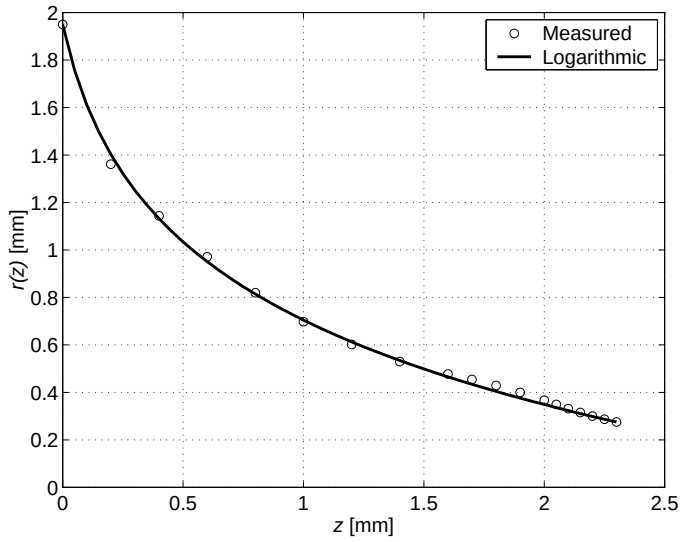

Figure 3.5: *Radius $r(z)$ of horn as function of depth. Measured data compared to the logarithmic function Eq. (3.25)*

with the arbitrary constant K set to $1795\,\mathrm{m}^{-1}$ by the method of least squares. This function is also shown in Fig. 3.5. To evaluate the influence of the shape of the horn, the linear function

$$r_{\mathrm{lin}}(z) = r_0 + (r_h - r_0)\,\frac{z}{h}, \tag{3.26}$$

corresponding to a conical horn shape, was also used in the simulations. To supplement the measurements of the molds, some of the microhorns were also examined in microscope. It was found that the perimeter of the inner perforation was jagged and only remotely circular.

The method used to measure the microhorn panel geometry introduced several *possible* errors, all of which may decrease the accuracy of the predictions by the models:

- The properties of the glue during hardening and changes in temperature are not known. If the glue shrunk during hardening, the measured values of $r(z)$ and h are too small.
- The inner part of the mold may have broken, or the glue may not have completely filled the horn. The result will be a too high measured value of r_h and a too low value of h.
- The projections of the molds were measured manually with a ruler. The random errors thus introduced are only partly compensated for by taking the average of the molds.
- Because of the importance of the value of r_h, a small error in the projection magnification may also introduce significant errors. By use of a known sample, the error in the projection system was found to be less than $0.02\,\mathrm{mm}$.

After the initial measurements, it was found that a panel vibration mode interfered with the Helmholtz resonance. To eliminate this problem, steel bars of dimension 5×5 mm were glued to the rear side of the panel. The stiffness thus introduced caused the frequency of the vibration mode to shift to a higher frequency.

Microperforated panel dimensions

An ordinary microperforated panel was also measured to compare with the microhorn panel. The MPP thickness, and perforation length, was $l = 1$ mm. Like the microhorn panel, the perforations were drilled in a rectangular grid, with $b = 15$ mm between the perforations. The diameter of the perforations in this panel was measured in microscope. It was found that $2r \approx 0.52$ mm. As for the microhorn panel, steel bars had to be glued to the rear side to avoid interference between plate vibration modes and the Helmholtz resonance.

3.2.2 Impedance measurements in Kundt's tube

The specific impedance at normal sound incidence of the microhorn panel and the ordinary MPP was measured in a Kundt's tube with square cross-section. The standardized transfer-function method was used [*Chung and Blaser*, 1980; *ISO 10534-2*, 1996; *Jones and Stiede*, 1997]. Figures 3.6, 3.7 and 3.8 show an overview of the measurement setup, the mounting of the sample, and the relevant dimensions, respectively. The specific impedance is given by

$$z = \mathrm{j}\rho_0 c_0 \frac{H_{12}\sin kt - \sin k(t-s)}{\cos k(t-s) - H_{12}\cos kt}, \tag{3.27}$$

where H_{12} is the measured transfer function H_{12} between the microphones, s is the distance between the microphones, and t is the distance between the front microphone and the sample. The inner dimension of the tube is 200×200 mm, with the lowest cut-off frequency at 850 Hz [*Morse and Ingard*, 1968, Ch. 9.2]. The measurements were done with *Brüel & Kjær* condenser microphones, type 4165. The distance t was 310 mm, and the microphone distance was $s = 150$ mm. According to *Boden and Åbom* [1986] and *Nordtest ACOU 095* [1996], this corresponds to a recommended frequency interval 113 – 907 Hz. Outside this frequency range, the maximum error in H_{12} increases sharply. The samples were fastened with screws to a square sample holder. The inner width and height of the sample holder is 190 mm, and the thickness (*i. e.* length along the tube axis) is 10 mm. The outer edge has a rubber band placed in a groove, to decrease leakage between the sample holder and the tube wall. Four values of the back cavity depth d were used; 44, 79, 149 and 219 mm. Only the results for $d = 44$ mm are presented and compared with simulations in Sec. 3.3 below.

The transfer function H_{12} was measured by the computer program *WinMLS* developed by *Morset Sound Development* [1999]. This program implements the Maximum Length Sequence (MLS) method [see *e. g. Chu*, 1990]. The PC had a *Hohner* ARC 44 sound card with four channels, three of which were used here. For all measurements and calibrations, the sampling rate was 11025 Hz, the sequence order 14, and the number of averages was 16.

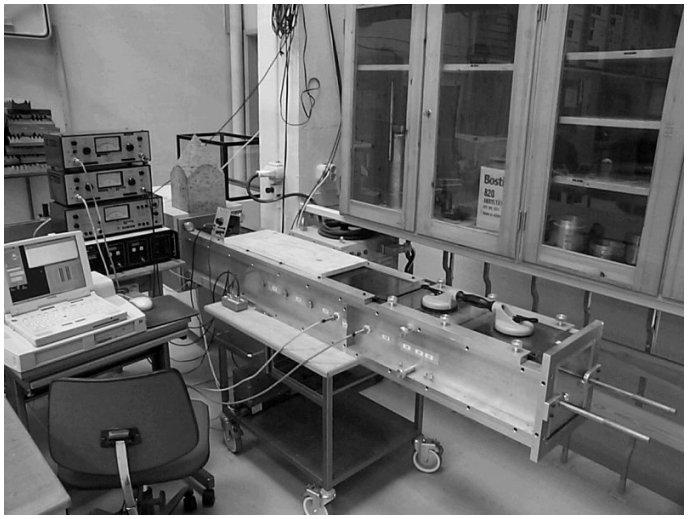

Figure 3.6: *The Kundt's tube, with microphone amplifiers to the left. Two of the tube walls, and also the movable "piston" which constitute the back wall, are made of glass. This allows for visual control of the mounted sample, and also vibration measurements by laser interferometry, as described in Ch. 4. In the background can be seen the anechoic end piece used during the calibration.*

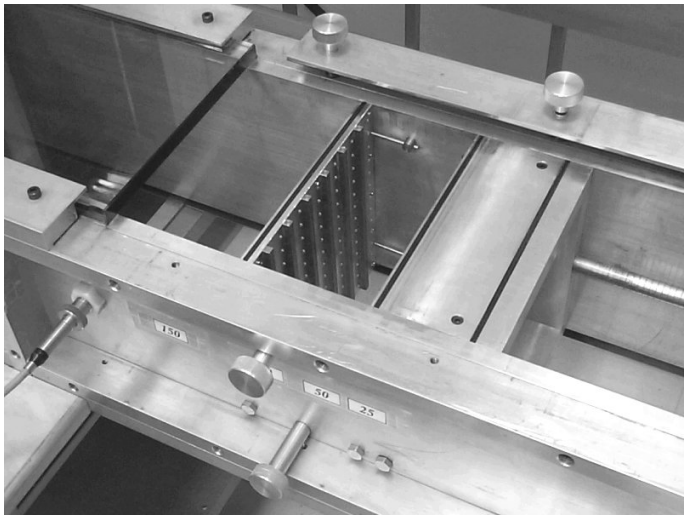

Figure 3.7: *The microhorn panel and sample holder, with tube top cover removed. The sample holder was held in place by pins near the corners. The reflecting end piece can be put in any position, only limited by the pins and the length of the tube.*

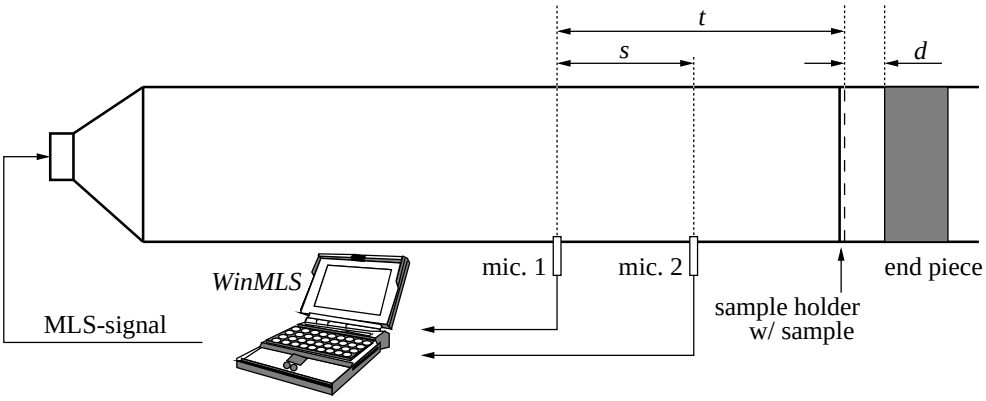

Figure 3.8: *The setup used for normal incidence impedance measurements of the microhorn panel and the MPP. The transfer function between the microphones was calculated by the computer program* WinMLS *[*Morset Sound Development*, 1999]. During all measurements,* $t = 310\,\text{mm}$ *and* $s = 150\,\text{mm}$*. Four values of d were used; 44, 79, 149 and* 219 mm*.*

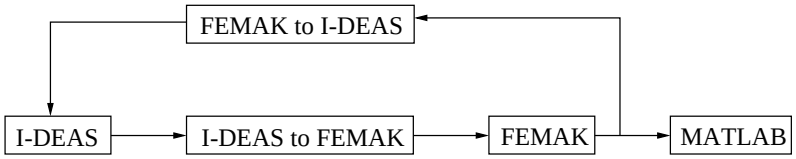

Figure 3.9: *Flowchart for the Finite Element Method simulations process. The geometry is defined in the CAD-program* I-DEAS*, and is translated into a form appropriate for* FEMAK *by a conversion program. The output is processed by* MATLAB*, but may also be returned to* I-DEAS *for graphical representation.*

3.2.3 Simulations

The simulations by the Finite Element Method were done on two different geometries. The first was a microhorn with dimensions like the measured microhorn panel. The *FEMAK* input file was generated by the CAD-program *I-DEAS* [*Lawry*, 1998; *SDRC Solutions*, 2000], with an appropriate conversion program [*Verdeille*, 1998a,b], as indicated in Fig. 3.9. The elements were approximately $0.05 \times 0.05\,\text{mm}$. The simulations were done at $1/3$ octave spaced points in the frequency range $31.5 - 1600\,\text{Hz}$. The other geometry was an ordinary MPP, with perforation diameter $0.5\,\text{mm}$, thickness $1\,\text{mm}$, and with $4\,\text{mm}$ spacing between perforations. The distance to the hard wall was $200\,\text{mm}$. The perforations were assumed to be filled with a porous material, and the flow resistivity of this material was varied. For this geometry, the *FEMAK* input file was written manually. The elements were $0.125\,\text{mm}$ wide in the radial direction. In the axial direction, the length was $0.25\,\text{mm}$ for the porous material

Table 3.1: *Values of geometry parameters used in Finite Difference and Integration Method simulations of microhorn, first series. The back cavity depth d was* 44 mm.

Parameter	Values used mm		
h	1	2	
l	0	0.2	0.5
r_0	1	2	5
r_h	0.25	0.50	

Table 3.2: *Values of geometry parameters used in Finite Difference simulations of microhorn, second series. Outer horn radius $r_0 = 1.95$ mm and length $h = 2.3$ mm for all simulations. Only horn shape function $r_{\log}$ was used. The back cavity depth d was* 44 mm.

Parameter	Values used mm			
l	0	0.1	0.2	0.3
r_h	0.250	0.260	0.265	0.275

elements, and 1 mm for the ordinary air elements at each perforation aperture. The simulation frequency range was $224 - 800$ Hz, with $1/6$ octave spaced points.

Two series of Finite Difference Method simulations were carried out. The *first* series was intended to illustrate the influence of large variations in the microhorn geometry on the absorption characteristics. The dimension parameters and the values used in the simulations are given by Table 3.1. Both shape functions, $r_{\log}$ given by Eq. (3.25) and r_{lin} given by Eq. (3.26), were used in these simulations, except for $r_0 = 5$ mm. This large outer radius in combination with the conic horn shape (r_{lin}) could not be simulated due to the extensive computer memory requirements. Simulations with $h = 5$ mm were originally planned, but could not be completed. This was also due to the large memory requirements. The *second* series of FDM simulations was intended to simulate the measured microhorn panel sample and investigate the sensitivity to small variations in the horn dimensions. The parameters of the second series are given in Table 3.2. For all the FDM simulations, the number of z-steps were $M = 70$, and the number of r-steps at $z = h$ were $L_M = 9$. These values were chosen to give a relatively square grid for dimensions close to the measured sample. With $h = 2.3$ mm and $r_h = 0.275$ mm, the grid lengths are $\Delta r \approx \Delta z \approx 0.03$ mm. At $f = 200$ Hz this is equivalent to 5 radial grid points inside the viscous boundary layer at $z = h$. The simulations were done at $1/3$ octave spaced points in the frequency range $31.5 - 800$ Hz.

The simulations by the Integration Method were assumed to give quick, approximatively correct predictions of the absorption coefficient of various microhorn geometries. This was

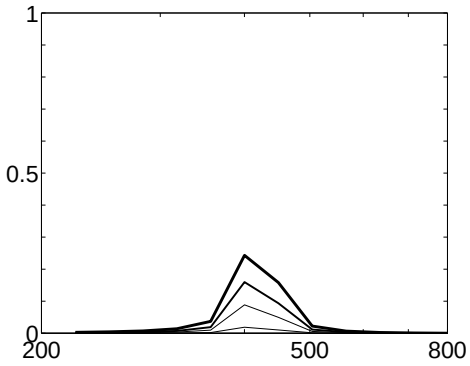

Figure 3.10: *Finite Element simulations of micro-perforation filled with porous material (see page 37). Absorption coefficient as function of frequency for different flow resistivities.* ——, $\sigma = 1\,\mathrm{kPas/m^2}$; ——, $\sigma = 5\,\mathrm{kPas/m^2}$; ——, $\sigma = 10\,\mathrm{kPas/m^2}$; ——, $\sigma = 20\,\mathrm{kPas/m^2}$.

not the case (see Sec. 3.3.1), so simulations by the IM were only done for the geometries in Table 3.1, with the same frequency range as used in the FDM simulations, and with $1/6$ octave spacing between the points.

The absorption coefficient of the microperforated panel sample was calculated by the computer program *FLAG*, developed at NTNU [*Vigran et al.*, 1991]. This program implements the transfer matrix method [see *e. g. Dunn and Davern*, 1986; *Brouard et al.*, 1995] for a number of materials, including MPPs. The MPP implementation in *FLAG* is based on Eq. (2.46). Unlike *Melling* [1973], the MPP implementation in *FLAG* uses only the standard value for the viscosity. *Stinson and Shaw* [1985] stated that the use of an "effective" viscosity, which includes the effect of thermal losses, is only appropriate for long tubes. Additionally, the polynomial coefficients used in *FLAG* differs from those given in Eq. (2.45). The geometry parameters used in the *FLAG* simulation of the MPP were the same as the physical dimensions given in Sec. 3.2.1. The *FLAG* program was also used to simulate MPPs with resonance frequencies approximately equal to that of the measured microhorn panel sample. For this, the dimensions of the MPPs were (a) $r = 0.250\,\mathrm{mm}$, $A = 120\,\mathrm{mm^2}$, (b) $r = 0.275\,\mathrm{mm}$, $A = 140\,\mathrm{mm^2}$ and (c) $r = 0.325\,\mathrm{mm}$, $A = 190\,\mathrm{mm^2}$. For all *FLAG* simulations, d was 44 mm and l was 1 mm. The simulations were done at $1/30$ octave spaced points in the frequency range $35 - 1094\,\mathrm{Hz}$.

3.3 Results

3.3.1 Comparison of simulation methods

The predicted absorption coefficient of the FEM simulation of the microhorn was practically zero for all frequencies. To verify that this result was not an error in the geometry definition or conversation process, a simpler geometry was defined. Figure 3.10 shows the result of decreasing the flow resistivity of a porous material in a micro-perforation. The procedure

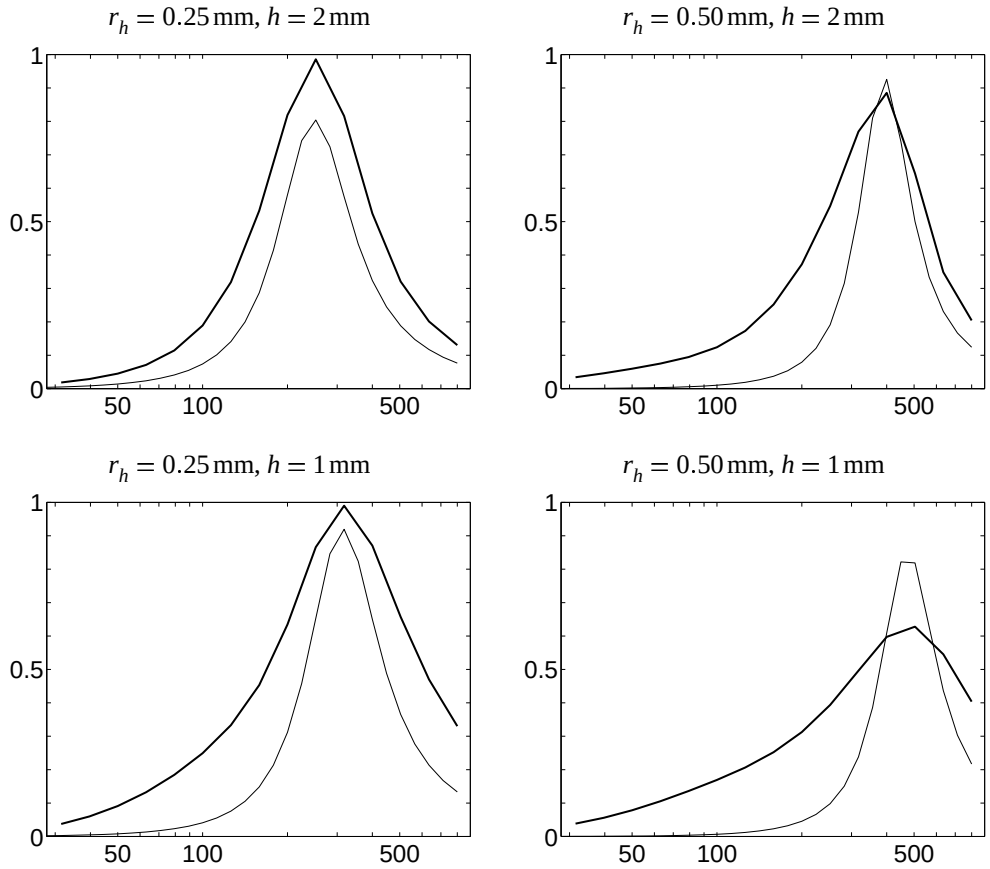

Figure 3.11: *Simulations of microhorn geometries. Absorption coefficient as function of frequency as calculated by the Integration Method and the Finite Difference Method. Inner horn length* $l = 0\,\text{mm}$, *outer horn radius* $r_0 = 2\,\text{mm}$ *for all graphs.* ——, *Integration Method;* ▬▬, *Finite Difference Method.*

in Sec. 3.1.2 obviously fails to predict the absorption characteristics of a simple MPP, when the flow resistivity is given by Eq. (3.13). It seems that, to simulate perforates correctly, the program *FEMAK* requires some resistive material to supply the required resistance, as were done by *Kristiansen and Vigran* [1994].

As mentioned in Sec. 3.1.1, the Integration Method can only be viewed as an approximate model, if only due to the inferior modelling of the velocity field in the horn. This is confirmed in Fig. 3.11, which compares simulations by the IM and the Finite Difference Method. Only the geometries with l, r_0 and $r(z)$ approximately equal to the experimentally tested sample, *i. e.* $l = 0\,\text{mm}$, $r_0 = 2\,\text{mm}$ and $r(z) = r_{\log}$, are presented in this figure. In contrast to the FDM results, and in contrast to what could be expected, the IM results seems relatively insensitive to variation of h and r_h. The same mismatch between the models is also evident for the

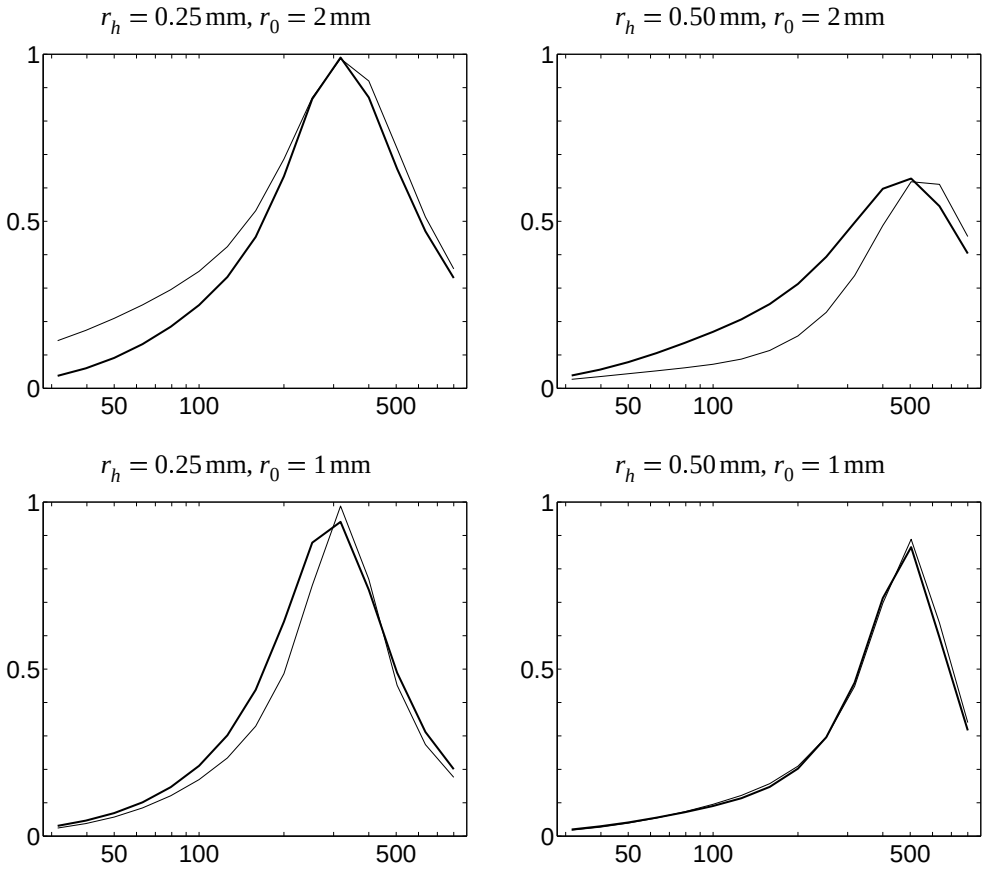

Figure 3.12: *Finite Difference simulations of microhorn geometries. Absorption coefficient as function of frequency for horn shapes* $r_{\log}$ *and* r_{lin}. *Inner horn length* $l = 0\,\text{mm}$, *outer horn length* $h = 1\,\text{mm}$ *for all graphs.* ——, $r(z) = r_{\text{lin}}(z)$ *given by Eq. (3.26);* ——, $r(z) = r_{\log}(z)$ *given by Eq. (3.25).*

geometries not shown, where $l = 0.2$ and $0.5\,\text{mm}$ and $r_0 = 1$ and $5\,\text{mm}$. Consequently, in the following sections only the FDM results are presented.

3.3.2 Variation of horn geometry

Horn shape

The effect of the shape of the horn is illustrated in Figs. 3.12 and 3.13, where the horn shapes $r_{\log}$ and r_{lin} are compared. The two figures correspond to $h = 1$ and $2\,\text{mm}$, respectively. For simplicity, l is $0\,\text{mm}$ for all graphs. Simulations of geometries with $r_0 = 5\,\text{mm}$ were also attempted, but could not be completed because FDM simulations with horn shape r_{lin} requires even more memory than $r_{\log}$. As could be expected, the results show that the horn

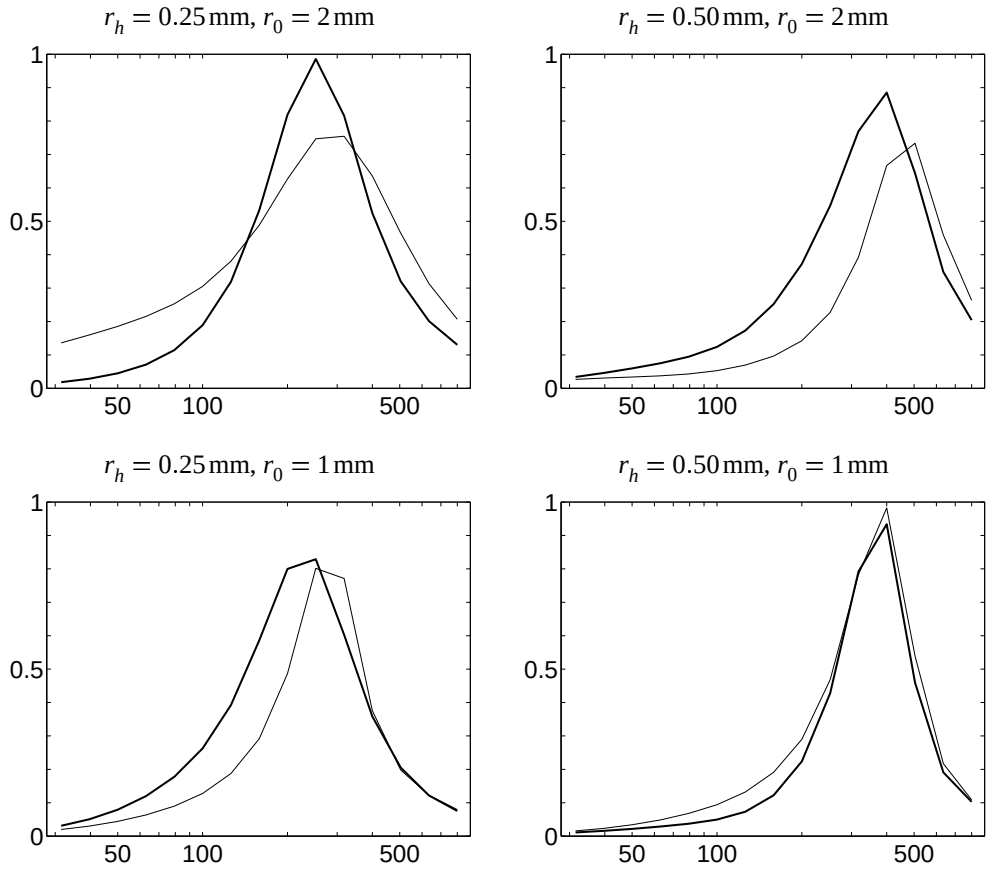

Figure 3.13: *Finite Difference simulations of microhorn geometries. Absorption coefficient as function of frequency for horn shapes* $r_{\log}$ *and* r_{lin}. *Inner horn length* $l = 0\,\mathrm{mm}$, *outer horn length* $h = 2\,\mathrm{mm}$ *for all graphs.* ——, $r(z) = r_{\mathrm{lin}}(z)$ *given by Eq. (3.26);* ——, $r(z) = r_{\log}(z)$ *given by Eq. (3.25).*

shape is of greater importance for the longer horns (Fig. 3.13), and even more so for horns with large r_0 or small r_h. It is less intuitive that the resonance frequencies generally are *higher* for conic horns than for logarithmic horns. This is despite the fact that the volume (and hence the nominal mass) of the conic horn is significantly larger than the volume of the logarithmic horn, given the same values of r_0, r_h and h. The reason for the difference in resonance frequency is probably that a logarithmic horn has a *longer* narrow portion of the horn length than a conic horn. As discussed by Craggs and Hildebrandt (see page 14), the effective density of air in narrow tubes can be up to $\rho_{\mathrm{e}} = 1.33\rho_0$ for small values of x. Hence, in some cases, the effective mass of the logarithmic horn may be larger than the effective mass of the conic horn.

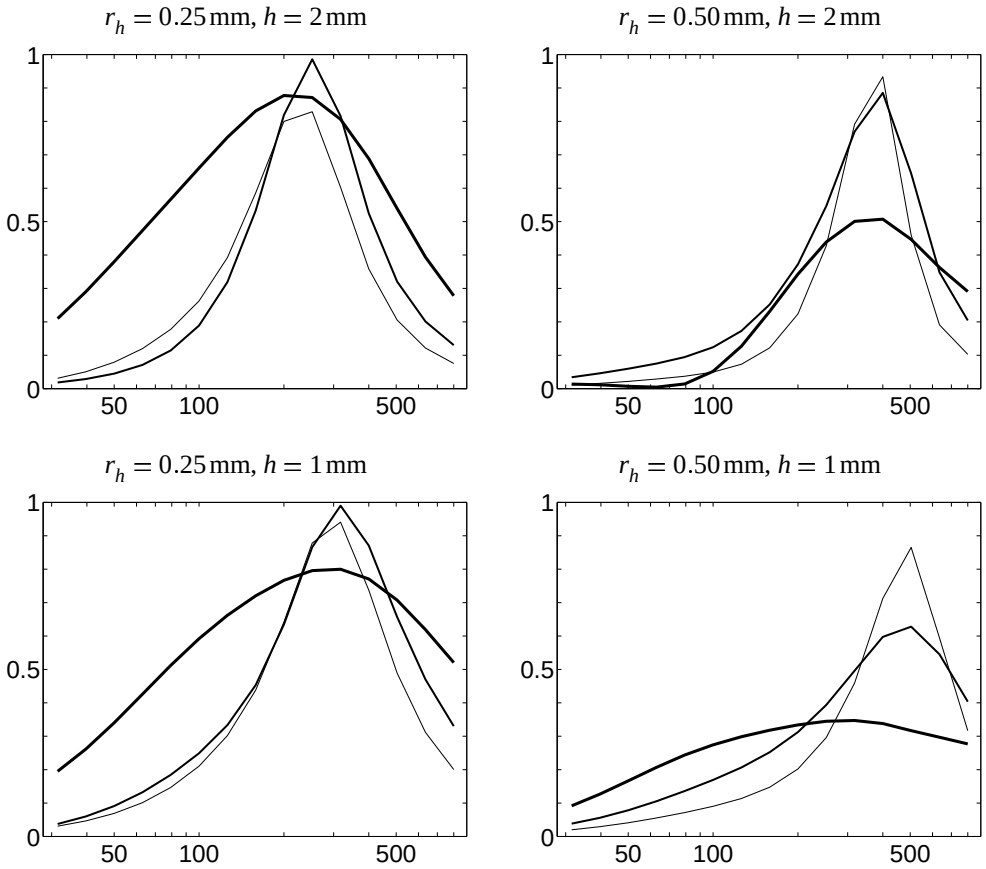

Figure 3.14: *Finite Difference simulations of microhorn geometries. Absorption coefficient as function of frequency for different outer radii* r_0. *Inner horn length* $l = 0\,\text{mm}$ *for all graphs.* ——, $r_0 = 1\,\text{mm}$; ▬, $r_0 = 2\,\text{mm}$; ▬, $r_0 = 5\,\text{mm}$.

Horn dimension

The sensitivity to variation in the horn dimensions r_0, r_h, h and l, is visualized by Figs. 3.14, 3.15 and 3.16. These figures correspond to $l = 0$, 0.2 and 0.5 mm respectively. By comparing the corresponding graphs in the three figures, it can be seen that the inner horn length l influences the absorption characteristics as expected: an increase in l will in most cases increase the resonance absorption coefficient α_0 due to the increased resistance, and shift the resonance frequency f_0 towards lower frequencies due to the increased (effective) mass. This seems to be the most significant effect of an increase in l. Except for r_h, the effect of the other geometry parameters are relatively independent of l.

An increase in the outer horn radius r_0 will generally decrease the Q-value of the resonance (as was the intended purpose of the horn-shaped orifices). While this is the dominant effect for $r_h = 0.25\,\text{mm}$, the decrease in Q is also accompanied by a decrease in α_0 for

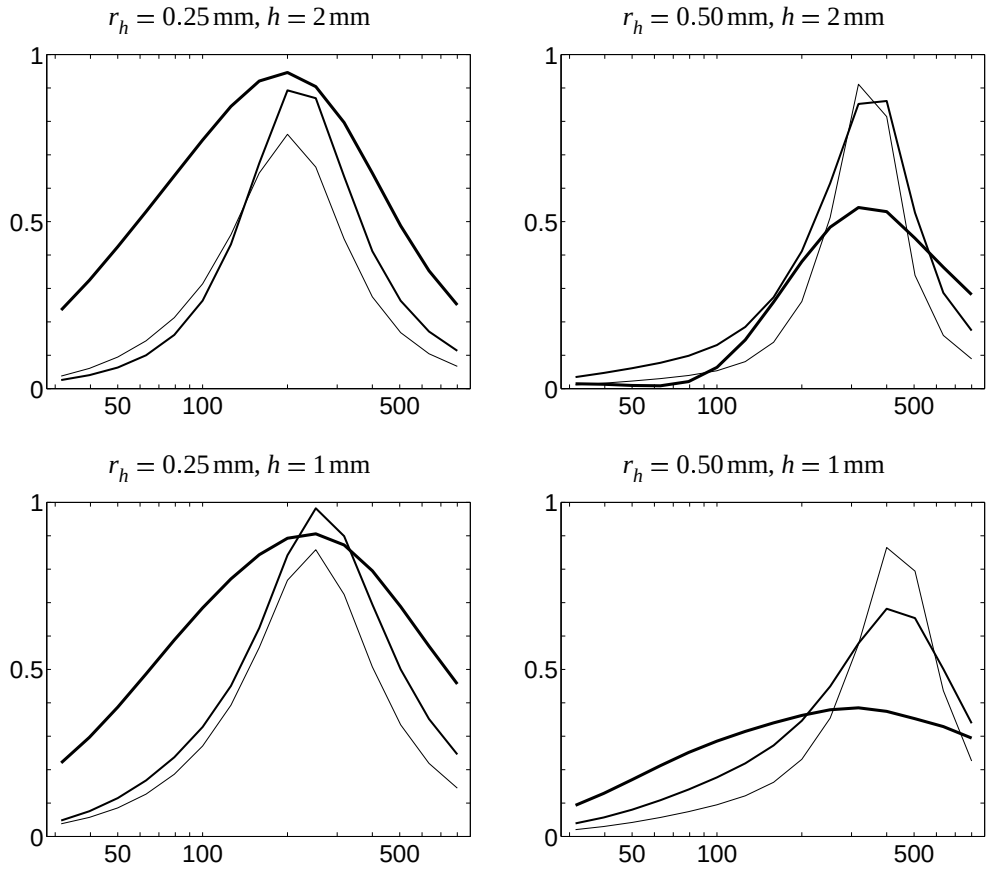

Figure 3.15: *Finite Difference simulations of microhorn geometries. Absorption coefficient as function of frequency for different outer radii* r_0. *Inner horn length* $l = 0.2\,\text{mm}$ *for all graphs.* ——, $r_0 = 1\,\text{mm}$; ——, $r_0 = 2\,\text{mm}$; ——, $r_0 = 5\,\text{mm}$.

$r_h = 0.50\,\text{mm}$, and especially for short outer horns, $h = 1\,\text{mm}$. It seems that although wider outer openings yield a larger flow rate through the horn, this cannot be fully utilized to increase the viscous losses if r_h is large, and especially if h is small. The reduced f_0 that is expected for increased r_0, due to the increased mass in the horn, is also most noticeable for short horns with large inner openings.

The effect of variation in the outer horn length h is dependent on the value of r_0 and r_h. For the *smallest* value of r_0, *i. e.* 1 mm, the outer part of the horn may be considered as mainly an extension of the cylindrical inner part. As was the case with variation in l, an increase in the outer horn length h therefore results in a decrease in f_0 in this case. On the other hand, for the *large* $r_0 = 5\,\text{mm}$, there is also a dependency on the value of r_h. For small inner openings, the main effect of an increase in h is a reduction in f_0, as before. However, for $r_h = 0.50\,\text{mm}$ the energy dissipation in the inner part of the horn is much less, and the increased resistance

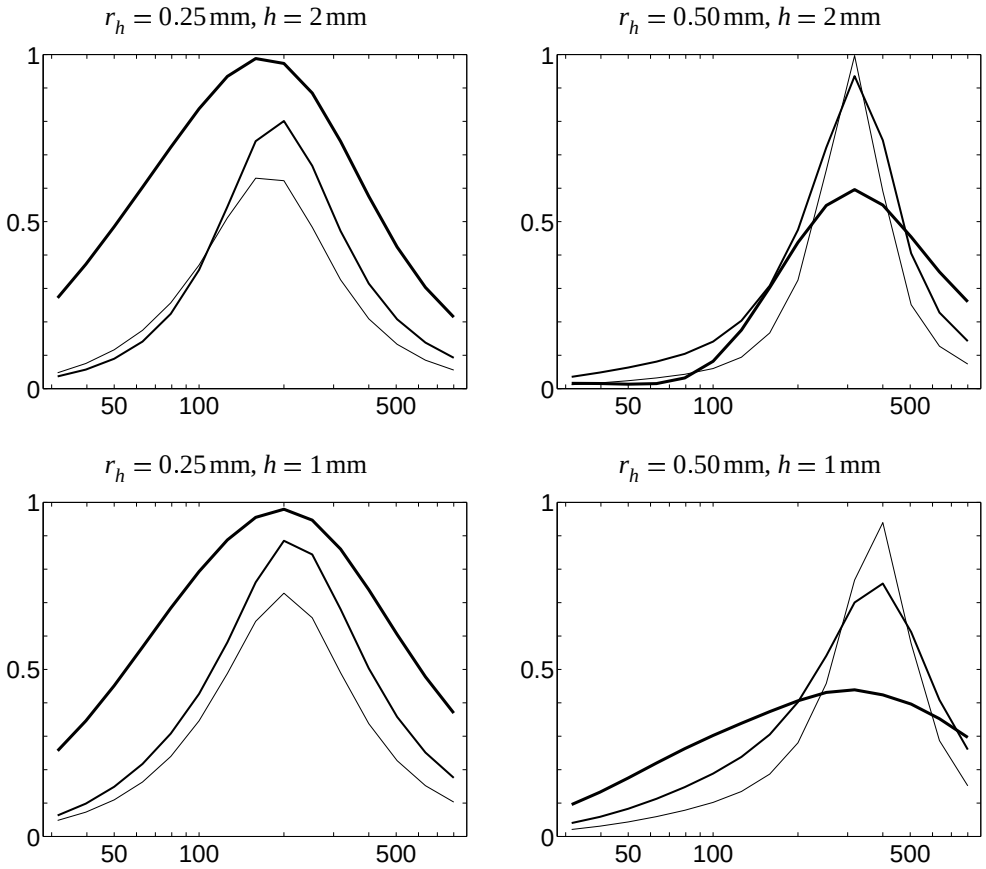

Figure 3.16: *Finite Difference simulations of microhorn geometries. Absorption coefficient as function of frequency for different outer radii* r_0. *Inner horn length* l *is* 0.5 mm *for all graphs.* ——, $r_0 = 1\,\text{mm}$; ——, $r_0 = 2\,\text{mm}$; ——, $r_0 = 5\,\text{mm}$.

caused by an increase in h will become more significant. Hence, α_0 increases. In this case, the resonance frequency is less sensitive to changes in h.

The most critical parameter, r_h, also has the most complex dependency on the other parameters. The only general observation is that the resonance frequency increases with r_h. This is probably because the reduction in the effective mass due to the increase in the perforate constant x is larger than the increase in the nominal mass due to the increased volume of the horn. For large $r_0 = 5\,\text{mm}$, the maximum absorption coefficient decreases for increasing r_h, as expected. For small $r_0 = 1\,\text{mm}$, the effect of r_h depends on h and l. For large $h = 2\,\text{mm}$, or large $l = 0.5\,\text{mm}$ in combination with the short $h = 1\,\text{mm}$, an increase in r_h will increase α_0. On the other hand, for the shortest total horn length, $h = 1\,\text{mm}$, $l = 0\,\text{mm}$, the maximum absorption decreases when r_h increases. It may seem that for the long tubes, the resistance is higher than the optimum, so that an increase in r_h will reduce the resistance to a more optimal

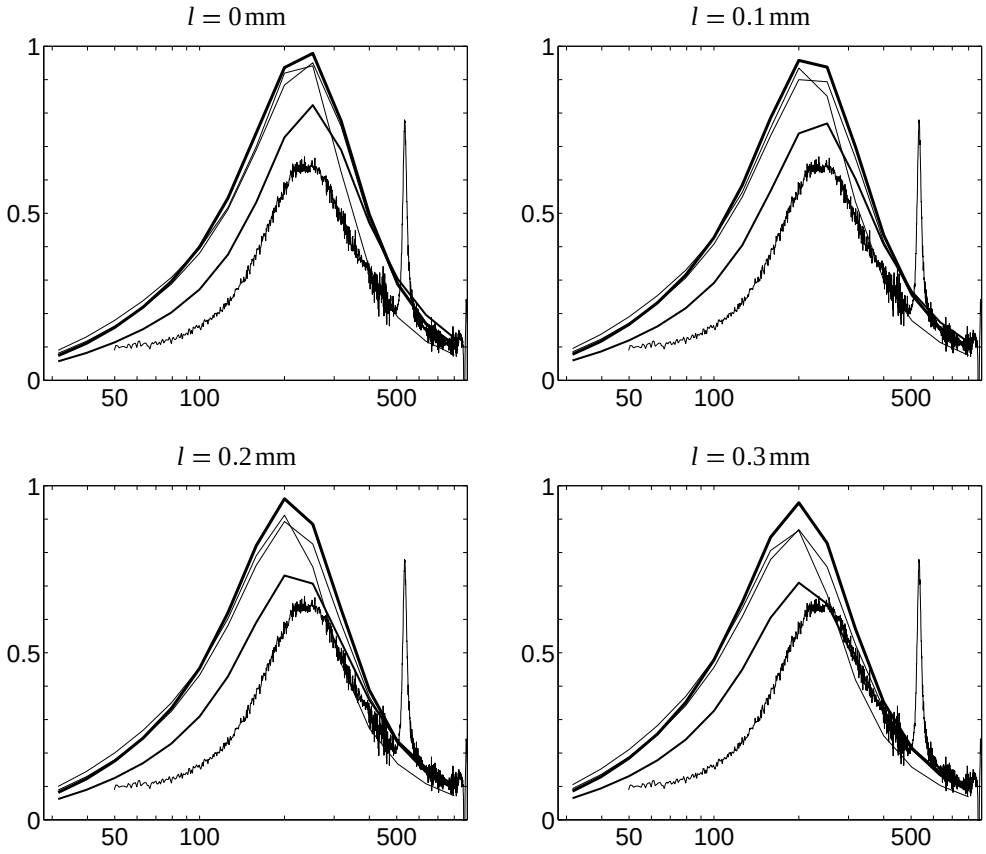

Figure 3.17: *Finite Difference simulations compared to measurement of microhorn panel. Absorption coefficient as function of frequency for small variations in inner radius r_h. Outer horn radius $r_0 = 1.95\,\mathrm{mm}$ and length $h = 2.3\,\mathrm{mm}$ for all graphs. The cavity depth $d = 44\,\mathrm{mm}$.* ——, $r_h = 0.250\,\mathrm{mm}$; ——, $r_h = 0.260\,\mathrm{mm}$; ——, $r_h = 0.265\,\mathrm{mm}$; ——, $r_h = 0.275\,\mathrm{mm}$.

level. For the shorter tubes, the increase in r_h results in less optimal resistance, and hence reduced α_0.

3.3.3 Comparison with measurements

The second series of FDM simulations was intended to illustrate the effect of small variations of the geometry parameters, close to the geometry of the sample panel. The results for different values of l and r_h are shown in Fig. 3.17. With regard to limitation set by the microphone separation, the measured data was cut at 50 Hz. The spikes at $f = 500\,\mathrm{Hz}$ is due to the plate resonance. The figure shows the expected shifting towards lower frequency for increasing l. More interesting, however, is the effect of variations in r_h. An increase in r_h does not *monotonically* reduce the maximum absorption coefficient, but results in an alternation in α_0 and

bandwidth. The alternation pattern is the same for all values of l. It seems that the FDM implementation used here cannot be trusted to give quantitatively correct predictions for small variations of the critical parameter r_h. This is most probably due to the relatively low number of radial grid points. As described in Sec. 3.2.3, for $f = 200\,\text{Hz}$ there are only 5 radial grid points inside the viscous boundary layer at $z = h$. The placement of grid points inside the viscous boundary layer, where the velocity profile is steep, will be significantly affected by a small variation of r_h.

For all values of l except zero, the predicted resonance frequencies are lower than the measured resonance frequency. The simulations also predict absorption peaks which are generally too high and too broad compared to the measurement. There are several possible explanations of the discrepancy:

- The dimensions of the microhorn panel sample may have been inaccurately determined, as mentioned in Sec. 3.2.1. Additionally, the shape of the inner horn openings were observed to be not quite circular. Thus, the real, average inner radius may have been larger than the value of r_h that was used.
- The number of grid points may be too small, so that the energy dissipation in the viscous boundary layer is not modelled correctly.
- The end corrections of the outer horn opening may be incorrect. Due to the shape of the horn, it is difficult to estimate how much of the openings area should be associated with the opening, and how much should be considered as part of the panel surface. A too high r_0 will result in a too high associated mass, leading to a too low resonance frequency.

3.3.4 Comparison with microperforated panels

The left chart in Fig. 3.18 shows the measured absorption coefficient of the microperforated panel sample compared with *FLAG* simulations of the same geometry. The agreement is quite good. Also, given the constraints $d = 44\,\text{mm}$, $r = 0.26\,\text{mm}$ and $f_0 \approx 180\,\text{Hz}$, this seems to be an almost optimal configuration. Several other combinations of A and t were simulated by *FLAG*, but none resulted in significantly higher absorption at the same frequency. The right chart in Fig. 3.18 compares the absorption coefficient of three simulated MPPs with the measured microhorn panel sample. Here too, the dimensions of the simulated MPPs are limited by $d = 44\,\text{mm}$ and $l = 1\,\text{mm}$, and are chosen so that $f_0 \approx 250\,\text{Hz}$.

3.4 Summary

The microhorn concept has been investigated by analytical, numerical and experimental methods. The microhorn concept was thought to increase the absorption bandwidth, compared to the ordinary MPPs. However, the microhorns turned out to be difficult to model with the accuracy required to design reasonable optimal panels for experimental testing. The experiments on the sample that was produced did neither confirm nor reject the feasibility of the microhorn concept.

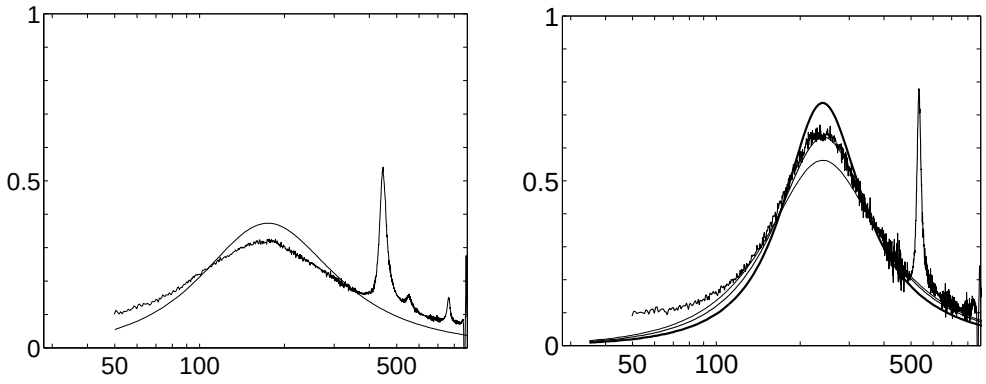

i) MPP ii) Microhorn

Figure 3.18: *Comparison of simulated and measured absorption coefficient as function of frequency for the panel absorber samples.* **i)** FLAG *simulation and measurement of microperforated panel sample. For the simulation,* $r = 0.26\,\text{mm}$, $l = 1\,\text{mm}$, $A = 245\,\text{mm}^2$ *and* $d = 44\,\text{mm}$. **ii)** FLAG *simulations of microperforated panels and measurement of microhorn panel sample. For the simulations,* $l = 1\,\text{mm}$ *and* $d = 44\,\text{mm}$. ——, $r = 0.250\,\text{mm}$, $A = 120\,\text{mm}^2$; ——, $r = 0.275\,\text{mm}$, $A = 140\,\text{mm}^2$; ——, $r = 0.325\,\text{mm}$, $A = 190\,\text{mm}^2$.

Three models were tried to simulate the microhorns. Of these, only the Finite Difference Method could, to some degree, be trusted to give qualitatively correct predictions. Due to limitations in the number of grid points, the FDM results cannot be trusted to be quantitatively correct. According to the FDM simulations, a high maximum absorption coefficient and a high absorption bandwidth can be obtained for geometries where the outer horn radius is large and the inner radius is small. The lengths of the outer and inner parts of the horn, and the shape of the horn, are also significant, but subordinate, factors. Considering the possible sources of error in the FDM simulations, these qualitative statements should nevertheless be correct.

Chapter 4

Double panel absorbers

The subject of study in this chapter is a new type of panel absorber. It is a distributed Helmholtz resonator with double plates, where the plates are perforated with holes or slits. The key idea is to elongate the resonator necks *laterally*, and make the width of these lateral slit-shaped necks so small that viscous losses become significant. Unlike the concept discussed by *Mechel* [1994c], the narrow, lateral slits are not "side branches" to the main resonator neck, but rather an integral part of the neck. Like the microperforated panels [*Maa*, 1987, 1998], this new absorber concept utilizes the viscous losses inherent in the resonator openings. Hence, it does not require extra resistive materials to achieve a relatively broadbanded absorption compared to the simple panel Helmholtz resonators.

The concept is implemented by mounting two parallel, smooth, perforated metal plates close together, separated by a small distance. The perforations form a regular grid, and the perforations in the front plate are at a maximum distance from those in the rear plate. The result is that the resonator necks consist of three segments; front opening, rear opening and the lateral slit formed by the gap between the plates. Figure 4.1 shows a sample of a double panel absorber with circular perforations, as mounted for impedance measurement in a Kundt's tube. Slit-shaped openings are also investigated. In this case, the length of the lateral slit can be varied by lateral displacement of one plate relative to the other plate. The effects of such displacements are also presented.

4.1 Circular perforations

This section describes the initial investigations on the double panel absorber concept, where the perforations were circular, short tubes.

4.1.1 Model

The double panel absorber with circular perforations is here modelled by a simple analytical model. If normal sound incidence is assumed, symmetry allows an imaginary tube of cross-section area $A = b^2$ to be associated with each perforation [*Allard*, 1993, Ch. 10]. Here b

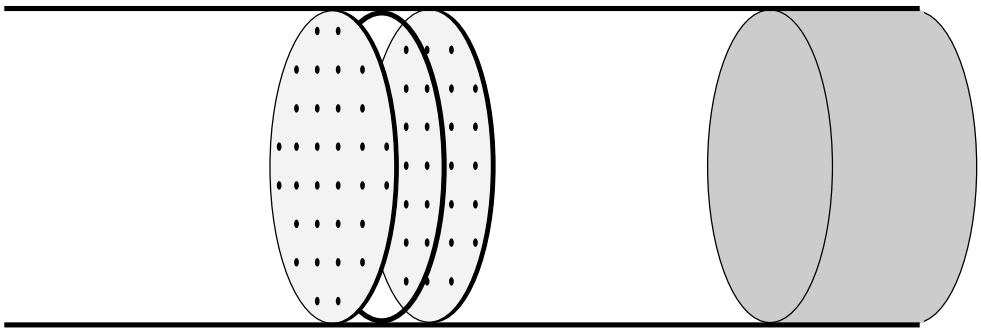

Figure 4.1: *The perforated double panel absorber, as mounted for impedance measurements in a Kundt's tube. The plates are separated by a number of thin metal rings at the perimeter. The openings in the two plates are placed symmetrically with respect to each other to maximize the length of the lateral slit formed by the gap between the plates. The center-center distance between the perforations is the same for both plates.*

is the center-center distance between the perforations. The modelled geometry is shown in Fig. 4.2, where the cross-section of the tube is indicated with a square. As shown in Sec. 2.3.3, the influence of the perforations outside the imaginary tube "walls" can be neglected for perforation cross-section areas S which are significantly smaller than A. For the "worst case" sample used in the measurements, the ratio S/A is 0.01 (see Table 4.1). Fok's function, by Eq. (2.44), is then 1.17. Therefore the effect of interaction between the perforations is excluded from the model.

As shown in Fig. 4.2, the model includes one hole from each plate. The four corner holes in the rear plate contribute $1/4$ of a hole each. The gap width between the plates is g, and the plates are t_i thick; $i = 1$ for front plate and $i = 2$ for rear plate. The calculation of impedance is trivial for all parts of the system, except the impedance of the gap between the plates; The impedance Z_{air} of the air layer between the rear plate and the wall is given by Eq. (3.5). The specific impedance of the perforation in plate i is given by Eq. (2.36). With the addition of the classic inductive end correction (Eq. (2.12)) and half the resistive end correction (Eq. (2.32)), the impedance can be written

$$Z_{\text{p},i} = \frac{\mathrm{j}\omega\rho_0 l_i}{\pi r_i^2}\left[\left(1 - \frac{2}{x_i\sqrt{-\mathrm{j}}}\frac{J_1\left(x_i\sqrt{-\mathrm{j}}\right)}{J_0\left(x_i\sqrt{-\mathrm{j}}\right)}\right)^{-1} + \frac{8r_i}{3\pi l_i} - \mathrm{j}\frac{d_{\text{v}}}{l_i}\right], \tag{4.1}$$

where r_i is the radius of the perforations in plate i. The length of the perforations, l_i, equals the plate thickness t_i. The perforate constant x_i is given by Eq. (2.37) with $r = r_i$. Note that Eq. (4.1) does not include the end corrections for the perforation apertures facing the gap between the plates. These end corrections are not needed, because the calculation of the impedance between the plates includes the impedance associated with these apertures.

To calculate the impedance of the gap between the plates, the velocity field between the plates is required. For $g < r_i$, the field is approximately equivalent to the field set up by

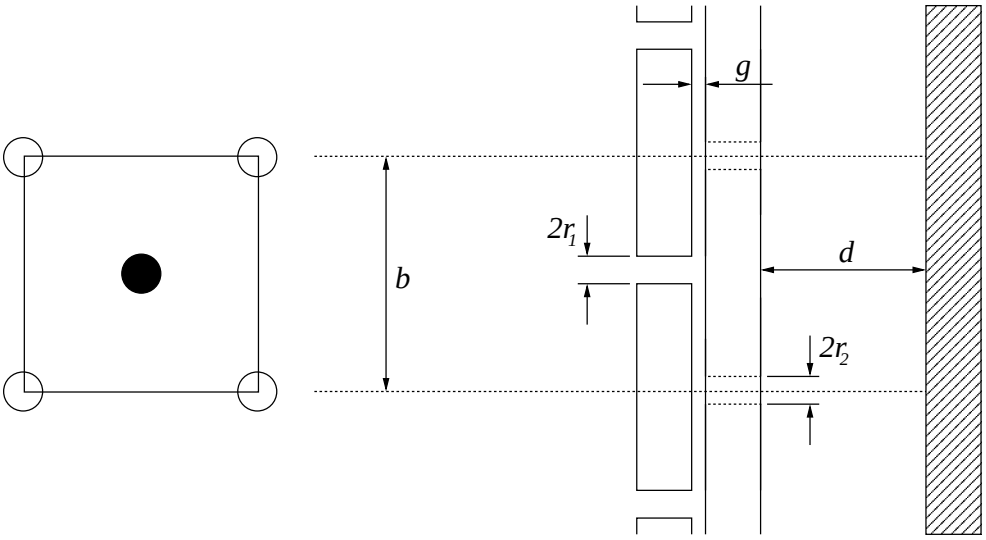

i) Front ii) Side

Figure 4.2: *Geometry of perforated double panel model.* **i)** *Only the cross-section $A = b^2$ inside the square is included in the model. A unit volume flow is assumed to flow from one hole in the front plate (filled circle) to $4 \times 1/4 =$ one hole in the rear plate.* **ii)** *The double panel is assumed to be placed a distance d in front of a hard back wall. The distance g between the plates is small enough to let viscous losses become significant.*

cylindrical radiating sources at the positions of the perforations. The sources have radii equal to the perforations radii r_i. Volume flow of unit size is assumed to flow parallel to the plates from the source associated with the front plate and into the rear plate source (*i. e.* sink). A 32×32 grid of points is defined across the imaginary tube cross-section. Each grid point has an associated area $\Delta S = (b/32)^2$. For each grid point, the velocity fields associated with each source is superposed. The grid points *inside* the perforations are of course excluded from the calculation. When the velocity field is calculated, the inductance of the gap is

$$L_{\mathrm{g}} = \frac{2}{U^2}\mathrm{KE} = \frac{2}{U^2}\left(\frac{1}{2}\rho_0 \sum_{l=1}^{32}\sum_{m=1}^{32} \left|\mathbf{u}_{l,m}\right|^2 \Delta S g\right), \tag{4.2}$$

where KE is the kinetic energy of the air in the gap. Unit volume flow, $U = 1$, is assumed. The reactance of the gap is calculated by

$$C_{\mathrm{g}} = \frac{2}{p^2}\mathrm{PE} = \frac{Ag}{\rho_0 c_0^2}, \tag{4.3}$$

where PE is the potential energy of the air in the gap. The viscous resistance of the air in the

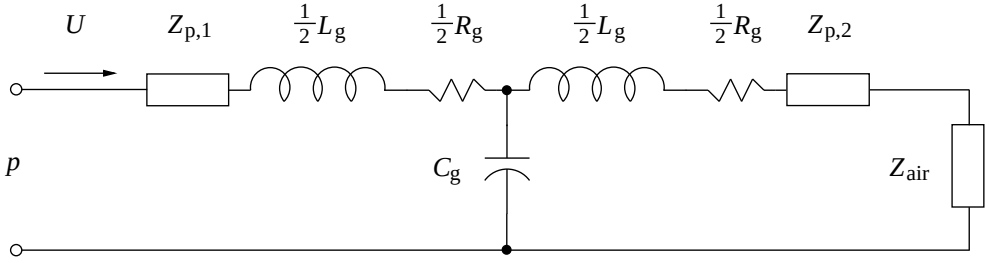

Figure 4.3: *Equivalent circuit for the perforated double panel model. The impedance $Z_{p,i}$ of a perforation in plate i includes the resistance and inductance of the perforation, and also the end corrections of the perforation apertures not facing the gap. The inductance and resistance in the gap is divided in two. The two parts are associated with the perforation apertures which faces the gap.*

gap is calculated by (see Eq. (2.29))

$$R_g = \frac{2P}{U^2} = \frac{\rho_0 \omega d_v \Delta S}{U^2} \sum_{l=1}^{32} \sum_{m=1}^{32} \left| \mathbf{u}_{l,m} \right|^2, \tag{4.4}$$

where P is the energy per second dissipated by viscous losses. Equations (4.2) to (4.4) are based on Eqs. (9.1.10), (9.1.11) and (6.4.39) in the book by *Morse and Ingard* [1968]. Equations (4.2) and (4.3) are valid only when the wavelength is much greater than the dimension of the imaginary tube, b. This is satisfied for the frequencies and geometries used here. The velocity $\mathbf{u}_{l,m}$ in Eq. (4.4) is, according to Morse & Ingard, the velocity *just outside the boundary layer*. For geometries where the plate separation g is in the order of the boundary layer thickness, R_g must be considered to be a crude approximation only. Expressions for the thermal resistances, assuming constant pressures over the surfaces, were included in a preliminary model. As stated by *Ingard* [1953], the thermal resistances were found to be negligible. To simplify the calculations, these resistances are excluded from the current model.

Figure 4.3 shows the equivalent circuit for the double panel absorber. With C_g in parallel to the impedance of the rear perforation and the air layer behind the plates, the total acoustic impedance of the imaginary tube is calculated as follows:

$$Z_{rear} = \frac{1}{2}\left(R_g + j\omega L_g\right) + Z_{p,1} + Z_{air} \tag{4.5}$$

$$Z_{gap} = \frac{Z_{rear} Z_C}{Z_{rear} + Z_C}, \text{ with } Z_C = \frac{1}{j\omega C_g} \tag{4.6}$$

$$Z_{dp} = Z_{gap} + \frac{1}{2}\left(R_g + j\omega L_g\right) + Z_{p,2} \tag{4.7}$$

Finally, the absorption coefficient is calculated by

$$\alpha = 1 - \left| \frac{Z_{dp} A - z_a}{Z_{dp} A + z_a} \right|^2 \tag{4.8}$$

Table 4.1: *Perforation radii and grid types for the plates used for measurements. Two types of grid were used; "X", where the center of the plate was perforated, and "O", where the center of the plate was not perforated. The distance between perforations was* $b = 17\,\text{mm}$*, and the plates were* $t_i = 2\,\text{mm}$ *thick.*

Plate	Perforation radius [mm]	Grid type
A	1	O
B	0.75	X
C	0.75	O
D	0.5	X
E	0.5	O
F	0.25	X

4.1.2 Measurements and simulations

Dimensions of samples

For the experiments, six different circular aluminium plates were used. By combining two and two plates, different configurations of double panel absorbers were obtained. All the plates were $t_i = 2\,\text{mm}$ thick and had a diameter of 103 mm. The plates had perforations with circular cross-section. Two types of regular grids, with $b = 17\,\text{mm}$ between the holes, were used. Table 4.1 shows the dimensions of the plates used. To keep the plates separated during measurements, several thin rings were cut out of copper sheets 0.11 and 0.30 mm thick. These rings had inner diameter 97 mm and outer diameter 103 mm. It was assumed that these rings did not significantly obstruct the flow of air through the double panel absorber.

Impedance measurements in Kundt's tube

The impedance of the panels were measured in a standard Kundt's tube, shown in Fig. 4.4. The diameter of the tube is 100 mm and the sample holder diameter is 103 mm. Two plates with different grid types were mounted in the tube so that the perforations in the front and rear plate were at maximum distance from each other. See Figs. 4.1 and 4.2. The standardized transfer-function method [*Chung and Blaser*, 1980; *ISO 10534-2*, 1996] was used to measure the impedance of the absorber. The setup was basically the same as in Fig. 3.8, except that the loudspeaker was not driven by a MLS-signal, but a white noise signal. The impedance was calculated by Eq. (3.27) after the transfer function H_{12} between the microphones had been measured. The microphones were *Brüel & Kjær* condenser microphones, type 4165. The transfer function was measured with a *ONO SOKKI* dual channel FFT-analyzer, type CF-940. The distance between the microphones was $s = 80\,\text{mm}$. The distance between the front microphone and the sample was $t = 180\,\text{mm}$. The lowest cut-off frequency of the tube is approximately 2 kHz [*Morse and Ingard*, 1968, Ch. 9.2]. For the microphone separation used here, the article by *Boden and Åbom* [1986] suggests that the best accuracy is obtained in the frequency range 212 – 1700 Hz.

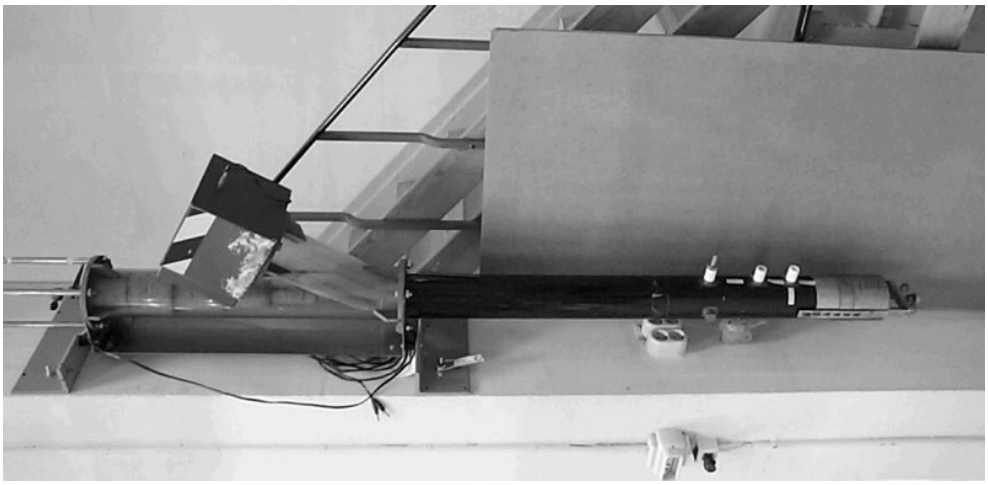

Figure 4.4: *The circular Kundt's tube used for the impedance measurements. Note that the figure has been rotated counterclockwise. The samples and the reflecting end piece are mounted from below and are held in place by the "clamp" at the bottom. There is no visual control of the mounted samples.*

Three series of experiments were done. Tables 4.2 and 4.3 show the geometries of the configurations in the first and third measurement series. After measurement 119, a small, possible leakage in the reflecting end piece was sealed. The second series of experiments (measurements 016 – 018) was done with single plates only. This was done to observe the absorption of the perforations, without the effect of the lateral slit between the plates. The tree plates used were plates F, D and A in Table 4.1, with perforation diameters 0.5, 1.0 and 2.0, respectively. The measuring frequency ranges were 0 – 500 Hz for measurements 001 – 018, and 50 – 1050 Hz for measurements 101 – 123.

Simulations

The panel dimensions listed in Tables 4.2 and 4.3 were also used in the simulations by the model presented in Sec. 4.1.1. The simulations were done at $1/6$ octave spaced points in the frequency range 39.7 – 2016 Hz. Because the predictions of the model agreed poorly with the measurements (see Sec. 4.1.3), simulations were not carried out for other geometries. The absorption coefficient of the single panel absorbers were simulated by the computer program *FLAG*, described on page 39. *FLAG* has two models for perforated panels; the MPP model described earlier, and a simpler model which is based on the mass of the air in the perforations, the classic mass end correction, and Ingard's expression for the resistance in and around the perforations (Eqs. (2.6), (2.12) and (2.31), respectively). The latter model failed completely in predicting the resistance of the small perforations in plate F. Therefore, the *FLAG* MPP model used in Sec. 3.2.3 is also used here.

Table 4.2: *Dimensions of the measured and simulated perforated double panels, first series. See Fig. 4.2 for definition of symbols. For all geometries,* $d = 95.5\,\text{mm}$.

Measurement no.	r_1 mm	r_2 mm	g mm
001		(Calibration)	
002	1	0.75	0.3
003	1	0.25	0.3
004	0.25	1	0.3
005	0.75	0.5	0.11
006	0.75	0.5	0.3
007	0.75	0.5	0.6
008	1	0.5	0.6
009	0.25	0.75	0.6
010	0.75	0.75	0.11
011	0.75	0.75	0.22
012	0.75	0.75	0.3
013	0.75	0.75	0.6
014	0.75	0.75	0.9
015	0.75	0.75	1.2

Table 4.3: *Dimensions of the measured and simulated perforated double panels, third series. See Fig. 4.2 for definition of symbols. For these configurations,* $d = 29.1\,\text{mm}$.

Measurement no.	r_1 mm	r_2 mm	g mm
101		(Calibration)	
119	0.75	0.75	0.6
120	0.75	0.75	0.6
121	0.75	0.75	1.2
122	1	0.75	1.2
123	1	0.5	1.2

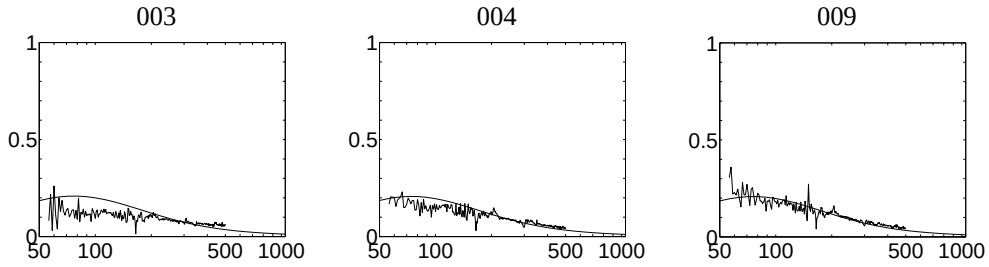

Figure 4.5: *Measured and simulated absorption coefficient of perforated double panels as function of frequency. Perforation radius* $r = 0.25\,\text{mm}$ *for one plate. See Table 4.2 for geometry definitions.*

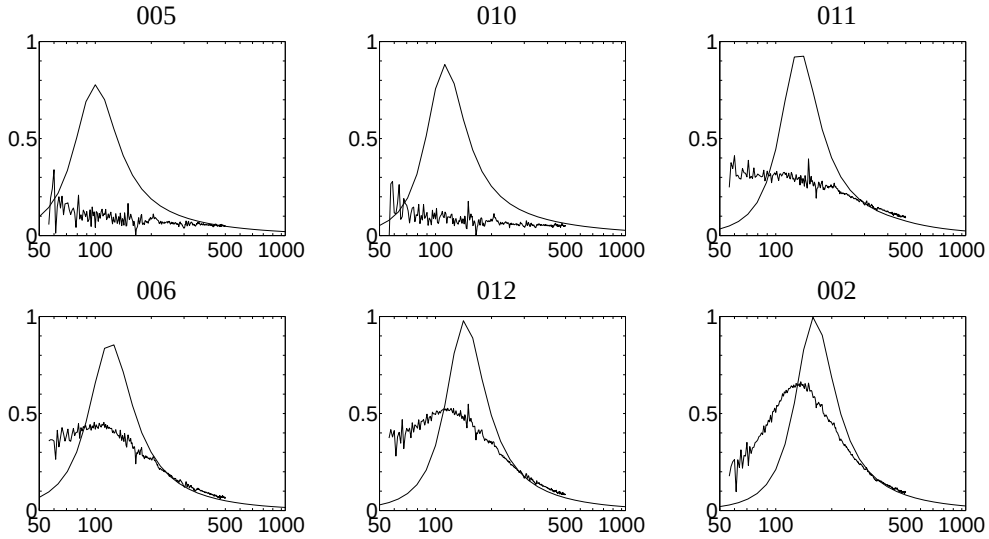

Figure 4.6: *Measured and simulated absorption coefficient of perforated double panels as function of frequency. Perforation radius* $r_i \geq 0.5\,\text{mm}$ *for both plates, and gap width* $g \leq 0.3\,\text{mm}$*. See Table 4.2 for geometry definitions.*

4.1.3 Results

The experimental work indicated that the plate separation influenced the absorption characteristics quite strongly, as was expected. Figures 4.5 to 4.8 compare the absorption coefficient predicted by the analytical model to the measured absorption coefficient. For comparison, Fig. 4.9 shows the measured absorption coefficient of perforated single panels. The results have two implications:

- The model described in Sec. 4.1.1, although approximately adequate for some of the geometries, is clearly not able to give accurate predictions of the absorption coefficient.
- The geometries of Tables 4.2 and 4.3 are clearly not suited as broadband absorbers.

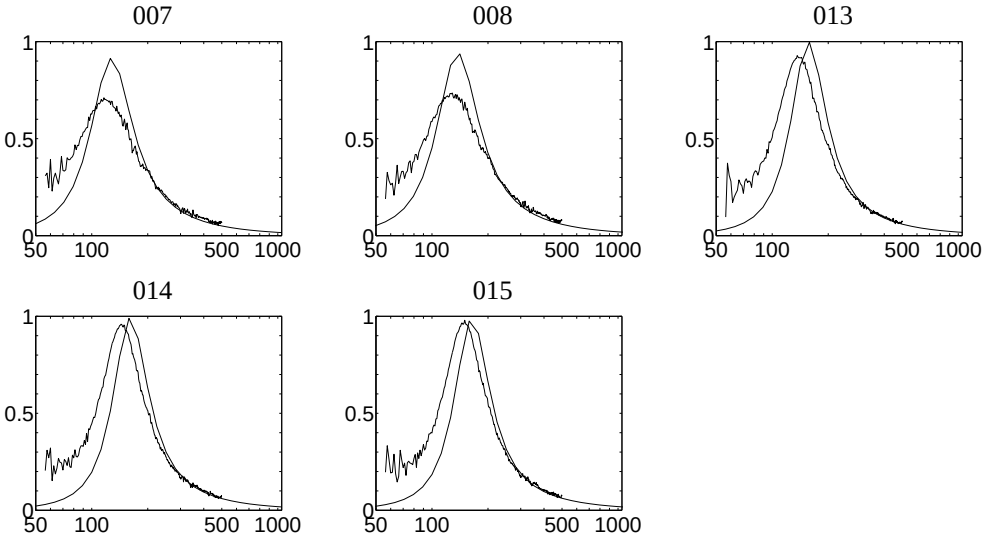

Figure 4.7: *Measured and simulated absorption coefficient of perforated double panels as function of frequency. Perforation radius* $r_i \geq 0.5\,\text{mm}$ *for both plates, and gap width* $g \geq 0.6\,\text{mm}$. *See Table 4.2 for geometry definitions.*

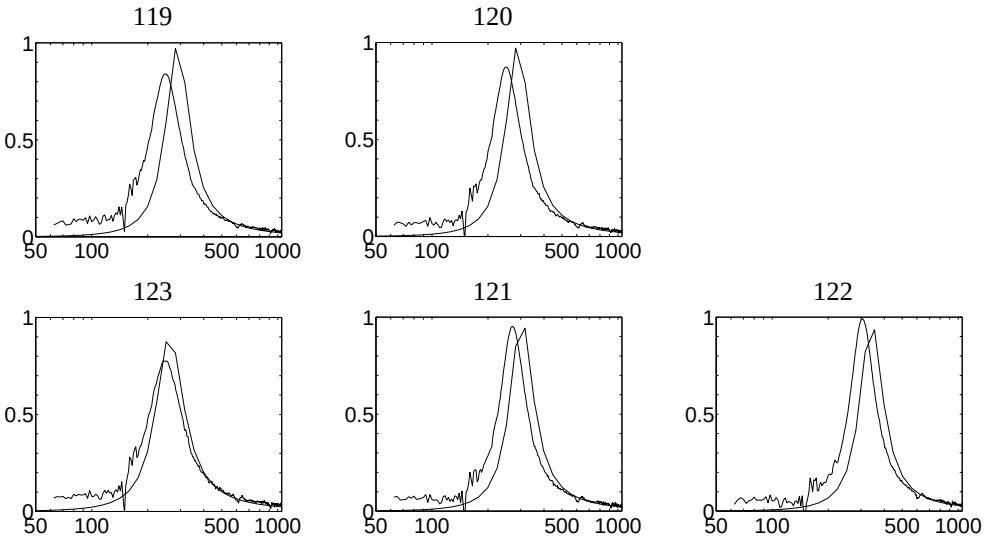

Figure 4.8: *Measured and simulated absorption coefficient of perforated double panels as function of frequency. Perforation radius* $r_i \geq 0.5\,\text{mm}$ *for both plates, and gap width* $g \leq 0.3\,\text{mm}$. *See Table 4.3 for geometry definitions.*

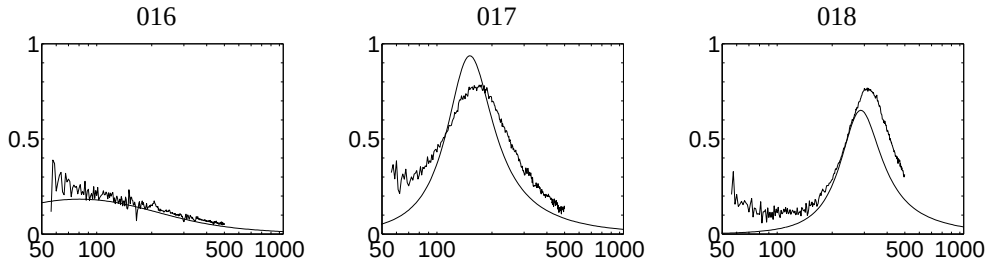

Figure 4.9: *Measured and simulated absorption coefficient of perforated single panels as function of frequency. See page 54 for geometry definitions.*

The model handles the geometries 003, 004 and 009 very well (see Fig. 4.5). In these geometries, the holes in the front or rear plate are quite small, $r = 0.25\,\text{mm}$, and the gap width is not very small, $g \geq 0.3\,\text{mm}$. The agreement between the model and the measurements is due to the fact that in these cases the impedance of the small perforation, Eq. (4.1), is of greater importance than the impedance of the gap (see geometry 016 in Fig. 4.9). For the geometries with larger perforations, $r \geq 0.5\,\text{mm}$, the agreement between model and measurements is clearly dependent on the value of g. For large values of g (geometries 115 and 121 – 123), the agreement is quite good, although a little shifted in frequency. For small g (geometries 005, 010 and 011), the model fails completely. The critical part of the model is Eq. (4.4), the resistance of the gap. As mentioned in Sec. 4.1.1, this equation is not valid, and clearly underestimate the resistance, when the distance between the plates is comparable to (or smaller than) the viscous boundary layer thickness.

The geometries tested are clearly not optimal. The main part of the energy dissipation is supposed to take place in the gap between the plates. Therefore, analogous to the MPPs, the gap width between plates should be in the order of the viscous boundary layer thickness. However, for the geometries where this is the case, it seems that the distance between perforations b is too large. In these cases, the relative resistance is significantly greater than unity. For the geometries with larger g, the resistance of the gap is low, and the total relative resistance is less than unity. To achieve a reasonable broadband absorption, optimum combinations of b and g, and to a lesser extent, r_i, must be found.

The accuracy of the measurements, especially 002 – 018, was poor for low frequencies. This is probably due to the small microphone separation. Because of this, the measurement data were cut at 56 Hz in all the figures above.

4.2 Slit-shaped perforations with constant separation

The initial investigation of the perforated double panel absorber was unsatisfactory. A better model was required to predict the impedance of the gap between the plates, and more experiments were required to validate the model. To simplify the geometry of the slit between the plates, the perforations were now assumed slit-shaped. With this change in geometry, the flow in the narrow gap between the plates becomes almost unidirectional. The impedance of flow in a thin, infinitely long gap is given by Eq. (2.38). However, the effect of the sharp

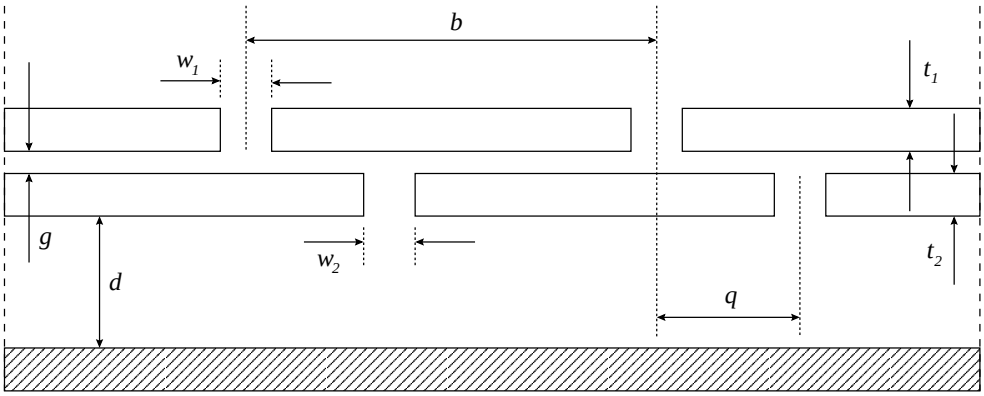

Figure 4.10: *The geometry of the slitted double panel resonator concept (side view, not at scale). The center-center distance between slits, b, is the same for the two plates. The offset between the centers of the slits in the two plates is q. The gap width g is in the order of one or two viscous boundary layers to allow viscous effects to become significant*

edges of the perforations is not easily incorporated in a theoretical model. Therefore, the Finite Difference Method was used to simulate the impedance of the gap between the plates. The model presented below is a revised version of an initial version which did not allow lateral displacement of one plate relative to the other. The initial model and some of the initial measurements have been described earlier [*Randeberg et al.*, 1999; *Randeberg*, 2000]. Besides the possibility of lateral displacement and some minor changes, the initial and revised versions are practically equivalent. Therefore, only the latter is presented below.

4.2.1 Model

The geometry of the slitted double panel absorber is shown in Fig. 4.10. As in Sec. 4.1.1, the model considers an imaginary tube. The cross-section area of the tube, and hence the cross-section of the cavity volume associated with a set of slits, is $A = b \times 1$. The impedance Z_{air} of the cavity behind the double panel is given by Eq. (3.5), with b^2 substituted by A:

$$Z_{\text{air}} = -\text{j}\frac{z_{\text{a}}}{A}\cot kd = -\text{j}\frac{z_{\text{a}}}{b}\cot kd \tag{4.9}$$

The distance between the front and rear slits is q. In this section, where the distance between the slits is constant, $q = b/2$. In general, q can take values in the range $0-b$, but due to symmetry, only the range $0-b/2$ is relevant.

The specific impedance of a slit in plate $i = 1$ or 2 is given by Eq. (2.38), the *total* inductive end correction of the slit is given by Eq. (2.22), and the *total* resistive end correction is given by Eq. (2.33). As explained below, the full length $l_i = t_i$ is not used in the first of these equations, but rather a length $l_i^{'} < l_i$. Using only the inductive and resistive end corrections

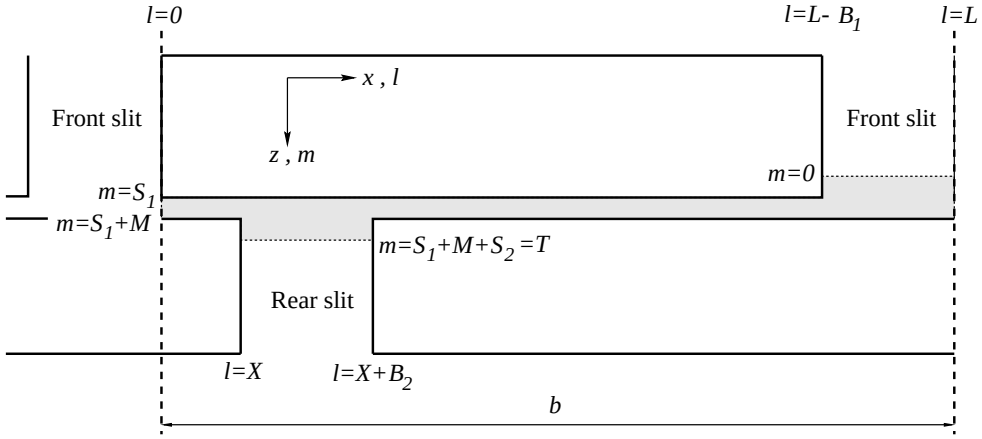

Figure 4.11: *The geometry of the FDM model for a slitted double panel resonator. The figure is at scale for a panel with typical dimensions. The FDM is used to solve Eq. (4.11) in the shaded region. The symbols are explained in the text. Note the cyclic symmetry; Points to the right of $l = L$ are equivalent to points to the right of $l = 0$.*

of the aperture which does not face the gap, the impedance of a slit in plate i can be written

$$Z_{s,i} = \frac{j\omega\rho_0 l_i'}{w_i}\left\{\left[1 - \frac{\tanh\left(x_s\sqrt{j}\right)}{x_s\sqrt{j}}\right]^{-1} - \frac{w_i}{\pi l_i'}\log\left[\sin\left(\frac{\pi w_i}{2b}\right)\right] - j\frac{d_v}{l_i'}\right\}, \tag{4.10}$$

where x_s is given by Eq. (2.39) with $w = w_i$, and d_v is given by Eq. (2.25).

As mentioned above, the impedance of the gap between the plates is calculated by the FDM. Assuming Cartesian coordinates, the linear Navier-Stokes equation, Eq. (2.34), and the mass conservation equation, Eq. (3.9) with $\phi = 1$, are written as

$$\begin{aligned} j\omega\rho_0 u + \frac{\partial p}{\partial x} - \mu\left(\frac{\partial^2 u}{\partial x^2} + \frac{\partial^2 u}{\partial z^2}\right) &= 0 \\ j\omega\rho_0 v + \frac{\partial p}{\partial z} - \mu\left(\frac{\partial^2 v}{\partial x^2} + \frac{\partial^2 v}{\partial z^2}\right) &= 0 \\ j\omega p + \rho_0 c_0^2\left(\frac{\partial u}{\partial x} + \frac{\partial v}{\partial z}\right) &= 0, \end{aligned} \tag{4.11}$$

These equations are solved for pressure $p(x,z)$ and velocity $\mathbf{u}(x,z) = u(x,z)\,\hat{\mathbf{x}} + v(x,z)\,\hat{\mathbf{z}}$ in the region shown shaded in Fig. 4.11. The gap between the plates is divided into M vertical steps of length $\Delta z = g/M$. The imaginary tube is divided into L horizontal steps of length $\Delta x = b/L$. L is determined so there are at least L_1 grid points in the most narrow slit, and at least L_2 grid points in the tube. It is desirable to include the edge effects of the slits in the FDM simulations. Therefore, the simulated region extends a length $\Delta z S_i$ into the slit in plate

i. $\Delta z S_i$ is set equal to g or $t_i/2$, whichever is smaller:

$$S_i = \begin{cases} M & \text{if} \quad g < \frac{t_i}{2} \\ M\frac{t_i}{2g} & \text{if} \quad g \geq \frac{t_i}{2} \end{cases} \tag{4.12}$$

Consequently, the reduced length in Eq. (4.10) is given by

$$l_i^{'} = l_i - \Delta z S_i \tag{4.13}$$

The values of M, L_1 and L_2 are given as input parameters to the simulation. The values of W_i and X in Fig. 4.11 are determined by the real slit widths w_i, so that w_i are *equal to* or *larger* than the width of the simulated slits, $\Delta x W_i$. X is also chosen so that $X + W_1/2 + W_2/2$ is the closest integer to $q/\Delta x$. In those cases where a simulated slit is wider than the corresponding real slit, *i. e.* if grid points at $l = L - W_1$, X or $X + W_2$ are not exactly at the real slit surfaces, those points are treated specially, as described below.

The boundary conditions used in the simulations are

– Repeating symmetry, *i. e.* points at $l = 0$ are the same as $l = L$:

$$\begin{aligned} u_{0,m} &= u_{L,m} & u_{-1,m} &= v_{L-1,m} \\ u_{1,m} &= u_{L+1,m} \end{aligned} \tag{4.14}$$

The same equations are valid with v or p instead of u. Any point at $l = L + n$ is equivalent to $l = n$.

– Constant sound pressure p^0 and vertical flow in the front slit ($m < 0$):

$$\begin{aligned} p_{l,-1} &= p^0 & v_{l,-1} &= v_{l,0} \\ u_{l,-1} &= 0 \end{aligned} \tag{4.15}$$

Equations (4.11) are linear, thus the impedance at any point is independent of p^0. The value of p^0 is therefore arbitrary, and is set to $p^0 = 1\,\text{Pa}$.

– Constant specific impedance z_T at the boundary in the rear slit ($m = T$), and vertical flow in the rear slit ($m > T$):

$$\begin{aligned} p_{l,T} &= z_T v_{l,T} & v_{l,T+1} &= v_{l,T} \\ u_{l,T+1} &= 0 & p_{l,T+1} &= p_{l,T} \end{aligned} \tag{4.16}$$

Here, $z_T = w_2 \left(Z_{\text{air}} + Z_{\text{s},2} \right)$.

– All surfaces are hard, and there is no slip of the viscous flow:

$$\left. \frac{\partial p}{\partial n} \right|_{\text{surface}} = 0 \qquad \mathbf{u}|_{\text{surface}} = 0, \tag{4.17}$$

where $\partial p/\partial n$ is the derivative of the pressure in the direction of a vector **n** normal to any surface. One exception was made to the "no slip" condition, as the velocity was allowed to be non-zero at the corners of the slits.

The symmetry makes it easy to handle situations where $l = L$ (*i. e.* $l = 0$) is *inside* the rear slit: In such cases, points outside the interval $l = 1 - L$ are wrapped inside. Analogous to the method used in Sec. 3.1.3, points more close to the surface than a normal horizontal grid length Δx are treated specially. The number η_m is defined as the ratio of the point – surface distance to the grid length, for grid line m. The pressure at the special points, *e. g.* at $l = X$, is calculated by [*Crandall*, 1956]

$$p_{l,m} = p_{l+1,m}, \tag{4.18}$$

and the particle velocity is calculated by

$$\mathbf{u}_{X,m} = \frac{\eta_m}{1+\eta_m}\mathbf{u}_{X+1,m} \tag{4.19}$$

Analogous equations are used for the other surfaces, $l = L - W_1$ and $l = X + W_2$.

The output of the FDM is the pressure and velocity distribution in the gap between the plates and inner parts of the slits. The average acoustic impedance at the entry of the front slit is given by the specific impedance at $m = 0$ and the acoustic impedance of the front slit, including end corrections (Eq. (4.10)):

$$Z_{\mathrm{dp}} = \frac{1}{w_1\,(B1+1)} \sum_{l=L-B1}^{L} \frac{p_{l,0}}{v_{l,0}} + Z_{\mathrm{s},1} \tag{4.20}$$

The absorption coefficient of the slitted panel absorber is given by Eq. (4.8), with $A = b \times 1$.

As with the FDM model used to simulate the microhorns in Sec. 3.1.3, the accuracy of the model presented here is limited by the available computing resources. As the gap between the plates is the most important parameter in determining the characteristics of the double panel absorber, the number M of vertical steps cannot be too small. However, the slits are typically ten times wider than g, thus it is not feasible to require that $\Delta x \approx \Delta z$. The number of x-steps in the inner parts of the slits may therefore not be optimal. Additionally, the boundary conditions at the boundary between the FDM model and the analytical expressions in the slits may induce some errors. A constant, average specific impedance is used in both slits. The errors introduced by these assumptions are probably much less than the error that would be caused by not including the inner parts of the slits (and hence the velocity field near the corners) in the FDM model.

4.2.2 Measurements and simulations

Dimensions of samples

For the experiments, 12 different aluminium plates were used. The plates were combined in pairs to form a number of double panel configurations. The diameter of the plates was 103 mm. The plates had regularly spaced, slit-shaped perforations. Table 4.4 shows the

Table 4.4: *Slit width w, slit separation b, plate thickness t and slit configuration for plates used for measurements. Two kinds of slit configurations were used; "X", where the diagonal of the plate was slitted, and "O", where the diagonal of the plate was not slitted.*

Plate	w mm	t mm	b mm	Slit configuration
A	1	1	15	O
B	1.5	1	15	O
C	1.5	2	15	O
D	1.5	2	15	X
E	3	2	15	O
F	3	2	15	X
G	2	3	15	X
H	3	3	15	X
I	1	1	20	X
J	1.5	2	20	X
K	1.5	2	20	O
L	2	3	20	O

dimensions of the plates used for measurements. The same type of thin, annular copper rings as described in Sec. 4.1.2 were used to keep the plates separated during measurements. The dimensions of the rings were the same as before, *i. e.* 0.11 and 0.3 mm thick.

Impedance measurements in Kundt's tube

The impedance of the panels were measured in the same standard Kundt's tube that was used to measure the perforated double panels. See Fig. 4.4. Two plates with different slit configurations (centered and non-centered) were mounted in the tube so that the slits of the front and rear plates were parallel to each other. Thus, the value of q in Fig. 4.10 was $b/2$ for these measurements. One or more of the annular rings were placed between the plates to keep them separated at a given distance g. The measurement method and setup was almost identical to what was used in Sec. 4.1.2. However, the distance between the microphones was now $s = 200$ mm, and the distance between the front microphone and the sample was $t = 300$ mm. For this microphone separation, the best accuracy is obtained in the frequency range 85 – 680 Hz [*Boden and Åbom*, 1986]. The distance d to the hard back wall was 95.5 mm.

Two series of experiments were conducted, the frequency range of which were 50 – 550 Hz and 100 – 600 Hz, respectively. To test the sensitivity to plate concavity, all the second series measurements were repeated with the front plate turned back to front. Three gap widths g were tested; 0.11, 0.22 and 0.52 mm, using an appropriate combination of the copper rings. Tables 4.5 and 4.6 summarizes the dimensions of the measured double panels.

Table 4.5: *Dimensions of the measured slitted double panels, first series. See Fig. 4.10 for definition of symbols. For all geometries,* $b = 15\,\mathrm{mm}$ *and* $q = 7.5\,\mathrm{mm}$.

Measurement no.	g mm	t_1 mm	t_2 mm	w_1 mm	w_2 mm
000			(Calibration)		
001	0.52	1.0	2.0	1.0	1.5
002	0.22	1.0	2.0	1.0	1.5
003	0.11	1.0	2.0	1.0	1.5
004	0.11	1.0	2.0	1.5	1.5
005	0.11	2.0	3.0	3.0	3.0
006	0.22	2.0	3.0	3.0	3.0
007	0.11	2.0	3.0	3.0	2.0
008	0.22	2.0	3.0	3.0	2.0
009	0.11	1.0	3.0	1.5	3.0
010	0.22	1.0	3.0	1.5	3.0
011	0.11	1.0	3.0	1.0	2.0
012	0.22	1.0	3.0	1.0	2.0

Table 4.6: *Dimensions of the measured slitted double panels, second series. See Fig. 4.10 for definition of symbols. Measurements 101 – 104 had* $b = 15\,\mathrm{mm}$ *and* $q = 7.5\,\mathrm{mm}$. *Measurements 105 – 107 had* $b = 20\,\mathrm{mm}$ *and* $q = 10\,\mathrm{mm}$.

Measurement no.	g mm	t_1 mm	t_2 mm	w_1 mm	w_2 mm
100			(Calibration)		
101	0.11	2.0	3.0	3.0	3.0
102	0.22	2.0	3.0	3.0	3.0
103	0.11	2.0	3.0	1.5	3.0
104	0.22	2.0	3.0	1.5	3.0
105	0.22	1.0	3.0	1.0	2.0
106	0.11	2.0	2.0	1.5	1.5
107	0.22	3.0	2.0	2.0	1.5

Table 4.7: *Simulation parameters used in the FDM model of the slitted double panels. See page 60 for definition of symbols.*

M	10	Number of z-steps in gap between plates
L_1	10	Minimum number of x-steps in the most narrow slit
L_2	50	Minimum number of x-steps in the gap between the plates

Simulations

Because the gap width is a very critical parameter, several values of g were used in the simulations while the other parameters from Tables 4.5 and 4.6 were kept constant. The values that were used are not tabulated here, but are given together with the results in Sec. 4.2.3. The simulation parameters used are shown in Table 4.7. These values were found to give a good compromise between simulation time and accuracy. The simulations were done at $1/3$ octave spaced points in the frequency range $39.7 - 2016$ Hz.

To compare the double panel resonator with the MPPs, the absorption of two MPPs were calculated using the FLAG program (see page 39). For the FLAG calculations, the perforation separations were chosen to give approximately the same resonance frequency as the resonance frequencies of the double panel with which the MPPs are compared. MPP A had a 0.65% perforation, and MPP B had a 0.39% perforation. The panel thickness was 1 mm, and the perforation radius was 0.5 mm. The same back cavity thickness as used during measurements, $d = 95.5$ mm, was assumed. The simulations were done at $1/30$ octave spaced points in the frequency range $35 - 1094$ Hz.

4.2.3 Results

Both the experiments and the simulations shown in Figs. 4.12 to 4.14 show that the absorption characteristics are very dependent on the gap width g between the plates. The most important observation that can be drawn from these figures is that an *optimum* value of g exists, for which the panel absorber has a high absorption and a relatively large bandwidth. The bandwidth of the resonance increases when g decreases, while the absorption at resonance, α_0, has a maximum value for some value of g. The situation is analogous to the case with MPPs, discussed by *Maa* [1987, 1998] (see Sec. 2.4.1). If the gap g between the plates is considered analogous to the perforation diameter r, the following observations can be made. For a small value of g, the relative resistance θ is high, because θ increases proportionally to $1/g^4$ (see Eq. (2.50)). Thus, a decrease in g increases the bandwidth, as illustrated by Fig. 2.9. On the other hand, the maximum absorption coefficient of Eq. (2.52), with $\theta \approx Y/g^4$, is

$$\alpha_0 \approx \frac{4Y}{\left(g^2 + \frac{Y}{g^2}\right)^2}, \tag{4.21}$$

where Y is a constant. Thus, α_0 has a maximum for $g \approx \sqrt[4]{Y}$. The simulation results confirm these effects. The maximum resonance absorption seems to occur at a gap width a little higher

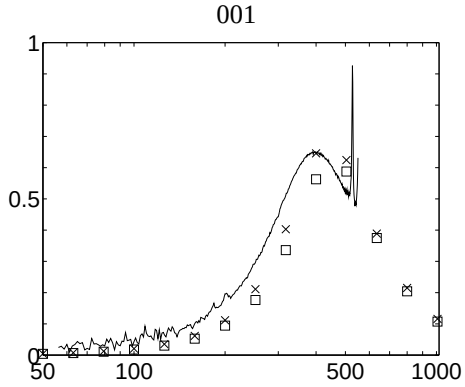

Figure 4.12: *Measurements and simulations of slitted double panels. Absorption coefficient as function of frequency for different gap widths g. See Table 4.5 for geometry definition. Measured gap width was* $g = 0.52\,\text{mm}$*. Simulated gap widths:* $\times$*,* $g = 0.52\,\text{mm}$*;* $\square$*,* $g = 0.58\,\text{mm}$*. The sharp peaks at about* 500 Hz *are due to plate resonances.*

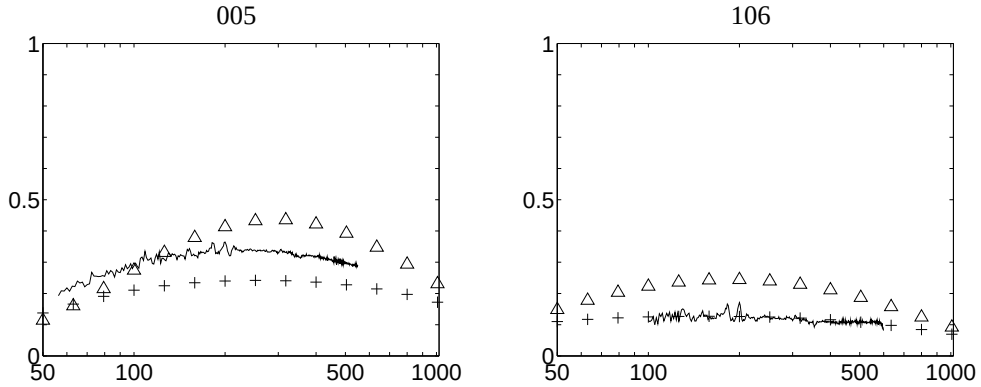

Figure 4.13: *Measurements and simulations of slitted double panels. Absorption coefficient as function of frequency for different gap widths g. See Tables 4.5 and 4.6 for geometry definitions. Measured gap widths were* $g = 0.11\,\text{mm}$*. Simulated gap widths:* $+$*,* $g = 0.11\,\text{mm}$*;* $\triangle$*,* $g = 0.14\,\text{mm}$*.*

than 0.22 mm. Also note that some of the double panel measurements show sharp peaks at about 500 Hz. These peaks are due to plate resonances in the relatively thin plates (1 mm) used in some of these double panels. As this resonance is narrow, and also not close to the Helmholtz resonance, it should not invalidate the measurements.

The simulations by the FDM model described in Sec. 4.2.1 correspond reasonable well with the measurements. The discrepancy in the maximum absorption is in some cases mainly caused by inaccuracy in the value of g. The plates are never completely plane, and may be slightly concave or convex. As showed by the simulations, a small deviation in g can significantly alter the value of α_0. The sensitivity to variations in g, and thus the influence of plate

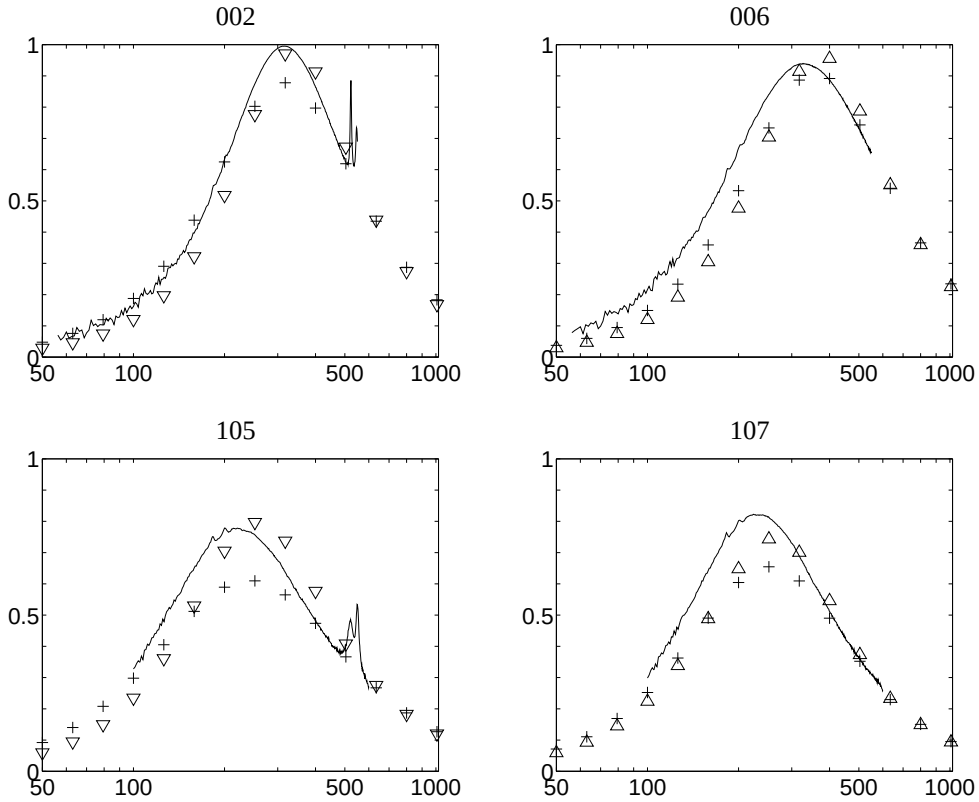

Figure 4.14: *Measurements and simulations of slitted double panels. Absorption coefficient as function of frequency for different gap widths g. See Tables 4.5 and 4.6 for geometry definitions. Measured gap widths were* $g = 0.22\,\text{mm}$*. Simulated gap widths:* $+$*,* $g = 0.22\,\text{mm}$*;* $\triangle$*,* $g = 0.24\,\text{mm}$*;* $\bigtriangledown$*,* $g = 0.26\,\text{mm}$*. The sharp peaks at about* 500 Hz *are due to plate resonances.*

concavity appear to be less for the large plate separation $g = 0.52\,\text{mm}$. The gap width also influences the resonance frequency. Figure 4.15 shows all measurements, except measurement 001 where $g = 0.52\,\text{mm}$. The results, especially those for $b = 15\,\text{mm}$, show that the measured resonance frequencies divide into two groups. This grouping is mainly determined by the gap width. Within each group of curves, the ratio of maximum and minimum air volume in the slits and in the gap up to 3:1. This variation in air volume (*i. e.* resonator mass) influences the resonance frequency relatively little. On the other hand, for each pair of configurations where only g differs, the variation in total air volume is about 10 %, while the difference in resonance frequency is large. Consequently, the effective resonator mass is mainly determined by the effective density of the air in the gap, and only slightly dependent on the air volume in the gap and the slits. This may also be confirmed by approximating the effective mass of the slits and the gap by the imaginary part of Eq. (2.38). Table 4.8 shows the results for some typical dimensions. The results have two implications: *Firstly*, the total effective mass of the slits is much less than the effective mass of the gap between the plates. Therefore, the influence on

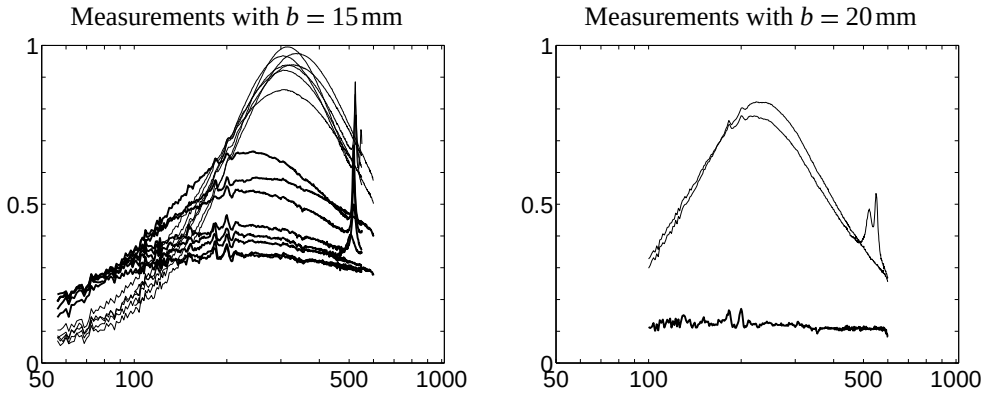

Figure 4.15: *Measurements of slitted double panels. Absorption coefficient as function of frequency for different gap widths g. All measurements in Tables 4.5 and 4.6 are shown, except for measurement 001.* ——, $g = 0.22$ mm*;* ——, $g = 0.11$ mm*.*

Table 4.8: *Effective mass for typical slit and gap widths. Calculated by imaginary part of Eq. (2.38), with* $f = 200$ Hz *and* $b = 15$ mm*.*

Length mm	Width mm	Effective mass g/m^2
$l = t = 1$	1.0	0.316
	3.0	0.097
$l = b/2 = 7.5$	0.14	17.8
	0.26	9.6

the resonance frequency is small. *Secondly*, the square root of the ratio of effective mass of the gap is 1.36. This is close to the ratio of typical resonance frequencies of the two groups of curves in Fig. 4.15, *i. e.* 310 and 230 Hz. The predicted resonance frequencies in Figs. 4.12 to 4.14 are generally a bit high compared with measurements. Like the discrepancy in α_0, this may in some cases be caused by non-planar plates, leading to a deviation in the value of g. However, because the predicted f_0 is generally too high, it seems that the effective resonator mass of the model is a little too low for most of the configurations. One reason for this may be that the FDM grid size is too large, so that the effective mass in the gap, especially near the edges of the slits, is not calculated correctly.

To investigate the effect of plate concavity, the second series of measurements was repeated with the front plate turned back to front. The effect of this is shown in Fig. 4.16. As shown, the turning of the front plate may lead to an increase or a decrease in α_0, or it may have no effect at all. The effect depends on the shape of the plates, and the sensitivity is largest for small values of g.

Figure 4.17 illustrates the effect of the slit distance b, when all other parameters (except

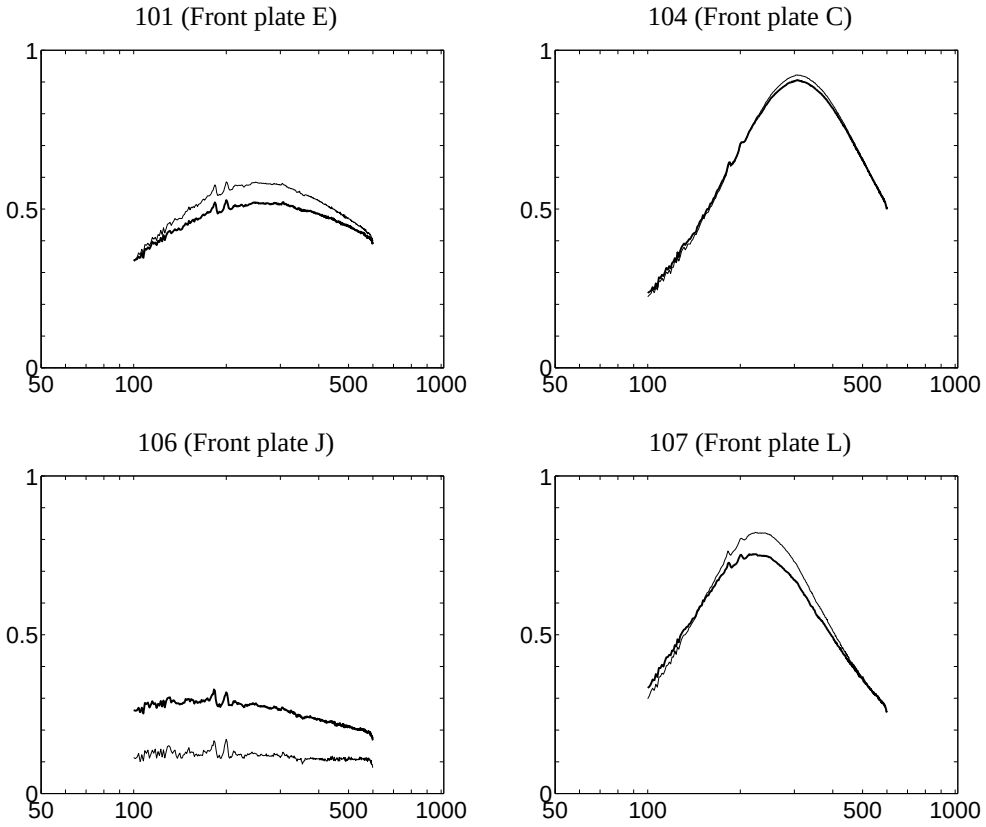

Figure 4.16: *Measurements of slitted double panels. Absorption coefficient as function of frequency with and without reversion of front plate. See Table 4.6 for geometry definitions.* ——*, front plate normal;* ——*, front plate reversed.*

q which equals $b/2$) are kept constant. Due to the higher cavity volume per slit for higher b, the shift towards lower frequencies is expected. The reduction of α_0 for $b = 20\,\text{mm}$ indicates that the resistance in this case is too large. Thus, there exists an optimum value of b for a given plate separation g.

Figure 4.18 compares the absorption of some of the double panel measurements with *FLAG* simulations of some typical MPPs. See Sec. 4.2.2 for dimensions of the MPPs. The high correspondence between the simulation of MPP A and the measurement of configuration 008 is a coincidence, but shows that the two concepts may have comparable absorption characteristics. Note that the dimensions of the measured double panels presented in this section have not been optimized.

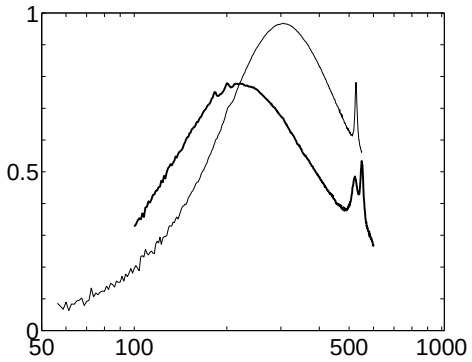

Figure 4.17: *Measurements of slitted double panels. Absorption coefficient as function of frequency for different values of b. See Tables 4.5 and 4.6 for geometry definitions.* ——, *measurement 012;* ——, *measurement 105.*

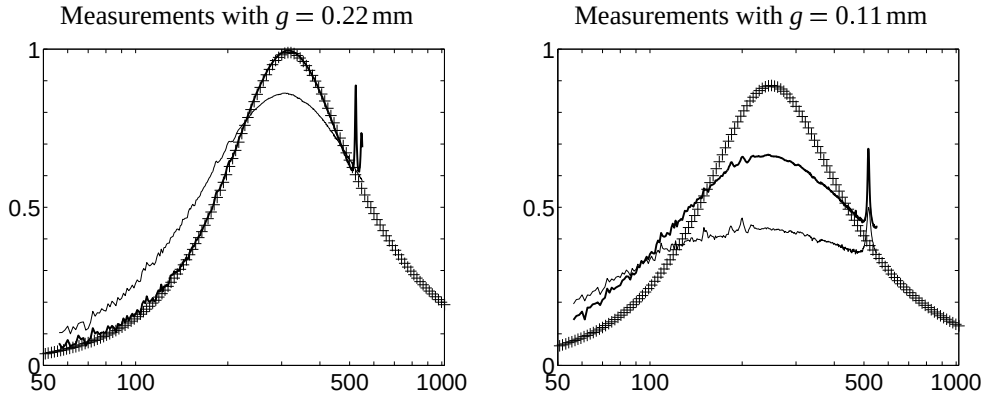

Figure 4.18: *Measurements of slitted double panels compared with simulations of MPPs. Absorption coefficient as function of frequency. See Table 4.5 and page 65 for geometry definitions. Left graph:* ——, *measurement 008;* ——, *measurement 002;* $+$, *MPP A. Right graph:* ——, *measurement 009;* ——, *measurement 003;* $+$, *MPP B.*

4.3 Slit-shaped perforations with adjustable separation

The results of the preceding section indicated that the double panel absorber could have absorption characteristics comparable to or better than those of MPPs. Further investigation was necessary. The availability of a Kundt's tube with a square cross-section made it possible to experimentally investigate the effect of relative lateral displacement of the slits in the two plates. This section presents measurements and simulations of this effect. A complete investigation of the effect of all eight geometry parameters is also presented.

4.3.1 Model

The model used in this section was presented in Sec. 4.2.1. The value of the slit separation q is in the range $0 - b/2$. The limits of this interval correspond to what will be called the "open" and "closed" states of the double panel absorber.

4.3.2 Measurements and simulations

Dimensions of samples

Four slitted double panels were produced for measurements. The dimensions of the panels are listed in Table 4.9. The panels were made of steel. To allow the plates to move relative to each other, while keeping a constant distance between the plates, thin strips of copper were glued to the front plate. The rear plate was fastened with screws to the front plate through short slits in the rear plate. Fig. 4.19 shows panel sample C in the "open" position. One of the objectives of the measurements on these samples was to investigate the influence of panel vibrations on the absorption characteristics. Thus, unlike the microhorn samples, no supporting bars were used.

Impedance measurements in Kundt's tube

The specific impedance at normal sound incidence of the adjustable, slitted double panel samples was measured using the same square Kundt's tube and equipment that was used for measurements on microhorns. See Sec. 3.2.2. The transfer function method was used as before. In addition, to measure the influence of panel vibration, a *Polytec* OFV-2200 laser vibrometer was used [*Polytec*, 1999] to measure the vibration velocity at several positions on the plates. The vibrometer outputs a voltage proportional to the velocity amplitude in the direction of the laser beam. During the measurements described here, the laser beam was approximately normal to the panel surface. Therefore, the output voltage was assumed to be approximately proportional to the normal velocity. Figures 4.20 and 4.21 show an overview of the measurement setup, and a sketch showing the relevant dimensions. The distances t and s were the same as in Sec. 3.2.2, that is $t = 310\,\text{mm}$, and $s = 150\,\text{mm}$. The sample was

Table 4.9: *Dimensions of the measured adjustable, slitted double panels. See Fig. 4.10 for definition of symbols. All plates were* 0.7 mm *thick.*

Panel	g mm	b mm	w_1 mm	w_2 mm	q mm
A	0.25	14	3.0	3.0	0, 3, 5, 6 and 7
B	0.45	42	7.0	7.0	0, 4, 7, 10, 13, 16, 19 and 21
C	0.10	10	3.0	3.0	0, 2, 2.5, 3, 3.5, 4 and 5
D	0.12	10	2.0	2.0	0, 1, 1.5, 2, 2.5, 3, 4 and 5

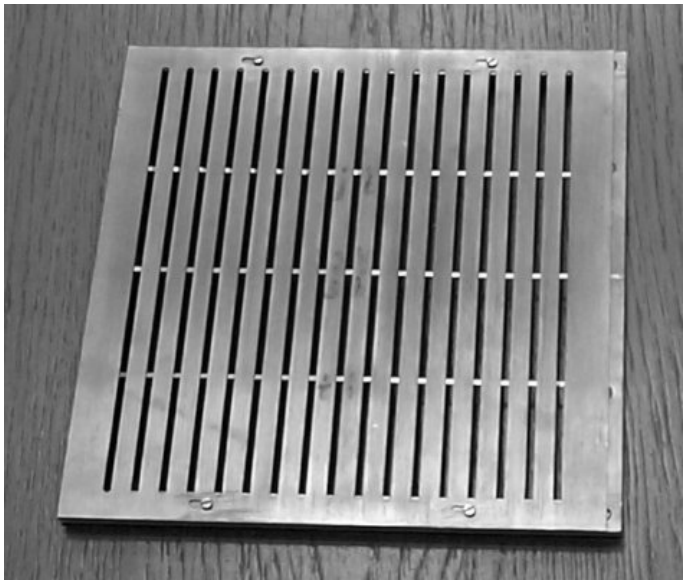

Figure 4.19: *Sample of adjustable slitted panel absorber, mounted to the sample holder. The panel is in the "open" position, and is seen from the rear side. Three of the five thin copper strips which keep the plates separated can be seen. These strips were glued to the front plate.*

fastened to the sample holder with screws, as shown in Fig. 4.19. Three values of the back cavity depth d were used; 300, 150 and 75 mm.

For a given transfer function between the microphones, H_{12}, the specific impedance was calculated by Eq. (3.27). The transfer function H_{12} was measured by the computer program *WinMLS*, described in Sec. 3.2.2. All four of the sound card channels were used here; one for the output MLS-signal, two for the microphone signals, and one for the velocity signal from the laser. For all measurements and calibrations, the measurement parameters were the same as in Sec. 3.2.2: The sampling rate was 11025 Hz, the sequence order 14, and the number of averages was 16.

To relate the measured plate vibration quantitatively to the dips and peaks in the absorption coefficient as function of frequency, the measured velocity was normalized with a factor proportional to the incident sound intensity. As given by *Vigran* [1985], the incident intensity is a function of H_{12}:

$$I_{\mathrm{i}} \propto \left[\exp(\mathrm{j}ks) - H_{12}\right]^2, \tag{4.22}$$

where $k = \omega/c$ is the wavenumber and s is the microphone distance. Then the normalized velocity is given by

$$v_{\mathrm{sf}} = \frac{H_{\mathrm{laser}}}{\left[\exp(\mathrm{j}ks) - H_{12}\right]^2}, \tag{4.23}$$

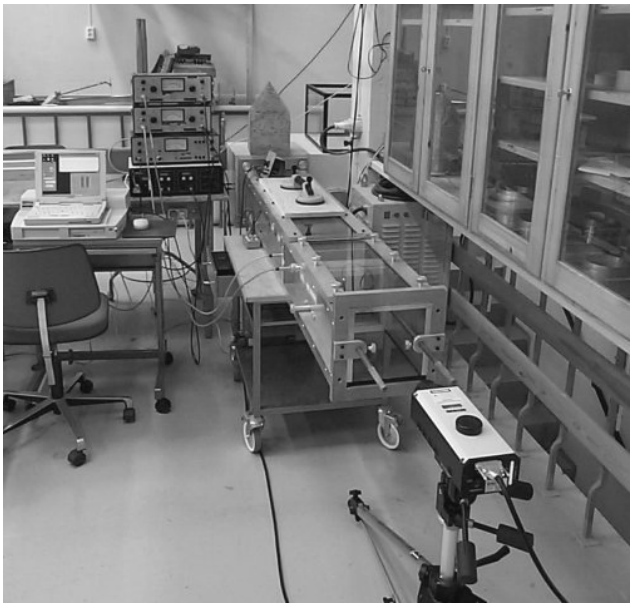

Figure 4.20: *The Kundt's tube, with microphone amplifiers to the left. The piston, which constitute the back wall of the tube, is made of thick glass, with a frame of aluminium. Thus, the laser at the rear end has an almost complete view of the mounted sample. In the background can be seen the anechoic end piece used during the calibration.*

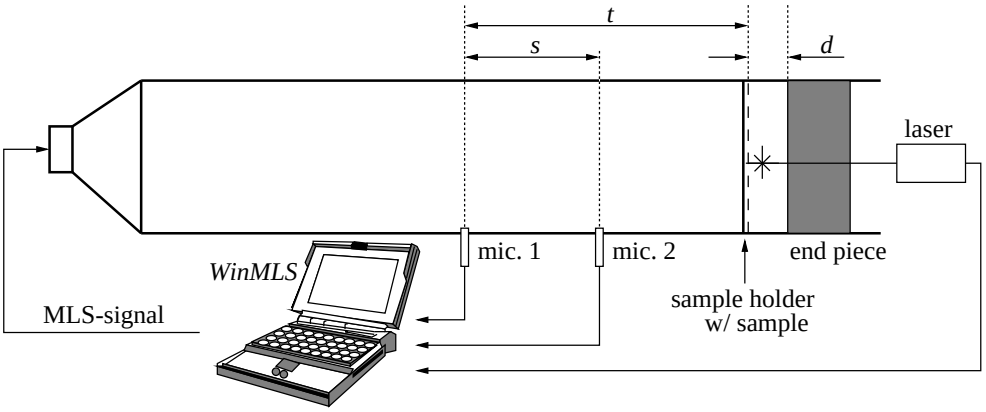

Figure 4.21: *The setup used for normal incidence impedance and vibration velocity measurements of the slitted double panel. The transfer function between the microphones and the vibration normalized velocity, Eq. (4.23), was calculated by the computer programs* WinMLS *[*Morset Sound Development, *1999] and* Qintv *(Sec. A.4). During all measurements,* $t = 310\,\text{mm}$ *and* $s = 150\,\text{mm}$*. Three values of* d *were used; 300, 150 and* $75\,\text{mm}$*.*

where H_{laser} is the Fourier transform of the measured velocity impulse response.

Simulations

The geometries in Table 4.9 were simulated by the model presented in Sec. 4.2.1. Alternative values of the gap width g were also simulated. These values are given together with the results. A comprehensive set of simulations was also carried out to investigate the influence of all the eight geometry parameters (w_1, w_2, t_1, t_2, b, q, g and d in Fig. 4.10). For all the FDM simulations, the simulation parameters were the same as in the preceding section, given in Table 4.7. The simulations were done at $1/3$ octave spaced points in the frequency range $39.7 - 2016\,\text{Hz}$, and also for the frequency $f = 2194\,\text{Hz}$, corresponding to $\lambda = d$.

To compare the slitted double panel resonator with MPPs, the absorption of two MPPs were calculated using the FLAG program (see page 39). As before, the perforation separations were chosen to give approximately the same resonance frequency as the resonance frequencies of the double panels. MPP A had a 0.94% perforation, and MPP B had a 0.76% perforation. The panel thickness was 1 mm, and the perforation radius was 0.5 mm. The back cavity thickness $d = 150\,\text{mm}$. The simulations were done at $1/30$ octave spaced points in the frequency range $35 - 1094\,\text{Hz}$.

4.3.3 Results

Note: To increase the readability, all length dimensions in the rest of this section are given without units. Unless otherwise stated, all lengths are given in millimeters. Also note that the plate thickness t or the slit width w are given without indices when one or both of these dimensions are the same for both plates.

Velocity profiles

The Finite Difference model that was applied to the inner parts of the slits and to the gap between the plates, is a linear model. The assumption of linearity fails if the velocity in the resonator neck is above a certain level. As mentioned in relation to Eq. (4.15), the driving pressure of the model was arbitrarily set to 1 Pa (or 94 dB). Note that this is the assumed sound pressure *inside* the front slit, at $m = 0$ in Fig. 4.11. Based on this, the maximum values of the horizontal and vertical velocity u and v were calculated for one typical geometry. The results are presented in Table 4.10. The maximum velocity, $5\,\text{cm/s}$ is the horizontal velocity in the gap between the plates when the resonator is in the "closed" state, and the frequency equals the resonance frequency. This velocity was found to be a factor 100 lower than the velocity which mark the onset of nonlinearity, as discussed in Sec. 2.3.2. Thus, assuming that the sound pressure in the front slit is not significantly lower than the driving pressure, the linear model should be valid for sound pressure levels up to about 134 dB.

Figure 4.22 shows the calculated velocity fields for the geometries and frequencies listed in Table 4.10. The velocity has a horizontal component some distance inside the slits, especially in the rear slits. This justifies the extension of the FDM a distance $\Delta z S_i$ into the slits. In general, the velocity profiles in the slits and in the gap between the plates have the qualitative properties described by *Craggs and Hildebrandt* [1984] (see page 14). The dimension

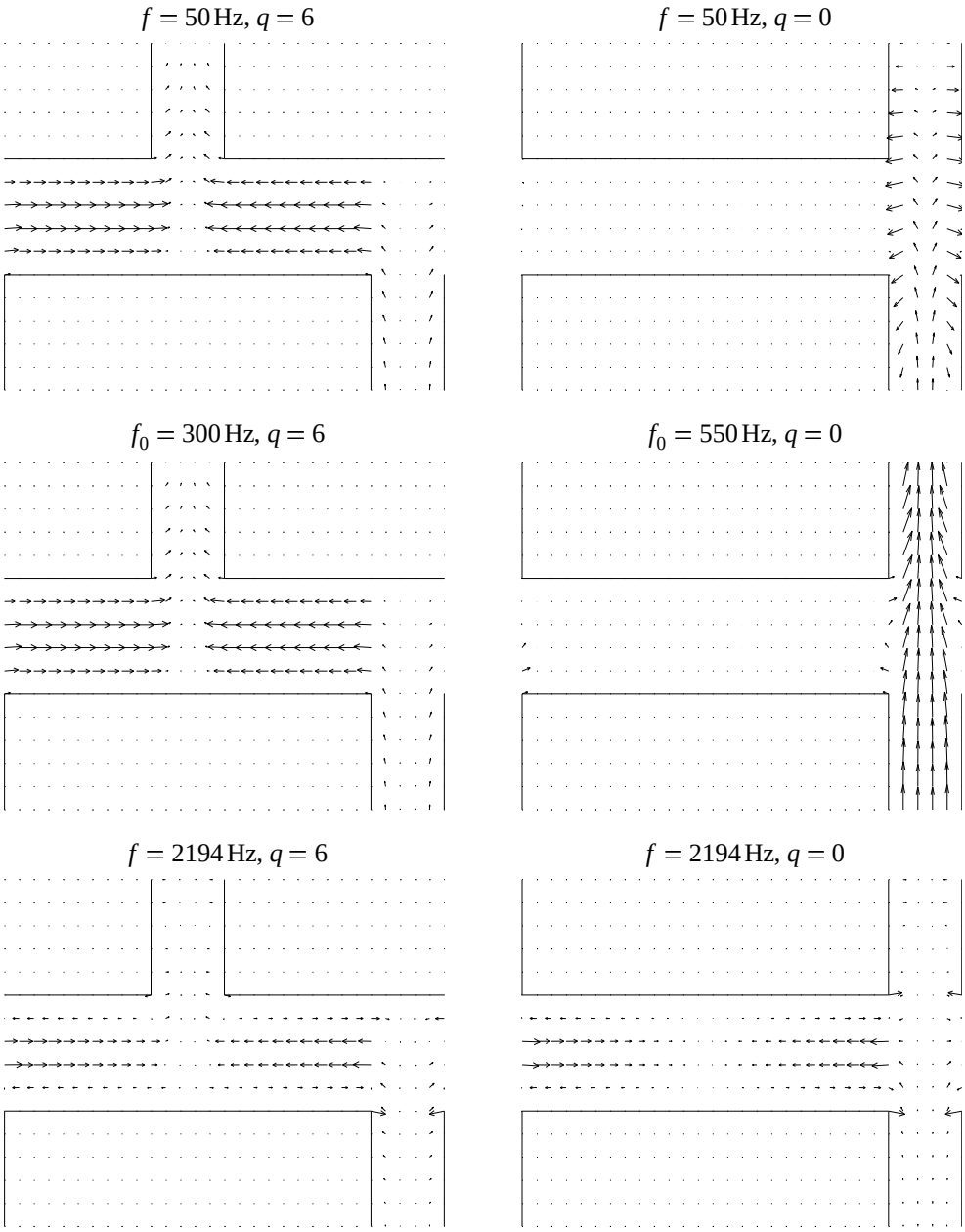

Figure 4.22: *Velocity fields of adjustable slitted double panels. The rear slit is* up *in the figures. The geometries and frequencies are the same as in Table 4.10. Note that to increase clarity, only every second grid point has been included. Also note that the scales in the figures differs by a factor 1000. Please refer to Table 4.10 to compare the velocities.*

Table 4.10: *Calculated* maximum *velocities of a typical slitted double panel in the "open" ($q = 0$) and "closed" ($q = 6$) states. The other geometry parameters were: $w = 2$, $t = 1$, $g = 0.16$, $b = 12$ and $d = 155$. The rows in bold typeface represents calculations for frequencies near resonance. The frequency* 2194 Hz *corresponds to* $d = \lambda$.

f Hertz	q mm	u (max) cm/s	v (max) cm/s
50	0	0.007	0.005
550	**0**	**0.5**	**1**
2194	0	0.009	0.001
50	6	0.7	0.1
300	**6**	**5**	**1**
2194	6	0.01	0.002

of the gap in this example is of the order of the viscous boundary layer thickness, and so the velocity profile in the gap is parabolic. The slit widths are large compared to the boundary layer thickness, so the velocity profiles there have a flat central part. This is best observed in the front slit, where the horizontal velocity components are less dominant than in the rear slit.

The shapes of the velocity fields in the "closed" state are surprisingly similar for the low frequency, $f = 50$ Hz and the resonance frequency, $f = f_0 = 300$ Hz, although the difference in magnitude is about 10, according to Table 4.10. The frequency $f = 2194$ Hz corresponds to $\lambda \approx d$, *i. e.* a standing wave in the back cavity. For this frequency, there is almost no net flow in the resonator neck. The relatively low velocities listed in the table correspond to the "rotational" flow that can be seen in the figure. The effect of the standing wave is also evident in the "open" state for the same frequency. It is interesting to note that at resonance, the maximum vertical velocity (corresponding to the velocity of the flow in the slits) is equal for the "closed" and "open" states of the double panel resonator. However, the horizontal velocities differs by a factor of 10. As the viscous energy dissipation is proportional to the square of the velocity to a surface, it is clear that the slits contributes very little to the dissipation of the sound energy.

Effect of geometry parameters

The results discussed in Sec. 4.2.3 gave an indication of the relative importance of the many geometry parameters used in the model. As the model was verified to be in reasonably accordance with experiments, a large series of simulations was done to systematically evaluate the effect of all eight geometry parameters. The main results of these simulations are presented in the following paragraphs.

Symmetry of plates The velocity fields in the slits were expected to be similar, so it was assumed that the plates should be interchangeable. An exchange of plates should not alter the

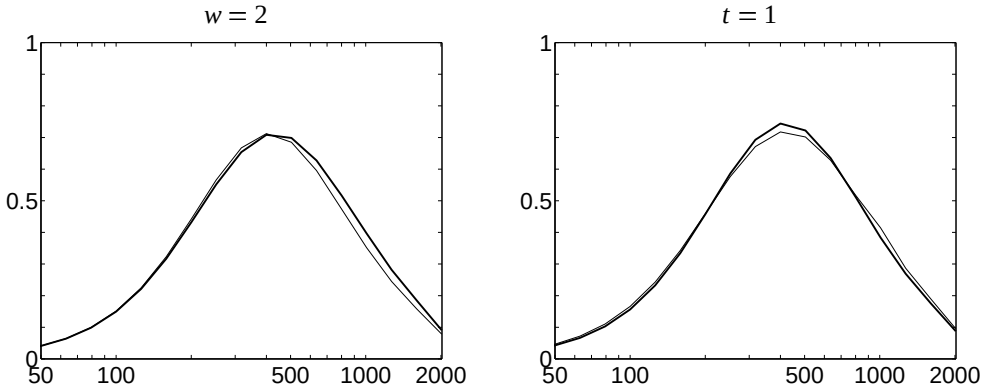

Figure 4.23: *Effect of exchange of plates of different thickness and with different slit widths. Absorption coefficient as function of frequency. See Fig. 4.10 for definition of symbols. For both graphs,* $b = 12$, $q = 6$, $d = 75$ *and* $g = 0.16$. *Left graph: ——,* $t_1 = 1$ *and* $t_2 = 2$*; ——,* $t_1 = 2$ *and* $t_2 = 1$. *Right graph: ——,* $w_1 = 1$ *and* $w_2 = 2$*; ——,* $w_1 = 2$ *and* $w_2 = 1$.

absorption characteristics. However, as demonstrated above, the velocity fields in the front and the rear slits were not completely similar. Figure 4.23 shows the effect of an exchange of plates of different thickness and with different slit widths. This figure shows that the plates of different dimensions are *not* completely symmetric, but the difference is so small that there is probably no need to consider this effect as part of a design process. To exclude the small effect of asymmetry, all the other geometries presented here had $t = t_1 = t_2$ and $w = w_1 = w_2$.

Effect of slit width and plate thickness Figure 4.24 shows the effect of a change in the plate thickness t and the slit width w. Simulations were also done with $t = 2$ and $w = 2$. These results are excluded to simplify the figure. By comparing the left column with the right column of Fig. 4.24, it is clear that the plate thickness is practically insignificant, at least for the relatively normal thicknesses considered here. This has the practical consequence that the plate thickness can be chosen solely on the basis of physical requirements. The slit width, on the other hand, may seem to have a significant influence on the absorption characteristics, according to the graphs in Fig. 4.24. This is probably not the case. As seen from Fig. 4.10 on page 59, the *effective* length of the gap between the front slit and the rear slit is $q - w_1/2 - w_2/2 = q - w$. A change in w will therefore change the effective gap length equivalently. By comparing the top left graph in Fig. 4.24 with the middle left graph in Fig. 4.27, the effect of w may be compared with the effect of q.

Effect of plate separation The plate separation was expected to be the most important parameter. The discussion in the beginning of Sec. 2.2 and the results of Sec. 4.2.3 indicate that for a given value of b (or q), there exists an optimum value of g. The existence of this optimum is confirmed by the graphs in Fig. 4.25. To increase the clarity, each graph includes only every third of the geometries that were simulated. The graphs clearly indicate the optimum value of g for the three values of b simulated. As expected, the optimum value of g increase

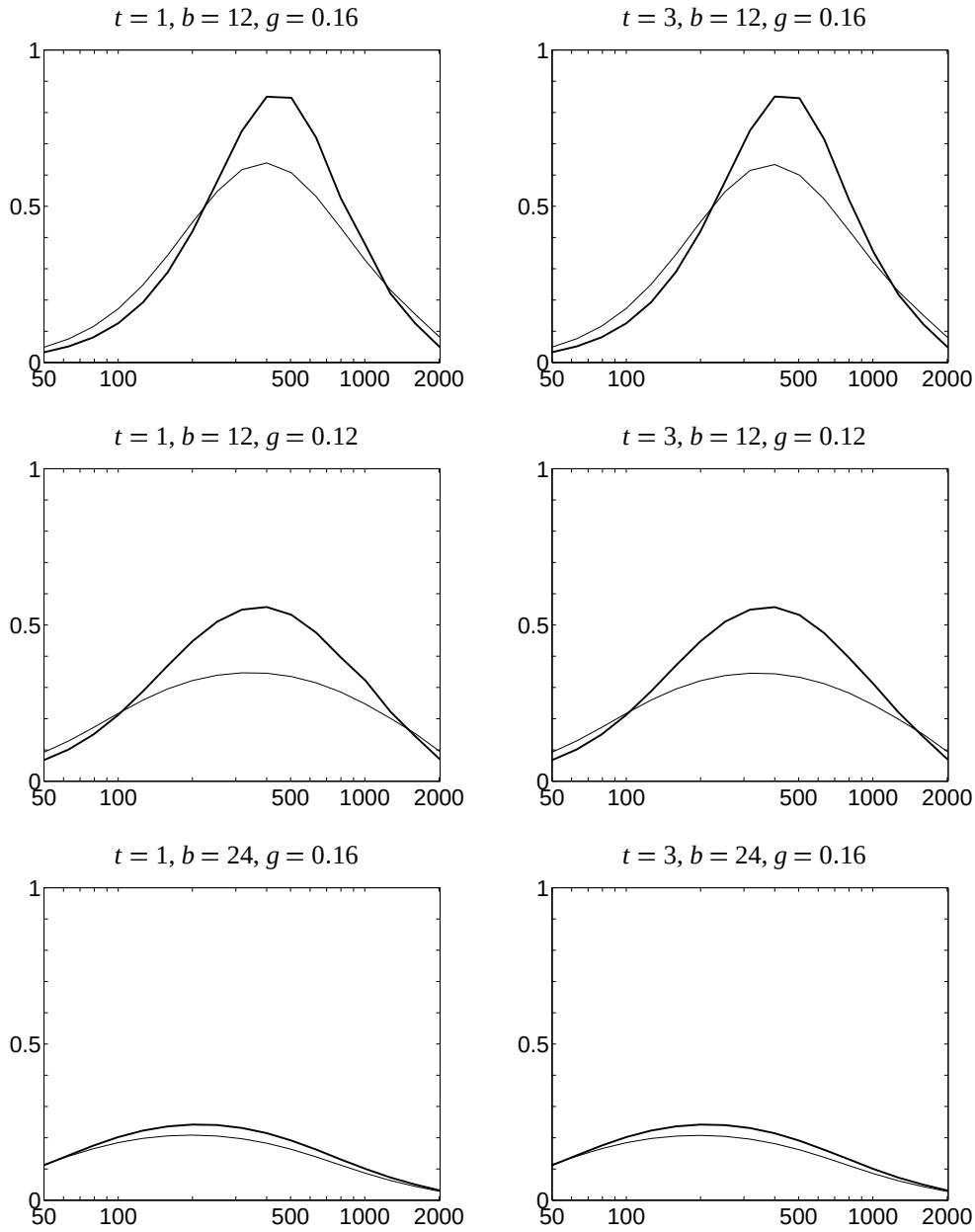

Figure 4.24: *Effect of plate thickness and slit width. Absorption coefficient as function of frequency. See Fig. 4.10 for definition of symbols. For all graphs,* $d = 75$ *and* $q = b/2$. ——, $w = 1$; ——, $w = 3$.

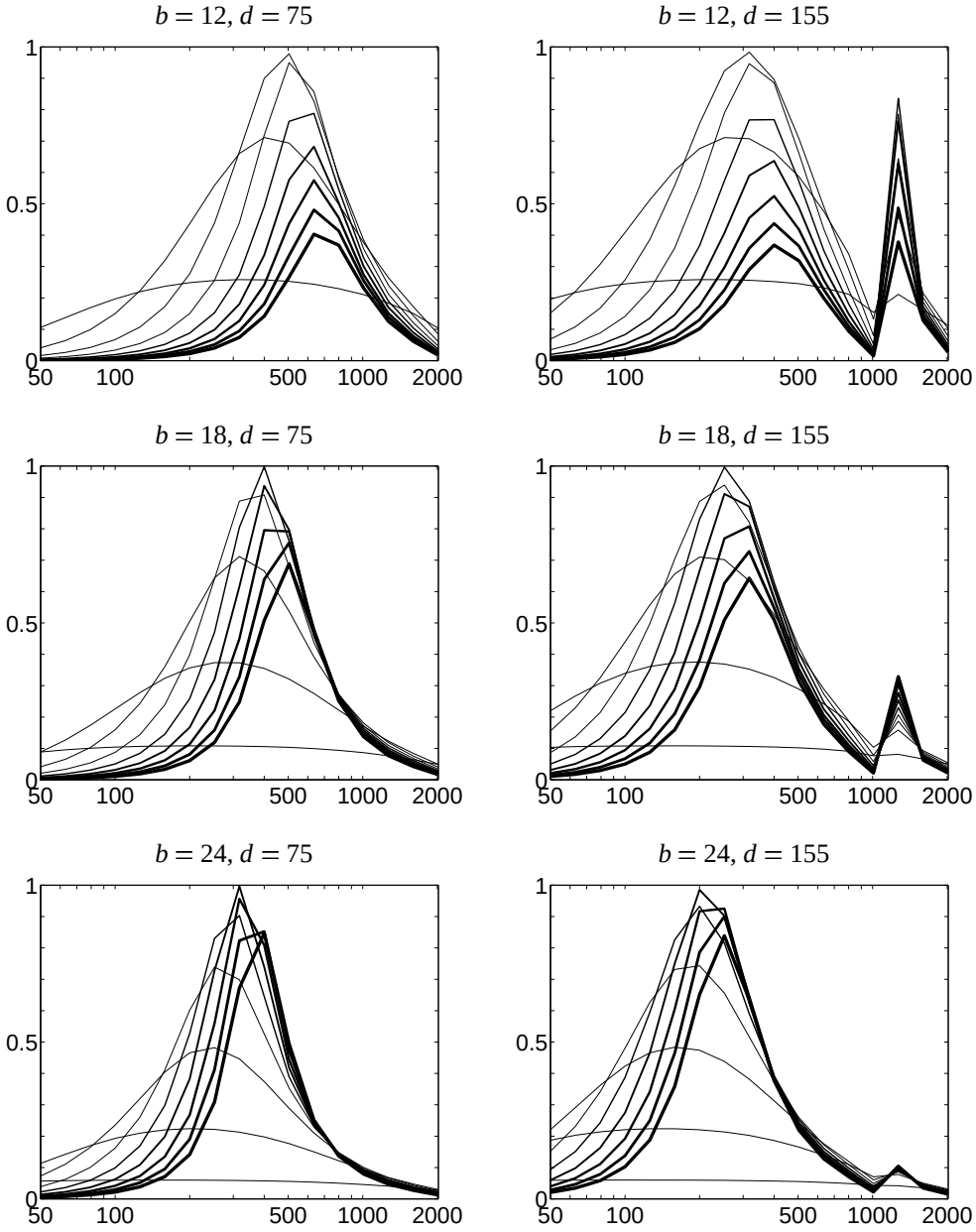

Figure 4.25: *Effect of plate separation. Absorption coefficient as function of frequency. See Fig. 4.10 for definition of symbols. For all graphs,* $w = 2$, $t = 1$ *and* $q = b/2$. *The curves correspond to plate separations* $g = 0.10$, 0.16, 0.22, 0.28, 0.34, 0.40, 0.46, 0.52 *and* 0.58. *Thicker lines correspond to larger values of g.*

for larger values of b, and is independent of d. However, the absorption bandwidth decreases for larger values of b. Thus, if high absorption over a large frequency range is required, the plate separation is limited to a rather low value. The resonance frequency increases when g increases, due to the reduction of the effective mass.

Effect of center-center distance between slits The effect of variation in the center-center distance between slits is shown in Fig. 4.26. These results are similar to those in Fig. 4.25, and shows that for a given g there exists an optimum value of b. As discussed above, a larger value of g corresponds to a larger optimum b, at the cost of a reduced absorption bandwidth. The resonance frequency decreases when b increases. Simulations with $g = 0.40$ are not included in Fig. 4.26. These simulations showed the same tendency as $g = 0.20$, with the maximum absorption coefficient occurring at $b = 22$.

Effect of slit separation Figure 4.27 shows the effect of variation in the slit separation, *i. e.* the lateral distance q between the centers of the front and rear slits. As shown in Fig. 4.26, for $g = 0.16$ the maximum absorption corresponds to $b = 8$. Thus, for $b = 12$ the absorption is maximum for a slit separation $q < b/2$, while for $b = 6$, the slit separation $b/2$ gives the largest possible absorption. If b is larger than the optimum value, the optimum value of q is less than $b/2$. As with g and b, a change in q causes a frequency shift. As shown in the middle left graph, this can be used to make a resonator with shiftable resonance frequency.

Summary It has been found that for the slitted double panel absorber, the plates are interchangeable. For plates of normal thickness, the thickness of the plates is of no practical significance. A change in the slit width, or a change in the lateral distance between the front and rear slits both cause a change in the *effective* length of lateral gap. For a given application, there exists an optimum combination of this effective gap length and the gap width. A change in plate separation g, center-center distance between slits b, or slit separation q may cause a significant change in the maximum absorption, absorption bandwidth or resonance frequency. As described in Sec. 4.3.2, the slit separation can be easily by changed. Thus, the adjustable slitted panel concept offers the possibility of resonators where the maximum absorption or the resonance frequency can easily be changed.

Panel vibrations

As stated earlier, one of the objectives of the measurements described here was to evaluate the influence of panel vibrations on the absorption characteristics. Figures 4.28 and 4.29 shows the modulus and phase of the measured normalized vibration velocity as function of frequency for several positions and configurations. All these measurements were done on panel A, defined in Table 4.9. The first four peaks, in the frequency range $20-55$ Hz, seems to be practically equal for all graphs, and are probably an artifact of the measuring system. The main vibration mode of the panel, at 77 Hz, shows the expected characteristics; The vibration velocity is smaller near the edge of the panel than it is at the center. The velocity is larger for a deeper back cavity. When the panel is in the "open" state, the vibration velocity becomes significantly smaller. This is in accordance with what was reported by *Tanaka and*

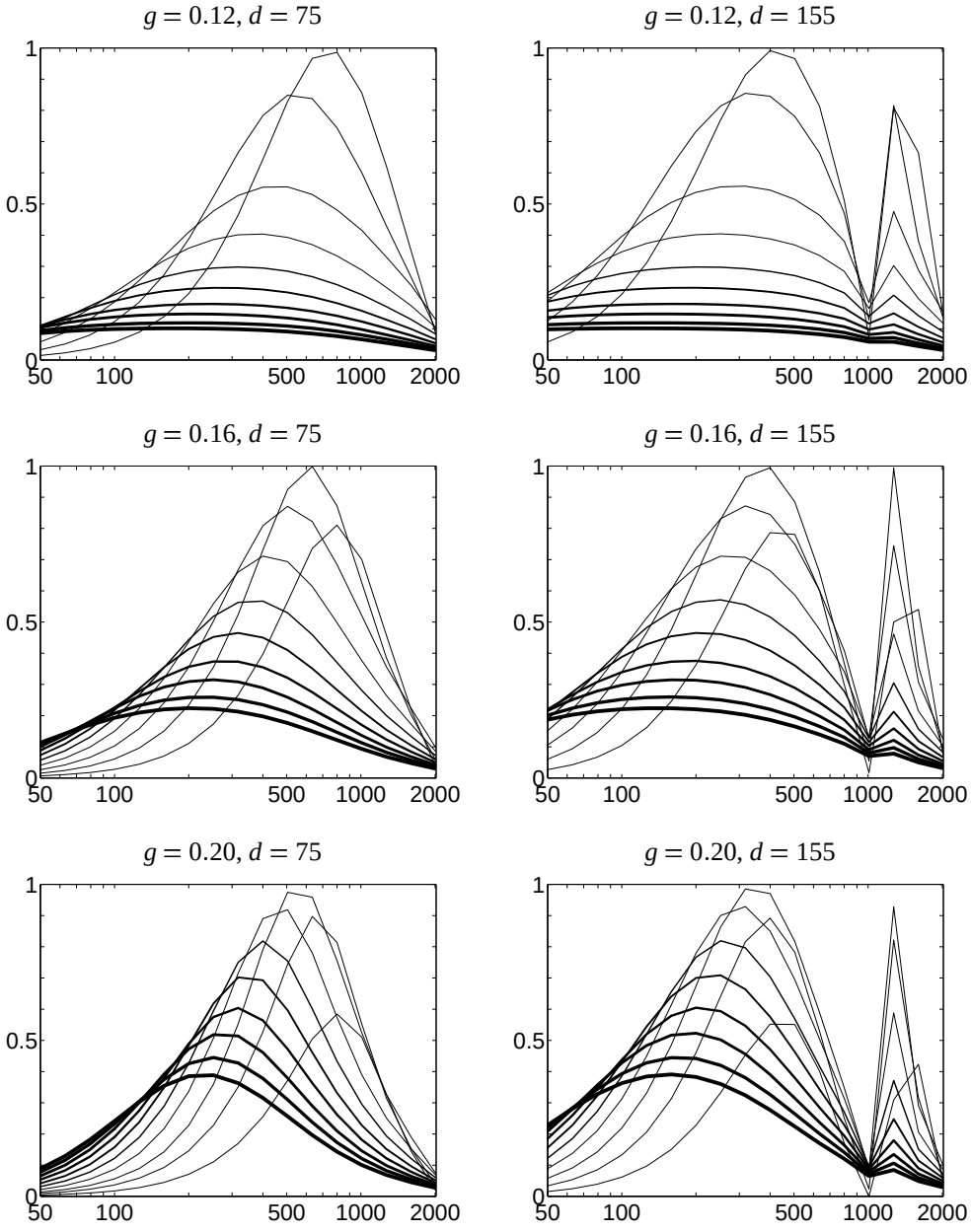

Figure 4.26: *Effect of center-center distance between slits. Absorption coefficient as function of frequency. See Fig. 4.10 for definition of symbols. For all graphs,* $w = 2$, $t = 1$ *and* $q = b/2$. *The curves correspond to center-center distance between slits,* $b = 6$, 8, 10, 12, 14, 16, 18, 20, 22 *and* 24. *Thicker lines correspond to larger values of* b.

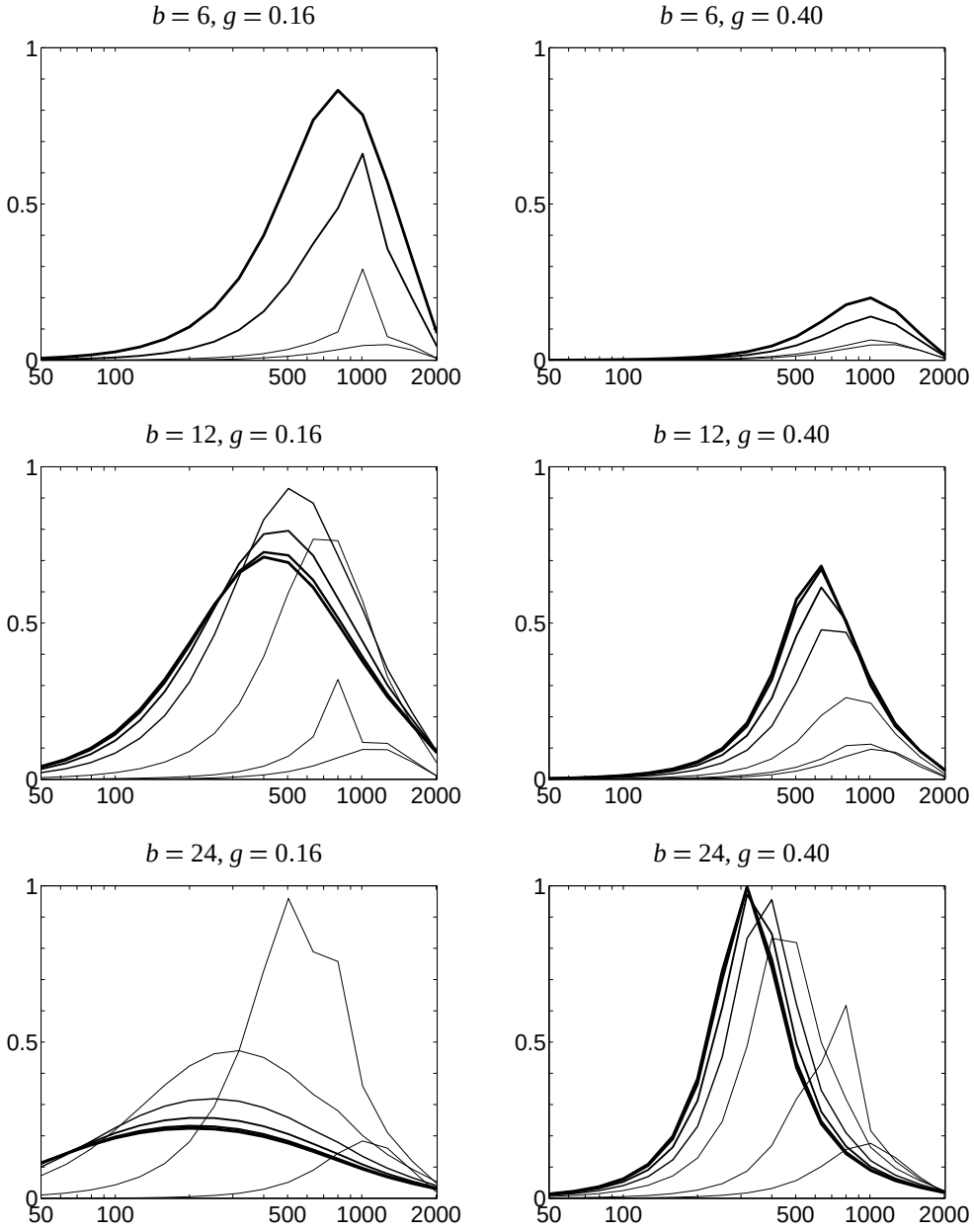

Figure 4.27: *Effect of slit separation. Absorption coefficient as function of frequency. See Fig. 4.10 for definition of symbols. For all graphs,* $w = 2$, $t = 1$ *and* $d = 75$. *The curves correspond to slit separations* $q = 0$, $b/12$, $b/6$, $b/4$, $b/3$, $5b/12$ *and* $b/2$. *Thicker lines correspond to larger values of q.*

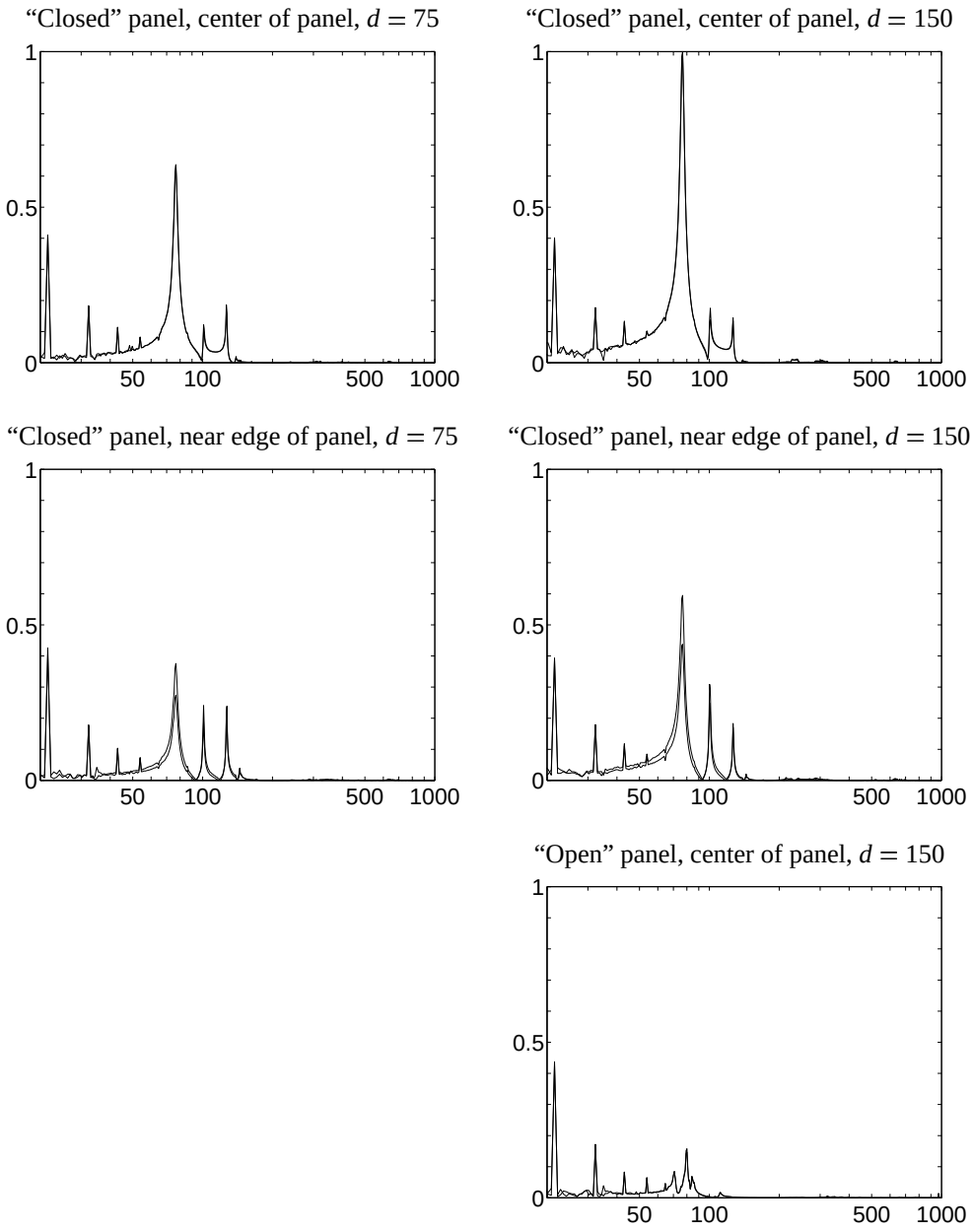

Figure 4.28: *Measured panel vibration for some measuring positions and panel states. Modulus of normalized vibration velocity as function of frequency. The ordinate has been scaled so that the maximum value equals 1. The measurements were done on panel A (see Table 4.9).* ——*, front plate;* ——*, rear plate.*

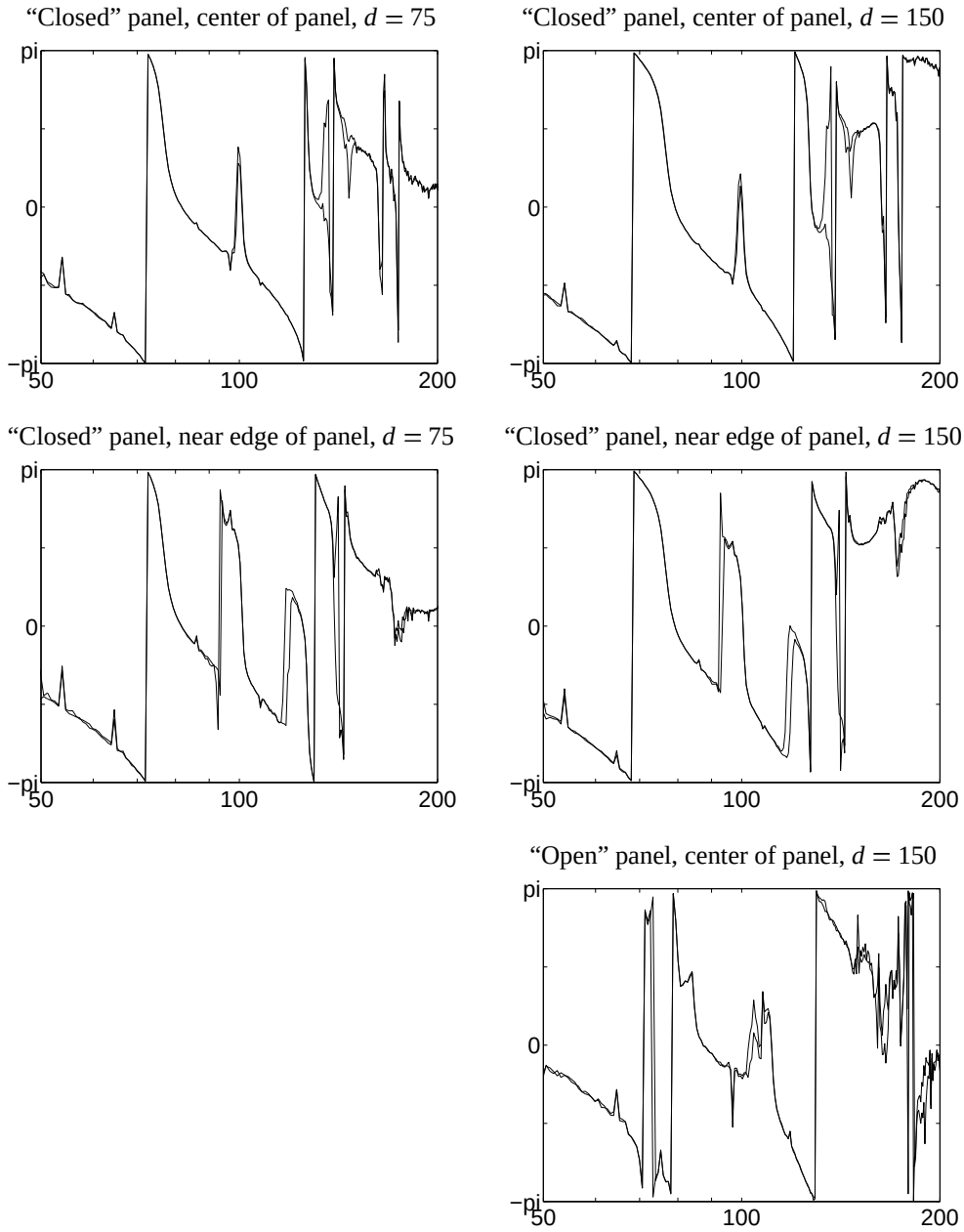

Figure 4.29: *Measured panel vibration for some measuring positions and panel states. Phase of normalized vibration velocity as function of frequency. The measurements were done on panel A (see Table 4.9).* ——*, front plate;* ——*, rear plate.*

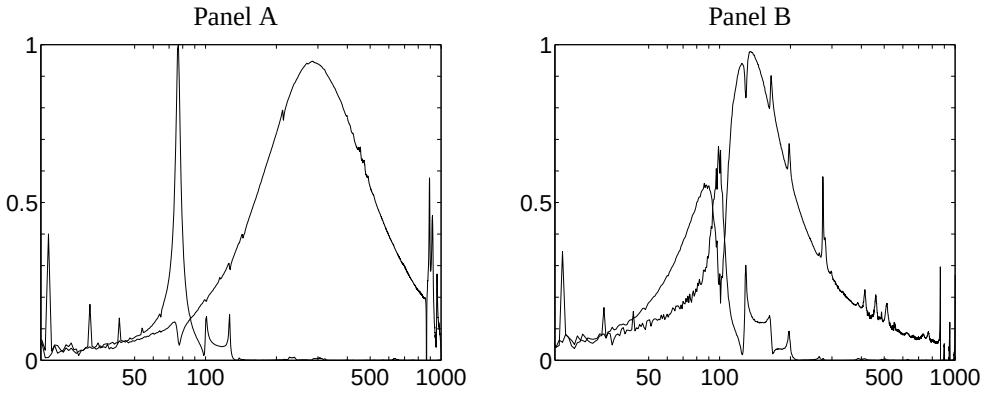

Figure 4.30: *Modulus of normalized panel vibration velocity and absorption coefficient as function of frequency. See Table 4.9 for geometry definitions. The back cavity depth was* $d = 150$ *for both panels. The velocity, measured at the center of the panel, has been scaled so that the maximum value equals 1.* ——*, vibration velocity;* ——*, absorption coefficient.*

Takahashi [1999] for perforated panels with large openings (see page 21). The graphs show that the vibration velocities of the two plates seem to have the same amplitude and, as shown in Fig. 4.29, practically the same phase. Consequently, the plate separation is not influenced by panel vibrations. Figure 4.30 compares the vibration modes with the dips and peaks of the absorption coefficient for two different panels. It is evident that the panel resonances may influence the absorption coefficient significantly, especially for panel resonances with frequencies near the Helmholtz resonance. It is also worth noting that panel resonances below the Helmholtz resonance result in dips in the absorption coefficient, while panel resonances above the Helmholtz resonance result in absorption peaks. This is probably due to the relative phase of the panel vibration velocity and the particle velocity in the panel openings. When these velocities are in phase, the particle velocity in the panel openings (*i. e.* the velocity relative to the panel) is smaller. The result is a decrease in the energy dissipation and a dip in the absorption coefficient.

Sample measurements and simulations

Figures 4.31 and 4.32 compares the measured and simulated absorption coefficient for the panels listed in Table 4.9. The panels were in the "closed" state. The agreement between measurements and simulations is relatively good for panels A and B. For panels C and D, however, the real, average gap separation seem to have been significantly different from what was assumed and listed in Table 4.9. In the case of panel C, this discrepancy could be observed visually. In an attempt to estimate the real, average gap width, several different values of g were simulated. The plotted simulations $g = 0.22$ for panel C and $g = 18$ for panel D had the best agreement with measurements. Subsequent simulations of panel D (see Figs. 4.33 and 4.34) have used $g = 0.18$.

The measured and simulated effect of a variation in the slit separation q is shown in Fig. 4.33. Note that the curves have been cut at 100 and 850 Hz to exclude the effects of the

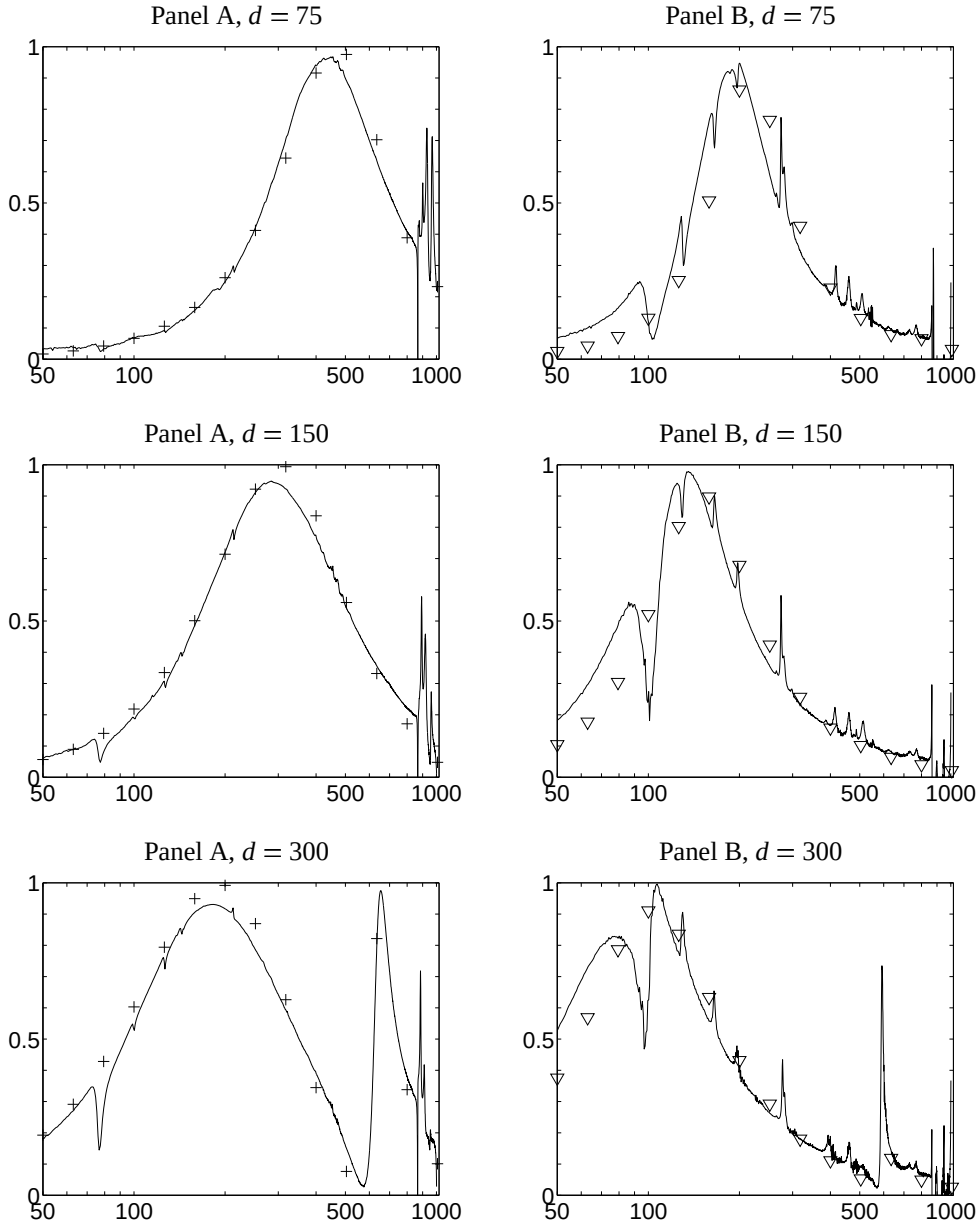

Figure 4.31: *Simulations and measurements of slitted double panels. Absorption coefficient as function of frequency. See Table 4.9 for geometry definitions. All panels were in the "closed" state. Left column: measured gap width* $g = 0.25$*, simulated gap width:* $+$*,* $g = 0.25$*. Right column: measured gap width* $g = 0.45$*, simulated gap width:* $\bigtriangledown$*,* $g = 0.45$*.*

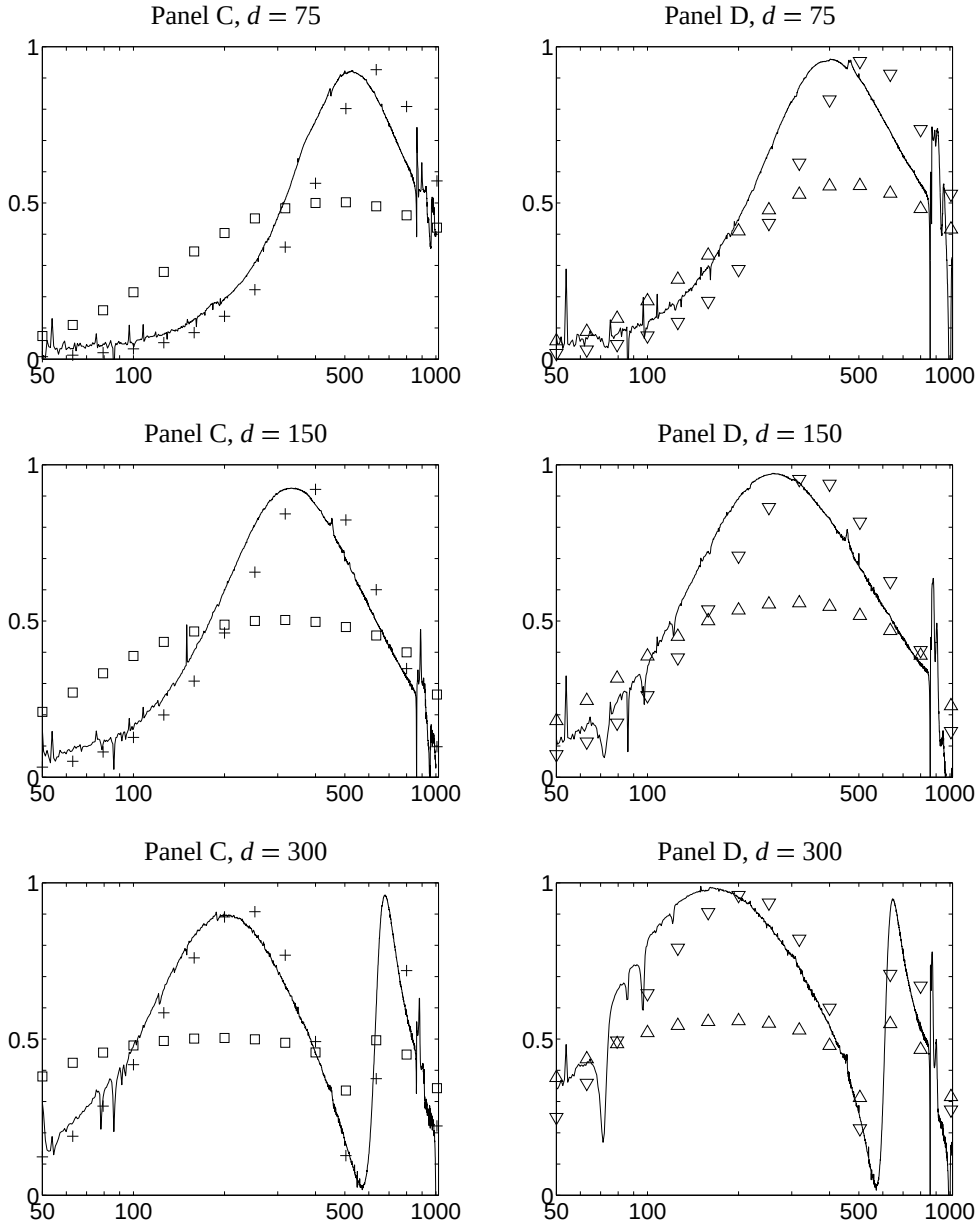

Figure 4.32: *Simulations and measurements of slitted double panels. Absorption coefficient as function of frequency. See Table 4.9 for geometry definitions. All panels were in the "closed" state. Left column: measured gap width* $g = 0.10$*, simulated gap widths:* $\square$*,* $g = 0.10$*;* $+$*,* $g = 0.22$*. Right column: measured gap width* $g = 0.12$*, simulated gap widths:* $\triangle$*,* $g = 0.12$*;* $\triangledown$*,* $g = 0.18$*.*

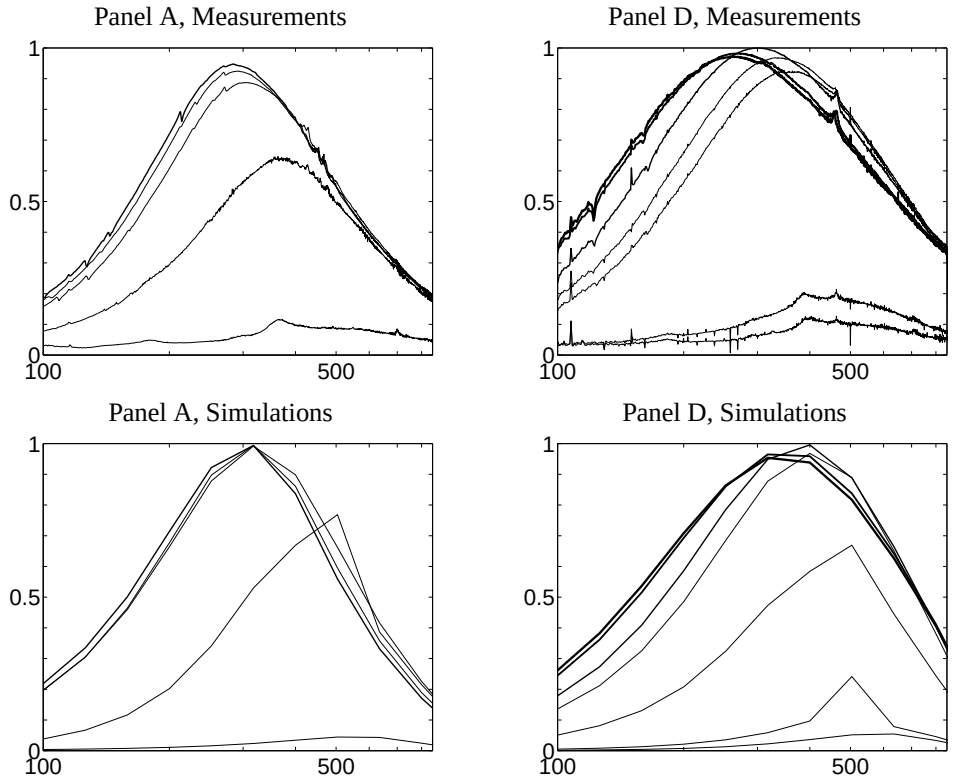

Figure 4.33: *Simulations and measurements of slitted double panels. Absorption coefficient as function of frequency for several values of q. See Table 4.9 for geometry definitions. The back cavity depth was* $d = 150$ *for both panels. For panel A, the curves correspond to slit separations* $q = 0$, 3, 5, 6 *and* 7. *For panel D, the curves correspond to slit separations* $q = 0$, 1, 2, 2.5, 3, 4 *and* 5. *Thicker lines correspond to larger values of q.*

main vibration mode of the panel and higher order modes in the Kundt's tube. As shown in Fig. 4.27, the absorption coefficient can be very sensitive to variations in q for intermediate values of q. Thus, some of the discrepancy between the simulations and measurements for intermediate values of q may be due to inaccuracies in the measured value of q. The general behavior with varying q is predicted by the simulations with a reasonable degree of accuracy.

Figure 4.34 compares the absorption coefficients of the "best" slitted double panels (panel A and D) with simulations of typical MPPs. The comparison with MPPs confirms the potential of the slitted double panel absorber. The results presented in Figs. 4.33 and 4.34 were the motivation for the work to be described in the next section.

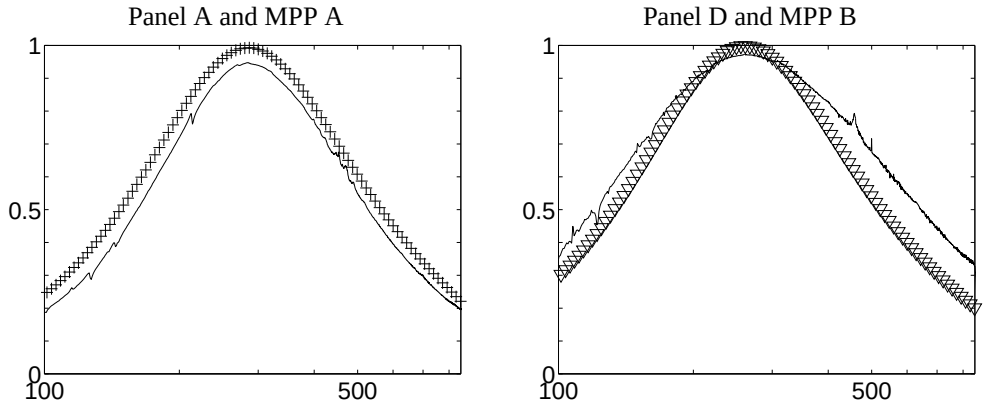

Figure 4.34: FLAG *simulations of MPPs and measurements of slitted double panels. Absorption coefficient as function of frequency. See Table 4.9 and page 74 for geometry definitions. The back cavity depth was* $d = 150$ *for all panels.* ——*, measured absorption coefficient;* $+$*, MPP A;* $\bigtriangledown$*, MPP B.*

4.4 Adjustable slitted panel absorber

The double panel absorber with adjustable slit separation seemed to have absorption characteristics equivalent to or better than typical microperforated panels. However, all measurements and simulations described in the preceding sections are valid for normal sound incidence only. This section describes the investigations on the double panel absorber in a diffuse sound field.

4.4.1 Model

The relative, specific impedance of an air cavity in front of a hard wall is

$$\zeta_{\text{air}}(\beta) = \frac{-\text{j}}{\cos\beta}\cot(kd\cos\beta), \tag{4.24}$$

where β is the angle of incidence and d is the thickness of the cavity. If a *locally reacting* perforated panel, *i. e.* a panel with impedance independent of the angle of sound incidence, is placed in front of the air cavity, the impedance becomes

$$\zeta(\beta) = \left[(\theta + \text{j}\omega\chi) + \zeta_{\text{air}}(\beta)\right]\cos\beta, \tag{4.25}$$

where θ and χ is the relative, specific resistance and reactance of the perforated panel. The absorption coefficient of the system is given by

$$\alpha(\beta) = \frac{4\Re(\zeta)}{|\zeta|^2 + 2\Re(\zeta) + 1}, \tag{4.26}$$

and the absorption coefficient in a diffuse sound field is given by the integral of $\alpha(\beta)$ [see *e. g. Morse and Ingard*, 1968, Ch. 9.5]:

$$\alpha_{\mathrm{st}} = \int_0^{2\pi} \mathrm{d}\beta' \int_0^{\pi/2} \alpha(\beta) \sin\beta \cos\beta \, \mathrm{d}\beta \tag{4.27}$$

This integral may be approximated by

$$\alpha_{\mathrm{st}} = 2\pi \sum_{m=1}^{M} \alpha(\beta_m) \sin\beta_m \cos\beta_m \, \Delta\beta, \tag{4.28}$$

where $\Delta\beta = \pi/2M$, and $\beta_m = m\Delta\beta$, and M is an integer.

For simplicity, the slitted double panel considered in this chapter is assumed to be locally reacting so that the theory above is applicable. However, the panel resistance θ and reactance χ are not explicitly given by the model described in Sec. 4.2.1. As shown in relation to Eq. (4.16), the impedance in front of the panel is dependent on the input parameter z_T, which is dependent on the impedance of the back cavity. Therefore, the calculation of the impedance in a diffuse field by Eq. (4.28) would require the time-consuming calculation of the impedance for a large number of incidence angles. As a more feasible alternative, the impedance of the gap between the panels is here approximated by Eq. (2.38):

$$Z_{\mathrm{gap}} \approx 0.5 \frac{\mathrm{j}\omega\rho_0 b/2}{g} \left[1 - \frac{\tanh\left(x_{\mathrm{s}}\sqrt{\mathrm{j}}\right)}{x_{\mathrm{s}}\sqrt{\mathrm{j}}} \right]^{-1} \tag{4.29}$$

The factor 0.5 is due to the fact that, as seen from the front slit, there are two gap lengths $b/2$ in parallel. The perforate constant of the gap, x_{s}, is given by Eq. (2.39), with w substituted by g. The total, relative, specific impedance of the system is then given by

$$\zeta_{\mathrm{dp}}(\beta) = \left[\zeta_{\mathrm{air}}(\beta) \frac{z_{\mathrm{a}}}{b} + Z_{\mathrm{s},2} + Z_{\mathrm{gap}} + Z_{\mathrm{s},1} \right] \frac{b\cos\beta}{z_{\mathrm{a}}}, \tag{4.30}$$

with $Z_{\mathrm{s},i}$ given by Eq. (4.10). Note that the slit length $l_i' = l_i = t$ for $i = 1, 2$. The statistical absorption coefficient is calculated by Eq. (4.28).

The model described here is intended to be an quick approximation, given the infeasibility of the Finite Difference Method. For simplicity, the model does not include corrections for end effects [see *e. g. Cremer and Müller*, 1978b, pp. 335-338].

4.4.2 Measurements and simulations

Dimensions of samples

Based on the results of the preceding sections, 25 full scale adjustable slitted panel absorbers were produced. The basic design was the same as for the samples described in Sec. 4.3.2. Figure 4.35 shows one of the panels. Table 4.11 summarizes the dimensions of the panels. As shown in the figure, there are four sections of slits. Each section is 140 mm wide, with 8 mm spacing. To keep the front and rear plates separated, five strips of adhesive tape were

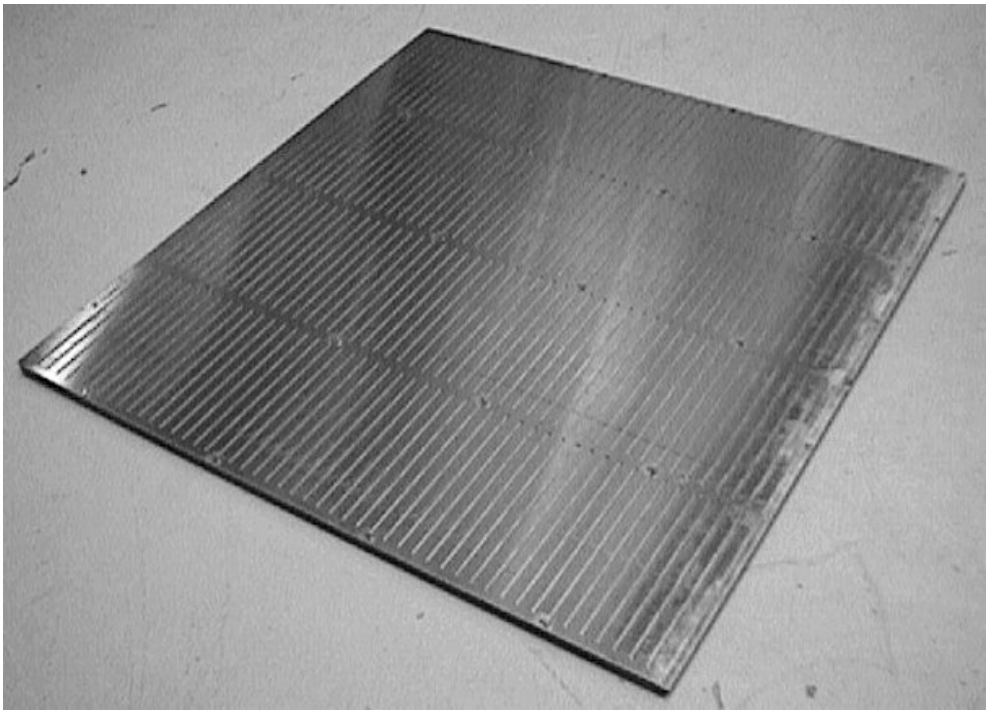

Figure 4.35: *Sample of full scale adjustable slitted panel absorber. The panel is in the "closed" state, and is seen from the front side. Barely visible are the screws used to fasten the front plate to the rear plate and the supporting frame.*

Table 4.11: *Dimensions of full scale adjustable slitted panels. See Fig. 4.10 for definition of symbols. The rear plate was* $600 \times 600\,\mathrm{mm}$ *and the front plate was* $594 \times 600\,\mathrm{mm}$*.*

Dimension	Length (mm)	
w	3	
t	0.7	
g	0.16	
b	12	
q	0, 3, 4, 5 and 6	for $d = 75\,\mathrm{mm}$
	0, 3, 3.5, 4 and 6	for $d = 155\,\mathrm{mm}$

fastened to the rear plate between (and outside) the sections of slits. The tape was 0.16 mm thick. Visual inspection showed that the plates were not completely plane, so the real, average distance between the plates was probably significantly larger than this. The rear panel was fastened with screws to a square frame of steel bars. To support the panel mechanically, there was also one steel bar at the middle of the panel. The cross-section of the steel bars was 8×10 mm. As shown in Fig. 4.35, the front plate was fastened to the back plate with screws through short slits in the front plate. These slits were placed along the strips of tape.

Absorption coefficient measurements in reverberation room

The absorption coefficient of the panels was measured according to *ISO 354* [1985] in a standard reverberation room with volume $268\,\mathrm{m}^3$. See Fig. 4.36. To minimize the effect of inaccuracies in the plate separation, the panels were laid with the front down, so that the weight of the steel frame would help keep the plates together. This is equivalent to the situation if the panels were mounted in a suspended ceiling. The panels were laid on T-profile steel bars, which were fastened to a rectangular frame of wood. The height of the frame was 70 mm. The total area of the setup was $3.024\,\mathrm{m} \times 3.072\,\mathrm{m} = 9.29\,\mathrm{m}^2$, which is a little low compared with the $10-12\,\mathrm{m}^2$ that is suggested by *ISO 354* [1985]. An extra frame, 80 mm high, was also made so that two different back cavity depths could be tested. Including the thickness of the T-profile steel bars, the distance d from the panel to the floor was 75 mm and 155 mm.

Two microphones were used in six positions in the room. The microphones used were *Brüel & Kjær* type 4145. The absorption coefficient was measured in $1/3$ octave bands in the range $100-5000$ Hz.

Simulations

Double panels with dimensions as given in Table 4.11 were simulated by the model described in Sec. 4.4.1. The number of discrete angles were $M = 45$. As an attempt to find the real, average gap width, several other values of the plate separation g were also simulated. The value $g = 0.25$ mm resulted in a good match with the measurements.

4.4.3 Results

Figure 4.37 shows the reverberation room measurements of the adjustable, slitted panel absorber. The effect of q is as expected (compare with Figs. 4.27 and 4.33). The maximum absorption is lower than was expected, however. As noted above, this is probably due to that fact that the average plate separation was significantly larger than 0.16 mm.

Figure 4.38 shows the measurements of the double panel absorber in the "closed" and "open" states, compared to simulation by the model described in Sec. 4.4.1. Simulations for the plate separation $g = 0.25$ mm corresponds reasonably well with the measurements, at least for $d = 75$ mm.

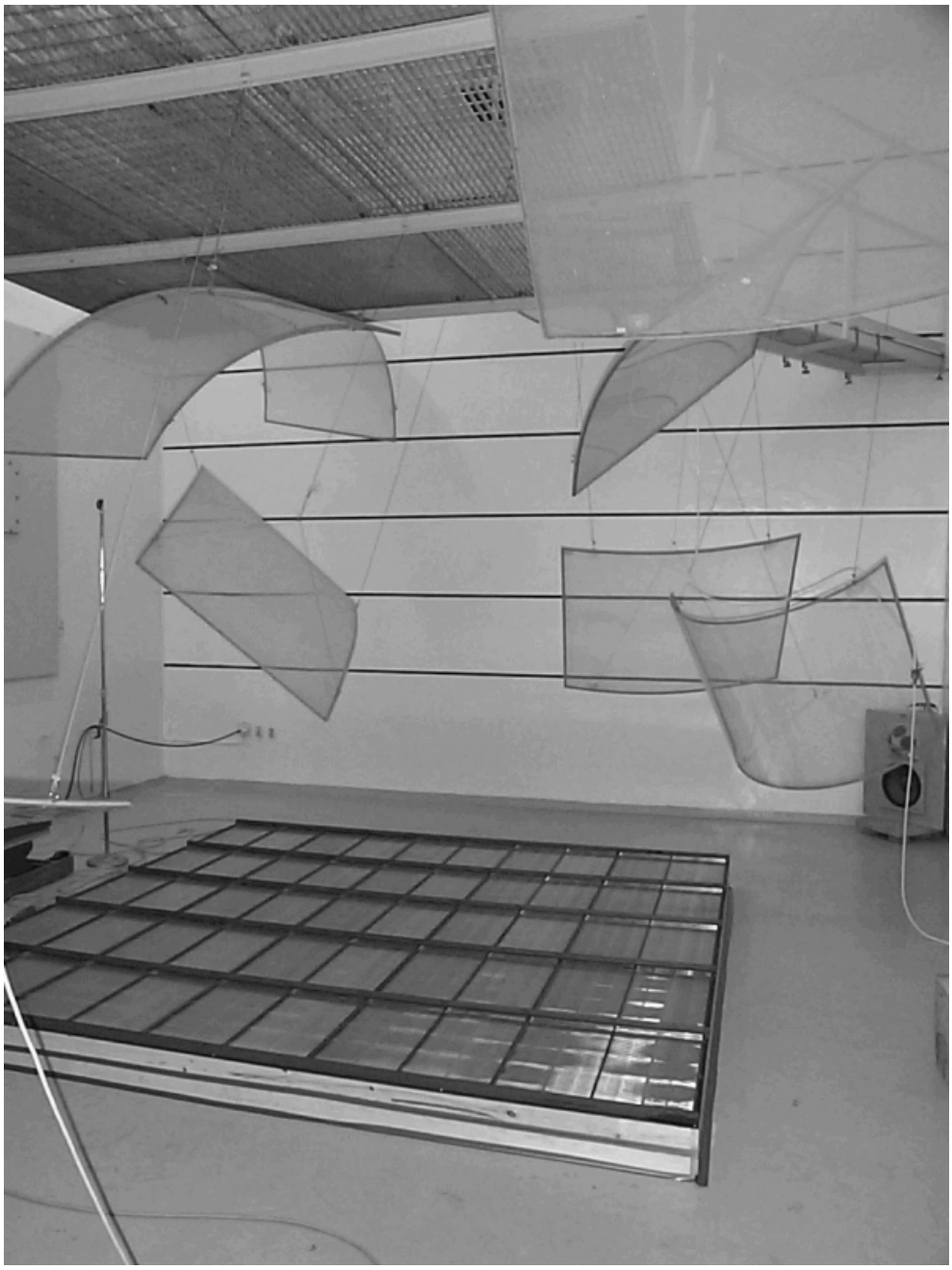

Figure 4.36: *Full scale adjustable slitted panels in the reverberation room. The panels were laid face down on supporting T-profiles. The total area of the samples was* $9.29\,\mathrm{m}^2$.

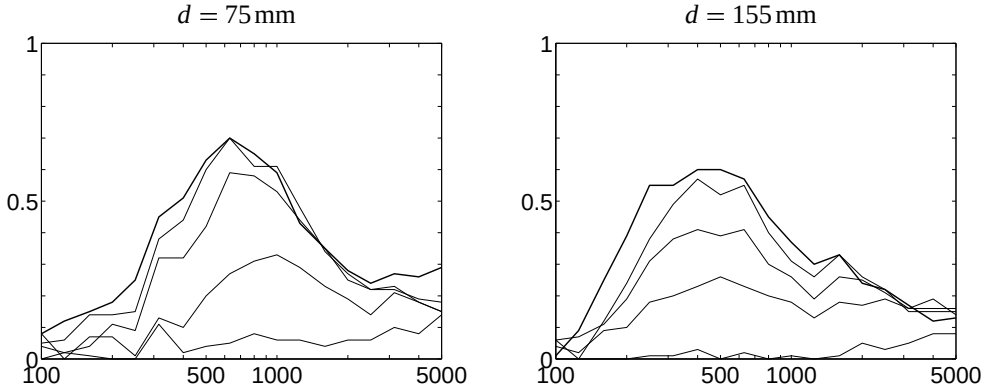

Figure 4.37: *Measurements of slitted double panels in a diffuse sound field. Absorption coefficient as function of frequency for several values of q. See Table 4.11 for geometry definitions. For the left graph, the curves correspond to slit separations* $q = 0$, 3, 4, 5 *and* 6 mm. *For the right graph, the curves correspond to* $q = 0$, 3, 3.5, 4 *and* 6 mm. *Thicker lines correspond to larger values of q.*

4.5 Summary

The double panel absorber concept has been investigated by analytical, numerical and experimental methods. Two variants have been examined: one where the plates have circular perforations, and one with slitted plates. It has been found that the double panel absorber is practically insensitive to the plate thickness. The most important design parameters are the thickness of the gap between the plates and the effective length of this gap, *i. e.* the distance between the panel openings of the two plates. With an optimal design, the double panel absorber may have an absorption bandwidth equal to or better than MPPs.

The slitted variant was simpler to model than the perforated variant. Additionally, the slitted double panel offered two distinct features that are not easily implemented with the perforated variant, or with microperforated panels:

– *Frequency shift*. The resonance frequency f_0 of the panel absorber can be shifted by adjusting the lateral distance between the slits in the front and the rear plate. From the simulations, it seems that at frequency shift of at least one octave is possible (at normal sound incidence), while keeping the absorption coefficient at 0.7 or larger.

– *Variation in absorption coefficient*. Also by adjusting the lateral slit separation, the absorption at resonance, α_0 can be varied from almost unity to a value close to zero.

To achieve a reasonable absorption bandwidth, the gap width g has to be quite small, in the range $0.1 - 0.3$ mm. In this range, the sensitivity to variations in g is very large. The method that has been used to keep g at a specified value is far from perfect. Thus, in the design process precautions must be taken to ensure that the value of g is kept as constant as possible.

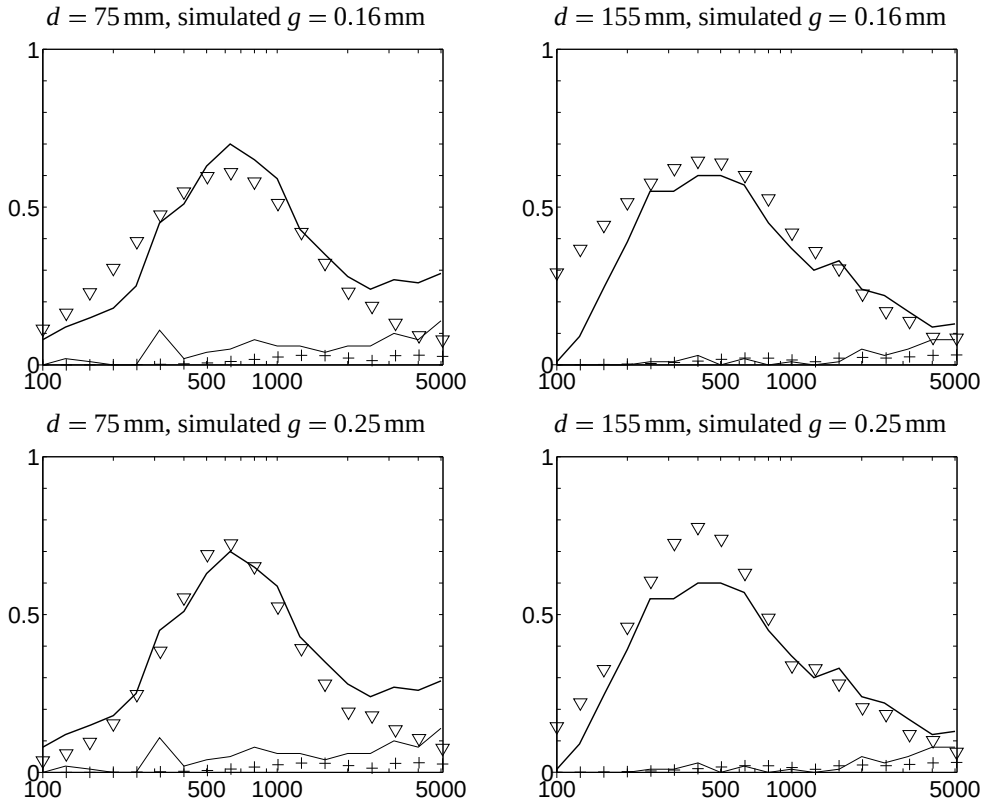

Figure 4.38: *Simulations and measurements of slitted double panels in a diffuse sound field. Absorption coefficient as function of frequency in "closed" and "open" states. See Table 4.11 for geometry definitions.* —, *measurement, "closed";*—, *measurement, "open";* $\bigtriangledown$, *simulation, "closed";* $+$, *simulation, "open".*

Chapter 5

Conclusions

This thesis has presented my work with two new perforated panel designs.

The microhorn panel absorber is a microperforated panel where the traditional cylindrical orifices have been shaped as small horns. The purposes of the horn-shape are to increase the surface area associated with each opening, increase the particle velocity in the inner part of the horn, and offer a better impedance match to the incoming sound wave. The microhorn concept has been investigated by the use of three models; the Finite Difference Method, the Finite Element Method, and an integration method based on the analytical expression for the impedance of a tube. Only the results of the FDM could, to some degree, be considered as qualitatively correct. According to these results, a relatively high absorption coefficient can be obtained over a relatively large bandwidth for microhorns with large outer radius and small inner radius. The microhorn absorber may have a potential as an "enhanced" microperforated panel. However, the model needs to be refined to give more accurate predictions and to evaluate the feasibility of the microhorn panel concept.

The double panel absorber consists of two parallel perforated or slitted plates separated by a small distance. The main part of the sound energy dissipation takes place in the small gap between the plates. The slitted variant is more easily modelled than the perforated variant, and offers two special features. By moving the plates relative to each other in the lateral direction, the maximum absorption coefficient can be adjusted from unity to almost zero, and the resonance frequency can be adjusted by an octave (for normal sound incidence). There are eight possible design parameters. FDM simulations and experiments on a number of samples have shown that the most important parameters are the *effective* length and thickness of the gap between the plates. The latter parameter is very sensitive. The plate thickness was found to be practically insignificant. The measured and simulated absorption coefficients of the double panel absorber have a bandwidth equivalent to, or slightly better than MPPs. To be of practical use, however, the panel design has to be improved so that the distance between the plates can be kept as constant as possible, and according to specifications.

Both panel absorber concepts illustrate that the distributed Helmholtz resonators without porous absorbers may obtain an acceptable absorption bandwidth by optimizing the design of the resonator orifices.

Bibliography

ACKERMANN U, FUCHS H V, and RAMBAUSEK N. Sound absorbers of a novel membrane construction. *Applied Acoustics*, **25**(3), 197–215 (1988)

ALLARD J F. *Propagation of Sound in Porous Media; Modeling Sound Absorbing Materials*. Elsevier (1993)

BODEN H and ÅBOM M. Influence of errors on the two-microphone method for measuring acoustic properties in ducts. *Journal of the Acoustical Society of America*, **79**(2), 541–549 (1986)

BROUARD B, ALLARD J F, BRUNEAU H, LAURIKS W, and VERHAEGEN C. Acoustical impedance and absorption coefficients of porous layers covered by a facing perforated by parallel slits. *Noise Control Engineering Journal*, **41**(1), 289–297 (1993)

BROUARD B, LAFARGE D, and ALLARD J F. A general method of modelling sound propagation in layered media. *Journal of Sound and Vibration*, **183**(1), 129–142 (1995)

CHANAUD R C. Effects of geometry on the resonance frequency of Helmholtz resonators. *Journal of Sound and Vibration*, **178**(3), 337–348 (1994)

CHANAUD R C. Effects of geometry on the resonance frequency of Helmholtz resonators, part II. *Journal of Sound and Vibration*, **204**(5), 829–834 (1997)

CHU W T. Impulse-response and reverberation-decay measurements made by using a periodic pseudorandom sequence. *Applied Acoustics*, **29**(3), 193–205 (1990)

CHUNG J Y and BLASER D A. Transfer function method of measuring in-duct acoustic properties. I. Theory, II. Experiments. *Journal of the Acoustical Society of America*, **68**(3), 907–921 (1980)

CRAGGS A. A finite element model for rigid porous absorbing materials. *Journal of Sound and Vibration*, **61**(1), 101–11 (1978)

CRAGGS A. A finite element model for acoustically lined small rooms. *Journal of Sound and Vibration*, **108**(2), 327–337 (1986)

CRAGGS A and HILDEBRANDT J G. Effective densities and resistivities for acoustic propagation in narrow tubes. *Journal of Sound and Vibration*, **92**(3), 321–331 (1984)

CRAGGS A and HILDEBRANDT J G. The normal incidence absorption coefficient of a matrix of narrow tubes with constant cross-section. *Journal of Sound and Vibration*, **105**(1), 101–107 (1986)

CRANDALL S H. *Engineering Analysis, a Survey of Numerical Procedures*, chapter 4.6. McGraw-Hill (1956)

CREMER L and MÜLLER H A. *Principles and Applications of Room Acoustics*, volume 2. Applied Science Publishers, London (1978a)

CREMER L and MÜLLER H A. *Principles and Applications of Room Acoustics*, volume 1. Applied Science Publishers, London (1978b)

DICKEY N S and SELAMET A. Helmholtz resonators: One-dimensional limit for small cavity length-to-diameter ratios. *Journal of Sound and Vibration*, **195**(3), 512–517 (1996)

DUNN I P and DAVERN W A. Calculation of acoustic impedance of multi-layer absorbers. *Applied Acoustics*, **19**(5), 321–334 (1986)

FROMMHOLD W, FUCHS H V, and SHENG S. Acoustic performance of membrane absorbers. *Journal of Sound and Vibration*, **170**(5), 621–636 (1994)

FUCHS H V and ZHA X. Einsatz mikro-perforierter Platten als Schallabsorber mit inhärenter Dämpfung. *Acustica*, **81**(2), 107–116 (1995)

FUCHS H V, ZHA X, and NOCKE C. Erprobt und ausgezeichnet: Mikroperforierte Folien-Absorber. *Bauphysik*, **21**(1), 34–38 (1999)

GERHART P M, GROSS R J, and HOCHSTEIN J I. *Fundamentals of Fluid Mechanics*. Addison-Wesley, 2nd edition (1993)

INGARD U. On the theory and design of acoustic resonators. *Journal of the Acoustical Society of America*, **25**(6), 1037–1061 (1953)

INGARD U. Perforated facing and sound absorption. *Journal of the Acoustical Society of America*, **26**(2), 151–154 (1954)

INGARD U and ISING H. Acoustic nonlinearity of an orifice. *Journal of the Acoustical Society of America*, **42**(1), 6–17 (1967)

INGARD U and LYON R H. The impedance of a resistance loaded Helmholtz resonator. *Journal of the Acoustical Society of America*, **25**(5), 854–857 (1953)

ISO 10534-2. *Acoustics - Determination of Sound Absorption Coefficient and Impedance in Impedance Tubes, Part 2: Transfer-function Method* (1996)

ISO 354. *Acoustics - Measurement of Sound Absorption in a Reverberation Room* (1985)

JOHANSEN T F, KRISTIANSEN U R, DHAINAUT M, and BROUARD B. *FEMAK - User's Manual*. NTNU, Dept. of telecommunications, Trondheim (1996). Report no. 429604

JONES M G and STIEDE P E. Comparison of methods for determining specific acoustic impedance. *Journal of the Acoustical Society of America*, **101**(5 I), 2694–2704 (1997)

KANG J, ZHA X, and FUCHS H V. Sound absorbers using microperforated layers. In *Proceedings from the 16th International Congress on Acoustics and the 135th Meeting of the Acoustical Society of America*, pp. 2743–2744. Seattle (1998)

KE L, FENGLEI J, HUI D, and WUZHI Q. Effect of the flat panel resonance on the absorption characteristics of a microperforated-panel absorber. In *Proceedings from the 16th International Congress on Acoustics and the 135th Meeting of the Acoustical Society of America*, pp. 1891–1892. Seattle (1998)

KRISTIANSEN U R and VIGRAN T E. On the design of resonant absorbers using a slotted plate. *Applied Acoustics*, **43**(1), 39–48 (1994)

LANDAU L D and LIFSHITZ E M. *Fluid Mechanics*. Pergamon Press (1959)

LAWRY M H. *I-DEAS Master Series Student Guide*. Structural Dynamics Research Corporation, Milford, Ohio (1998)

LEE J and SWENSON JR G W. Compact sound absorbers for low frequencies. *Noise Control Engineering Journal*, **38**(3), 109–117 (1992)

MAA D Y. Micro-perforated wideband absorbers. *Noise Control Engineering Journal*, **29**(3), 77–84 (1987)

MAA D Y. Potential of microperforated panel absorber. *Journal of the Acoustical Society of America*, **104**(5), 2861–2866 (1998)

MECHEL F P. Helmholtz resonators covered by foils. *Acustica*, **80**(5), 478–489 (1994a)

MECHEL F P. Helmholtz resonators with added porous absorbers. *Acustica*, **80**(3), 268–279 (1994b)

MECHEL F P. Helmholtz resonators with slotted neck plates. *Acustica*, **80**(4), 321–331 (1994c)

MELLING T H. The acoustic impedance of perforates at medium and high sound pressure levels. *Journal of Sound and Vibration*, **29**(1), 1–65 (1973)

MORSE P M and INGARD K U. *Theoretical Acoustics*. Princeton (1968)

MORSET SOUND DEVELOPMENT. WinMLS home page. `http://www.nvo.com/winmls` (1999)

NORDTEST ACOU 095. *Ducted silencers: Transmission loss, Transfer Function Method in Ducts* (1996)

PANTON R L and MILLER J M. Resonant frequencies of cylindrical Helmholtz resonators. *Journal of the Acoustical Society of America*, **57**(6 II), 1533–1535 (1975)

PFRETZSCHNER J, SIMÓN F, RODRIGUEZ R M, and DE LA COLINA C. Simplified calculus to estimate the acoustical absorption of non-planar materials. In *Proceedings from the Joint 137th Meeting of the Acoustical Society of America and the 2nd convention of the European Acoustics Association: Forum Acusticum*. Deutsche Gesellshaft für Akustik, Berlin (1999)

POLYTEC. *Operator's manual, OFV-2200 vibrometer system*. Polytec GmbH (1999)

RANDEBERG R T. A Helmholtz resonator with a lateral elongated orifice. *Acustica*, **86**(1), 77–82 (2000)

RANDEBERG R T, KRISTIANSEN U R, and VIGRAN T E. A Helmholtz resonator with elongated orifice. In *Proceedings from the Joint 137th Meeting of the Acoustical Society of America and the 2nd convention of the European Acoustics Association: Forum Acusticum*. Deutsche Gesellshaft für Akustik, Berlin (1999)

RSCHEVKIN S N. *A Course of Lectures on the Theory of Sound*. Pergamon Press, Oxford (1963)

SAPOVAL B, HAEBERLÉ O, and RUSS S. Acoustical properties of irregular and fractal cavities. *Journal of the Acoustical Society of America*, **102**(4), 2014–2019 (1997)

SDRC SOLUTIONS. SRDC - I-DEAS homepage. `http://www.i-deas.com` (2000)

SELAMET A, DICKEY N S, and NOVAK J M. Theoretical, computational and experimental investigation of Helmholtz resonators with fixed volume: Lumped vs. distributed analysis. *Journal of Sound and Vibration*, **187**(2), 358–367 (1995)

SELAMET A, RADAVICH P M, DICKEY N S, and NOVAK J M. Circular concentric Helmholtz resonators. *Journal of the Acoustical Society of America*, **101**(1), 41–51 (1997)

SMITHS J M A and KOSTEN C W. Sound absorption by slit resonators. *Acustica*, **1**(3), 114–122 (1951)

STINSON M R. The propagation of plane sound waves in narrow and wide circular tubes, and generalization to uniform tubes of arbitrary cross-sectional shape. *Journal of the Acoustical Society of America*, **89**(2), 550–558 (1991)

STINSON M R and SHAW E A G. Acoustic impedance of small, circular orifices in thin plates. *Journal of the Acoustical Society of America*, **77**(6), 2039–2042 (1985)

TANAKA M and TAKAHASHI D. Effect of plate vibration on sound absorption of the microperforated elastic plate. In *Proceedings from the Joint 137th Meeting of the Acoustical Society of America and the 2nd convention of the European Acoustics Association: Forum Acusticum*. Deutsche Gesellshaft für Akustik, Berlin (1999)

VERDEILLE R. *From I-DEAS to FEMAK and From FEMAK to I-DEAS Conditions notebook*. SINTEF, Trondheim (1998a)

VERDEILLE R. *Trans-IDEAS-FEMAK and Trans-FEMAK-IDEAS Handbook*. SINTEF, Trondheim (1998b)

VIGRAN T E. Measuring the acoustic properties of ducts. *Applied Acoustics*, **18**(4), 241–249 (1985)

VIGRAN T E, OLSEN H, and STOREHEIER S . Prediction schemes for acoustical properties of layered media. In *Proceedings from Inter-Noise 91*, volume 2, pp. 1209–1212 (1991)

ZHANG Z M and GU X T. The theoretical and application study on a double layer microperforated sound absorption structure. *Journal of Sound and Vibration*, **215**(3), 399–405 (1998)

ZHOU X, HEINZ R, and FUCHS H. Zur Berechnung geschicteter Platten- und Lochplatten-Resonatoren. *Bauphysik*, **20**(3), 87–95 (1998)

ZIENKIEWICZ O C and MORGAN K. *Finite Elements and Approximation*. Wiley (1983)

ZWIKKER C and KOSTEN C W. *Sound Absorbing Materials*. Elsevier (1949)

Appendix A

Documentation of functions

The headers of all MATLAB-, Perl- and shell functions used in the modelling, measurements and data analysis are presented here.

A.1 General functions

absfakt()

```
function abscoeff = absfakt(Z,rho,c,F)
% abscoeff = absfakt(Z,rho,c,F) calculates the absorption coeffisient of a
% surface from the impedance of the surface.
%
% Parameters:
%
% Z   : impedances of surface
% rho : air density
% c   : velocity of sound in air
% F   : 1 if the impedances are normalized to (rho*c)
%
% If Z is the only parameter, rho = 1.23, c = 340 and F = 0 is assumed
```

lastabs()

```
function [fr,a] = lastabs(filnr);
% [fr,a] = lastabs(filnr) reads frequency and impedance data data from
% za[filnr].dat, and returns the frequencies and absorption coefficients in
% vectors fr and a. The impedance data is assumed to be normalized to (rho*c),
% and each line of the form 'frequency  Re(Z)  Im(Z)'.
%
% Parameters:
%
% filnr : file number. Leading zeros are automatically added (three digits)
%
```

```
% Requires function: absfakt.m
```

lendeh()

```
function z = lendeh(r)
% z = lendeh(r) calculates the mass end correction (acoustic inductance) for a
% circular opening in an infinite baffle. Only one end correction is
% calculated. Air density 1.23 is assumed. From Ingard (JASA 25, p.1037-1061).
%
% Parameters:
%
% r : radius of opening
```

lendehi()

```
function z = lendehi(r,b)
% z = lendehi(r,b) calculates the inner mass end correction (acoustic
% inductance) for a circular opening in an square tube. Only one end
% correction is calculated. Air density 1.23 is assumed. From Ingard (JASA 25,
% p.1037-1061) and Allard (1993, ch. 10)
%
% Parameters:
%
% r : radius of opening
% b : Width of square tube
```

lendes()

```
function z = lendes(w,b)
% z = lendes(w,b) calculates the mass end correction (acoustic inductance) for
% slits in an infinite baffle. Only one end correction is calculated. Air
% density 1.23 is assumed. From Smiths and Kosten (JSV 1, p.114-122)
%
% Parameters:
%
% w : width of slits
% b : center-center distance between slits
```

rendeh()

```
function R = rendeh(R,Omega)
% R = rendeh(R,Omega) returns the viscous acoustic resistance for a
% circular opening (i.e. the resistive end correction). Only one end
% correction is calculated. Air density 1.23 and viscosity 1.79e-5 is
% assumed. From Ingard (JASA 25, p.1037-1061).
%
% Parameters:
%
```

```
% R     : radius of opening
% Omega : angular frequencies
```

rendes()

```
function R = rendes(Omega,w)
% R = rendes(Omega,w) returns the viscous acoustic resistance for a slit
% opening (i.e. the resistive end correction). Only one end correction is
% calculated. Air density 1.23 and viscosity 1.79e-5 is assumed. From
% Kristiansen & Vigran (Applied Acoustics 43, p.39-48).
%
% Parameters:
%
% Omega : angular frequencies
% w     : width of slit
```

tertop()

```
function result = tertop(cond,a,b)
% result = tertop(cond,a,b) returns a if cond == 1, else returns b
```

zhull()

```
function z = zhull(Omega,r,t)
% z = zhull(Omega,r,t) returns the acoustic impedance of a circular tube,
% which is assumed shorter than the wavelength. Air density 1.23 and viscosity
% 1.79e-5 is assumed. From Maa (Noise Control Engineering Journal 29,
% p.77-84). Thermal losses and end corrections are NOT included.
%
% Parameters:
%
% Omega : angular frequencies
% r     : radius of tube
% t     : length of tube
```

zmotvangle()

```
function z = zmotvangle(k,a,Zc,Zwall,theta)
% z = zmotvangle(k,a,Zc,Zwall,theta) returns the (exact) impedance of a layer
% of some media in front of a wall, for oblique sound incidence
%
% Parameters:
%
% k     : wave number in the medium
% a     : the distance to the wall
% Zc    : the characteristic impedance of the medium
% Zwall : impedance of the wall
% theta : angle of sound incidence
```

zmotvapr()

```
function z = zmotvapr(k,a,Zc)
% z = zmotvapr(k,a,Zc) returns the (approximate) impedance of a layer of some
% media in front of a wall.  Assumes cot(k*a) = 1/(k*a).
%
% Parameters:
%
% k     : wave number in the medium
% a     : the distance to the wall
% Zc    : the characteristic impedance of the medium, divided by the
%         cross-section area
```

zmotvegg()

```
function z = zmotvegg(k,a,Zc,Zwall)
% z = zmotvegg(k,a,Zc,Zwall) returns the (exact) impedance of a layer of some
% media in front of a wall.
%
% Parameters:
%
% k     : wave number in the medium
% a     : the distance to the wall
% Zc    : the characteristic impedance of the medium
% Zwall : impedance of the wall
```

zspalte()

```
function z = zspalte(Omega,w,t)
% z = zspalte(Omega,w,t) returns the acoustic impedance of a slit which is
% assumed shorter than the wavelength. Air density 1.23 and viscosity
% 1.79e-5 is assumed. From Maa (NCEJ 29, p.77-84) and Allard (Elsevier 1993).
% Thermal losses and end corrections are NOT included.
%
% Parameters:
%
% Omega : angular frequencies
% w     : width of slit
% t     : depth of slit
```

A.2 Microhorn models

hentdata.sh

```
# The shell script hentdata.sh pipes the FEMAK result files
# <input file name>.$counter through the perl-function
# hentnoder.pl.  The resulting MATLAB .m-files, one
# for each frequency, are numbered as
```

```
# <output file name>_$counter.m
#
# Syntax:
#
# hentdata <input file name> <output file name>
#
# Requires file          : frekdata
# Requires perl function : hentnoder.pl
```

hentnoder.pl

```
# The perl-function hentnoder.pl reads a FEMAK output file, and extracts
# the pressure at the nodes specified in the files utnoderline1 and
# utnoderlinje2.  The pressures and the corresponding positions are written
# to a MATLAB .m-file in the form
#    DATA1=[...];
#    DATA2=[...];
#
# Syntax:
#
# cat <input file name> | hentnoder > <output file name>
#
# Requires files: utnoderlinje1, utnoderlinje2
# These files contain lists of nodes to extract pressures from.
```

ihoved

```
% The script ihoved calculates the absorption coefficient of the microhorn
% geometries defined in one or more defbatch_#.m - files.  The IM method is
% used (in zhornd) to calculate the impedance of the horn.
%
% Requires functions:  zmotvegg.m, lendeh.m, rendeh.m, zhull.m, zhornd.m
```

mhoved

```
% The script mhoved calculates the absorption coefficient of the microhorn
% geometries defined in one or more defbatch_#.m - files.  The FD method is
% used (in zrn_ik) to calculate the impedance of the horn.
%
% Requires functions:  zmotvegg.m, lendeh.m, rendeh.m, zhull.m, zrn_ik.m
```

ONnormal()

```
function angle = ONnormal(Rout,Rin,h,modell,x,z)
% angle = ONnormal(Rout,Rin,h,modell,x,z) returns the angle between the
% z-axis and the vector from point (x,z) perpendicular to the surface of
% the horn, described by the function rhorn.
%
```

```
% Parameters:
%
% Rout   : radius at outer end of horn
% Rin    : radius at inner end of horn
% h      : length of horn
% modell : modell number in rhorn.m
% x, z   : start point of vector
%
% Requires functions: rhorn.m, ONvektor.m
```

ONvektor()

```
function length2 = ONvektor(Z,Rout,Rin,h,modell,x,z)
% length2 = ONvektor(Z,Rout,Rin,h,modell,x,z) returns the square of the
% length of the vector between points (radius(Z),Z) and (x,z).
%
% Parameters:
%
% Z      : z-distance of first point
% Rout   : radius at outer opening of horn
% Rin    : radius at inner opening of horn
% h      : length of horn
% modell : modell number in rhorn.m
% x, z   : position of second point
%
% Requires functions: rhorn.m
```

regnalt.sh

```
# The shell script regnalt.sh calls the program FEMAK to calculate the
# pressure at the nodes defined in FEMIN.DAT.  For each frequency defined
# in the file frekdata, the frequency and the corresponding flow resistance
# and back cavity impedance is read from frekdata and substituted in
# FEMIN.DAT, and the FEMAK program is run.  The output files, one for each
# frequency, are numbered as FEMOUT.DAT.counter
#
# Requires files         : FEMIN.DAT, frekdata
# Requires perl function : settinndata.pl
```

rhorn()

```
function result = rhorn(Rout,Rin,z,h,model)
% result = rhorn(Rout,Rin,z,h,model) returns the radius of a 'horn' as
% function of distance from the outer opening.
%
% Parameters:
%
% Rout, Rin : outer and inner radius of the horn
```

```
% z         : distance from outer opening
% h         : length of horn
% model     : specify the shape of the horn. Can be any of these:
%
%             0 = constant,      Rin
%             1 = linear,        Rin + (Rout-Rin)*(1-z/h)
%             2 = quadratic,     Rin + (Rout-Rin)*(1-z/h)^2
%             3 = elliptic,      Rin + (Rout-Rin)*sqrt(1-z^2/h^2)
%             4 = exponential,   Rin + (Rout-Rin)*(exp((h-z)/h)-1)/(exp(1)-1)
%             5 = polynomial, based on measurements on an actual horn,
%                 Rin = 2.75e-4, Rout = 1.95e-3, h = 2.3e-3.
%                 For z > 2.3e-3, result = 2.75e-4.
%                 Input parameters Rin, Rout and h are ignored
%             6 = logarithmic, Rin - 1/k*log(1-(h-z)/h*(1-exp(-k*(Rout-Rin))))
%                 Parameter k is set to 1795 to give the same general
%                 shape as the horn in model 5
%
% Requires file: horn.mat which contains the polynomial coefficients used
%                 in model 5.
```

rhorninv()

```
function result = rhorninv(X,Rout,Rin,h,model,Radius)
% result = rhorninv(X,Rout,Rin,h,model,Radius) returns the difference
% between radius in a horn at a distance X from the outer opening, and the
% given Radius.
%
% Parameters:
%
% X         : distance from outer opening
% Rout, Rin : outer and inner radius of the horn
% h         : length of horn
% model     : see rhorn.m
% Radius    : radius to be compared with radius at X
%
% Requires file: horn.mat which contains the polynomial coefficients used
%                 in model 5.
```

settinndata.pl

```
# The perl-function settinndata.pl reads the datafile frekdata, and
# substitutes the frequency and the corresponding flow resistance and back
# cavity impedance into the FEMAK input file FEMIN.DAT.
#
# Syntax:
#
# settinndata.pl <frequency number> > <output filel>
#
```

```
# Requires files: FEMIN.DAT, frekdata
# The data file frekdata must contain lines of the form
#   frequency, flow resistance, Re(Za), Im(Za)
# where Za is the impedance of the back cavity.
```

zhornd()

```
function z = zhornd(R0,Rh,h,N,Omega,modell)
% z = zhornd(R0,Rh,h,N,Omega,modell) returns the acoustic impedance of a
% microhorn. The impedance is calculated by numerical integration of the
% impedance of a number of segments with constant cross-section. Air density
% 1.23 and viscosity 1.79e-5 is assumed. Thermal losses are
% neglected. From Maa (NCEJ 29, p.77-84).
%
% Parameters:
%
% R0,Rh  : Outer and inner radius of horn
% h      : length of tube
% N      : number of segments
% Omega  : angular frequencies to calculate
% modell : model number in rhorn.m
%
% Requires function: rhorn.m
```

zrn_ik()

```
function ZRes = zrn_ik(ZEnde,w,r0,rh,h,modell,Lmin,M,plotting,plotting2,...
                       matrise,informasjon)
% ZRes = zrn_ik(...) calculates the specific impedance by the outer opening
% of a microhorn.  The linear Navier-Stokes eq., with non-compressible flow,
% is used.
%
% Parameters:
%
% ZEnde       : impedances at inner end of horn, corresponding to w
% w           : angular frequencies
% r0          : radius of outer end of horn
% rh          : radius of inner end of horn
% h           : length of horn
% modell      : modell number in rhorn.m
% Lmin        : Number of x-steps in inner end of horn
% M           : Number of z-steps in horn
% plotting    : =1 to print the velocity field
% plotting2   : =1 to also print 3D plots of velocities and pressure
% matrise     : =1 to print the coefficient matrix
% informasjon : =1 to print misc. information
%
% Requires functions: rhorn.m, rhorninv.m, ONnormal.m
```

A.3 Perforated panel models

avis

```
% The script avis.m calculates the absorption coefficient for two closely
% separated, perforated plates placed in front of a hard wall. Based on
% expressions mainly from Ingard & Morse (1968).
%
% Requires functions: zmotvegg.m, zmotvapr.m, lendeh.m, lendehi.m,
%                     rendeh.m, zhull.m, rvl.m
```

mhoved

```
% The script mhoved.m calculates the absorption coefficient for two closely
% separated, slitted plates placed in front of a hard wall. The main
% procudere (the FDM calculation) is in the function zrn_sik_ny.m.  The
% input geometries are defined in the files mbatch_#.m
%
% Requires functions: zmotvegg.m, lendes.m, rendes.m,
%                     zspalte.m, zrn_sik_ny.m
```

rvl()

```
function [Rvis,L] = rvl(rad1,rad2,b,a,antx,omega,Z,dv)
% [Rvis,L] = RvL(rad1,rad2,b,a,antx,Omega,Z,dv) returns the viscous, acoustic
% resistance and acoustic inductance of the air gap between two closely
% separated plates. The velocity field is calculated by a superposition of the
% cylindrical flow from each hole (source in front plate, sink in rear plate).
% Air density 1.23 and velocity of sound in air 340 is assumed. Rvis is
% calculated with eq. 6.4.39 in Morse & Ingard (1968), L is calculated with
% eq. 9.1.10 in M&I.
%
% Parameters:
%
% rad1, rad2 : radius of holes in front and rear plate
% b          : distance between holes
% a          : distance between plates
% antx       : numeber of points in x- and y-direction to calculate
% Omega      : angular frequencies
% Z          : specific impedance in gap between plates
% dv         : viscous boundary layer thickness
%
% Requires function: upv.m
```

upv()

```
function [ux,uy] = upv(antx,Fluks,rad,a,x0,y0,x,y);
% [ux,uy] = upv(antx,Fluks,rad,a,X0,Y0,x,y) returns the velocity in the x-
```

```
% and y-direction from a cylindrically radiating source.
%
% Parameters:
%
% antx       : number of points in x- and y-direction to calculate
% Fluks      : fluid flux
% rad        : radius of source
% a          : height of source
% x0, y0     : positions of source center(s)
% x, y       : positions where velocity are calculated
```

zrn_sik_ny()

```
function ZRes = zrn_sik_ny(ZEnde,w,b1,b2,o2,cca,a,Lmin1,LminS,M,S1,S2,...
                           plotting,jaja,matrise,informasjon)
% ZRes = zrn_sik_ny(...) simulates the non-compressible, linear Navier-Stokes
% eq. and the mass conservation eq. with the finite difference method between
% two closely separated, slitted plates, and returns the specific impedance a
% little distance into the front slits. The relative distance between front
% and rear slits can be specificed.
%
% Parameters:
%
% ZEnde         : impedance a distance S2*dz into rear slit
% w             : angular frequencies to calculate
% b1, b2        : widths of front and rear slits
% o2            : horizontal distance between center of front and rear slit
% cca           : center-center distance between slits
% a             : distance between plates
% Lmin1, LminS  : minimum number of x-steps pr. cca and min(b1,b2)
% M             : number of z-steps in the gap between plates
% S1, S2        : number of z-steps into front and rear slit
% plotting      : =1 to show velocity distributions
% jaja          : =1 to show more velocity and pressure distributions
% matrise       : =1 to show the coefficiont matrix filling
% informasjon   : =1 to show some informative information
```

A.4 Measurements

loadimp()

```
function [imp_res, Fs, Format, Comment] = loadimp(filename)
% LOADIMP  Load WinMLS 1.1 impulse response files.
%
% Copyright Morset Sound Development 2/1-98
```

Qintv

```
% The program Qintv.m is a menu-driven program where the user can set
% parameters, calibrate, measure & calculate the intensity in front of a panel
% absorber, and the vibration velocity of the panel, using a three channel
% measurement.
%
% Requires functions: Qcintv.m, Qmintv.m, Qkintv.m, Qpintv.m
%
% Extended from a original program by T.E.Vigran
```

Qcintv()

```
function CalOK = Qcintv(fpath,filn,extt,seqord,fs,navg,setupfile);
% CalOK = Qcintv(...) does a two-microphone calibration, and returs CalOK == 1
% if all is OK. The calibration data is saved in a file with name
% (fpath + filn + '.mat').
%
% Parameters:
%
% fpath     : path to files to be written
% filn      : filename basename for the calibration files
% extt      : filename extension
% seqord    : MLS sequence order
% fs        : sampling frequency
% navg      : number of averages
% setupfile : WinMLS setup file name
%
% Requires file: winmls.m, loadimp.m
%
% Extended from original function by T.E. Vigran
```

Qkintv()

```
function []=Qkintv(fpath,filekname,filername,filecname,mikdsep,miklsep,...
%                  temp,fstart,fend,sstart,send);
% function Qkintv(...) reads the measured transfer functions and impulse
% responses from (fpath + filekname + '.mat'), plots them for visualisation,
% together with the absorption coefficient, reflection coefficient and
% normalized vibration, and (optionally) saves the result to
% (fpath + filername + '.mat').
%
% Parameters:
%
% fpath     : path to files to be read/written
% filekname : measurement file to read
% filername : results file to write
% filecname : calibration filename
% mikdsep   : distance between microphones
```

```
% miklsep   : distance between mic. 1 and sample
% temp      : temparature during measurements
% fstart    : First frequency to be included in plots
% fend      : Last frequency to be included in plots
% sstart    : First frequency to be included in plots
% send      : Last frequency to be included in plots
```

Qmintv()

```
function MeaOK = Qmintv(fpath,filemname,filecname,extx,seqord,...
                        fs,nav,setupfile);
% MeaOK = Qmintv(...) does the MLS measurement of two microphones and one
% vibrometer (three channels) and saves the resulting impulse responses and
% transfer functions to (fpath + filemname + '.mat'). MeaOK == 1 if all is
% well.
%
% Parameters:
%
% fpath     : path to file to be read/written
% filemname : measurement filename
% filecname : calibration filename
% extx      : measurement filename extension
% seqord    : sequence order
% fs        : sampling frequency
% nav       : number of averages
% setupfile : WinMLS setup file name
%
% Requires files: winmls.m, loadimp.m
%
% Extended from original function by T.E.Vigran
```

Qpintv()

```
function []=Qpintv(fpath,filebase,filetypec,filetypem,filetyper,mikdsep,...
                   miklsep,temp,fstart,fend);
% function Qpintv(...) reads the measured transfer functions and impulse
% responses from (fpath + filebase + 'm*.mat'), and writes the calculated
% reflection coefficient, normalized vibration, and impedance to
% (fpath + filebase + 'r*.mat').
%
% Parameters:
%
% fpath     : path to files to be read/written
% filebase  : Base file name
% filetypec : Char. for calibration
% filetypem : Char. for measurements
% filetyper : Char. for results
% mikdsep   : distance between microphones
```

```
% miklsep   : distance between mic. 1 and sample
% temp      : temparature during measurements
% fstart    : First frequency to be included in files
% fend      : Last frequency to be included in files
```

WinMLS()

```
function [] = WinMLS(SF, FN1, FN2, CO, SO, NA, Fs, ST, FSD)
% WINMLS  Perform MLS measurement using WinMLS 2.0.
%
% Copyright Morset Sound Development 2/9-98
```